UNIVERSITÀ
DEGLI STUDI
DI PADOVA

Sede Amministrativa: Università degli Studi di Padova

Dipartimento di Ingegneria Idraulica, Marittima, Ambientale e Geotecnica

SCUOLA DI DOTTORATO DI RICERCA IN Scienze dell'Ingegneria Civile ed Ambientale

CICLO XXIII

EVALUATION OF SEDIMENT PROPERTIES USING WIND AND TURBIDITY OBSERVATIONS AND EXPERIMENTAL INVESTIGATION OF THE IMPACT OF MACROALGAL MATS ON SEDIMENT STABILITY AND FLOW DYNAMICS IN SHALLOW TIDAL AREAS.

Direttore della Scuola : Ch.mo Prof. Stefano Lanzoni
Supervisori : Ch.mo Prof. Marco Marani
Ch.mo Prof. Stefano Lanzoni

Dottoranda : Chiara Venier

Ai miei genitori e a Guido

Contents

List of Figures

List of Tables

Abstract

Sediment resuspension and deposition are key processes governing intertidal morphodynamics and are crucially influenced both by physical and biological factors. The present thesis addresses two important aspects of sediment transport processes in intertidal areas. The first topic concerns the quantitative analysis of suspended sediment concentration and wind forcing to provide estimates of sediment properties, such as settling velocity and the critical shear stress for erosion, valid at a spatial scale which is relevant for the overall morphodynamics of the system. The first part of the thesis thus develops and describes a method to evaluate sediment properties based on the solution of a sediment mass conservation equation in the water column accounting for the effects of wind-induced and current-induced bottom shear stress. The method is applied by using data from a network of *in situ* sensors in the Venice lagoon and provides estimates which compare favorably with observations in the same shallow tidal areas, and are in line with what is expected for sandy-silt sediments. The proposed estimation method is direct and quantitative, it does not interfere with the local system physical and biological status, and lends itself to the monitoring of sediment parameters on a seasonal basis and for long periods of time with limited operational effort. The second, related, topic treated here concerns the laboratory study of the impact of mats of *Ulva intestinalis* on sediment stability and flow dynamic in shallow tidal areas. Macroalgae are a controlling factor of flow and sediment stability, as they act to inhibit sediment erosion due to waves or currents and promote sedimentation. Algal mats are increasingly more frequent

and extended in many coastal and estuarine intertidal habitats and it is thus important to quantitatively characterize their impact on the flow field and on sediment stability, in order to better understand ongoing degradation of coastal lagoons and to develop suitable mitigation and restoration measures. The second part of the thesis thus describes and analyzes a series of experiments performed in a large open-channel flume (the Total Environment Simulator - TES- facility at University of Hull, UK), set up with a bed of fine sand, partially covered by strands of *U. intestinalis*. The experiments allowed the accurate measurement, both in space and time, of flow velocity distributions, water levels, bed levels, and suspended sediment concentration. The presence of macroalgae was found to influence both the velocity distribution near the sediment bed, and the Reynolds shear stress acting on it. Direct inspection during the experiments and data analysis suggest that macroalgae exert a significant bio-stabilizing effect.

Sommario

La risospensione e la deposizione dei sedimenti sono processi chiave nel governo della morfodinamica a marea e sono influenzate in modo cruciale sia da fattori fisici che biologici. La presente tesi affronta due importanti aspetti dei processi di trasporto dei sedimenti negli ambienti a marea.

Il primo argomento riguarda l'analisi quantitativa della concentrazione del sedimento in sospensione e della forzante vento per produrre delle stime delle proprietà del sedimento, quali la velocità di sedimentazione e lo sforzo tangenziale critico per l'erosione, a scale spaziali rilevanti per la generale dinamica morfologica del sistema. La prima parte della tesi pertanto sviluppa e descrive un metodo per valutare le proprietà del sedimento sulla base della soluzione di una equazione di conservazione del sedimento nella colonna d'acqua che tiene conto degli effetti dello sforzo tangenziale al fondo dovuto al vento e alle correnti di marea. Il metodo è applicato utilizzando osservazioni da una rete di sensori nella laguna di Venezia e produce stime in buon accordo con osservazioni puntuali negli stessi siti e allineate con i valori attesi per sedimenti sabbiosi-limosi. L'analisi è stata effettuata attraverso serie temporali relative a intensità del vento, fornite da stazioni anemometriche, a misure di torbidità, fornite da sensori torbidimetrici ed a serie temporali relative a livelli di marea acquisite dalla rete telemareografica; tutte le stazioni operano simultaneamente, sono disposte in prossimità l'un l'altra e ricoprono grossomodo l'intera area lagunare. Per calcolare gli sforzi dovuti all'azione del moto ondoso è stato implementato

un modello puntuale forzato dal vento sotto l'ipotesi di fetch illimitato, in cui gli sforzi sono stati calcolati in funzione del coefficiente di attrito, della densità dell'acqua e della velocità orbitale massima al fondo. La velocità orbitale massima al fondo è stata espressa in funzione dell'altezza d'onda ed il periodo d'onda che è stato calcolato in funzione di parametri adimensionalizzati e seguendo la legge di potenza i cui parametri di fitting sono stati adattati alle osservazioni in laguna. L'altezza d'onda è stata calcolata secondo un bilancio energetico in cui si è trascurata la componente advettiva dell'energia dell'onda. Con il modello forzato dalla marea si sono calcolati gli sforzi in funzione del coefficiente di attrito, della densità dell'acqua e della velocità della corrente di marea. Una volta calcolati gli sforzi tangenziali al fondo è stata implementata l'equazione di conservazione della massa di sedimenti assumendo concentrazione dei sedimenti spazialmente uniforme (divergenza del flusso nulla e continuità della massa d'acqua), in cui la variazione nel tempo del prodotto tra il tirante e la concentrazione (la concentrazione viene espressa come differenza tra la concentrazione effettivamente acquisita dai torbidimetri ed una concentrazione residua che rimane sempre in sospensione in laguna) è data dalla somma tra il flusso di erosione ed il flusso di sedimentazione. Nel caso di processo di sedimentazione, il flusso erosivo è stato trascurato, ed i parametri ws (velocità di settling) e Co (concentrazione residua) sono stati calcolati risolvendo un fitting lineare. Una volta calcolati i valori di velocità di deposizione compresi tra $2.7 \cdot 10^{-4}$ e $6.3 \cdot 10^{-4}$ m/s e la concentrazione residua compresa tra 6.7 e 16.2 mg/l, si sono successivamente calcolati la velocità di erosione, sulla base della quale si è risolto l'algoritmo del simplesso per ottenere la curva di regressione dei valori medi di velocità di erosione. Dalla regressione si sono ottenuti i valori dello sforzo critico di erosione compresi tra 0.1 e 0.5 Pa e del parametro di erosione compresi tra $2 \cdot 10^{-6}$ e $3 \cdot 10^{-4} kg/sm^2$. E' stata compiuta inoltre un'analisi stagionale dopo aver suddiviso le serie temporale in stagioni secondo la suddivisione astronomica. I risultati si sono dimostrati in generale in soddisfacente accordo con i valori misurati in situ attraverso le tradizionali strumentazioni, Sea Carousel e Mini

Flume. La metodologia implementata ha il vantaggio di stimare i parametri dei sedimenti senza interferire con gli effetti di bio-stabilizzazione operati dai microrganismi e di fornire una stima parzialmente integrata delle soglie di erosione e della velocità di sedimentazione. Si può in definitiva concludere che il metodo di stima proposto è diretto e quantitativo, non interferisce con lo stato fisico e biologico locale del sistema e si presta ad attività di monitoraggio delle proprietà dei sedimenti su base stagionale e per lunghi periodi, con limitato sforzo operativo.

Il secondo, correlato, argomento riguarda lo studio di laboratorio dell'impatto della macroalga *Ulva intestinalis*, sulla stabilità del sedimento e sul campo di velocità in aree a marea. Le macroalghe, infatti, esercitano un controllo importante sulla distribuzione della velocità e sul trasporto di sedimenti, poiché inibiscono l'erosione del sedimento dovuta a onde o correnti e promuovono la sedimentazione. Larghe estensioni di macroalghe sono sempre più frequenti in molti habitat intertidali estuarini e costieri ed è dunque importante caratterizzare quantitativamente il loro impatto sul campo di moto e la stabilità del sedimento, per una migliore comprensione dell'attuale degrado di lagune costiere e per sviluppare adatte misure di mitigazione e ricostruzione ambientale. La seconda parte della tesi, dunque, descrive e analizza una serie di esperimenti condotti in una canaletta di grandi dimensioni (il Total Environment Simulator - TES- presso l'Università di Hull, UK), con sedimento costituito da sabbia fine, parzialmente coperto da individui di *U. intestinalis*. L'attività sperimentale è stata indirizzata a quantificare l'effetto delle macroalghe sulla dinamica della struttura del campo di moto indotto da correnti e moto ondoso. L'apparato strumentale utilizzato è costituito da una canaletta di 11 metri di lunghezza e 2 di larghezza, su cui è disposto uno strato di sedimenti artificiali non coesivi (sabbia fine: $135\mu m$ di diametro). L'apparato è fornito di generatore di flusso ed onde. Attraverso una completa strumentazione costituita da ADV (Acoustic Doppler Profiler), PIV (Particle Image Velocimetry), ABS (Acoustic BackScatter) si sono fornite informazioni su: andamento temporale del vettore velocità,

evoluzione temporale della superficie del fondo, andamento temporale della concentrazione dei sedimenti sospesi. Si sono infine utilizzate trappole di sedimento posizionate all'uscita del flusso di corrente dalla canaletta per fornire l'integrale della massa solida trasportata. Sono stati compiuti 12 test simulando diverse condizioni idrodinamiche: corrente ed onde per diversi livelli di tirante (0.21 m; 0.31 m; 0.25 m) dapprima in presenza di macroalghe e successivamente su fondo nudo. Le alghe dopo essere state prelevate presso la Riserva Naturale Nazionale di Budle Bay, sulla costa nord-orientale dell'Inghilterra, sono state ripiantate nello strato di sedimenti della canaletta in modo da seguire una disposizione su linee trasversali sfalsate ricoprendo tutta la superficie della canaletta con una densità di circa 12 unità $/m^2$. Con l'obiettivo di quantificare le osservazioni raccolte durante ciascun test ed in particolare al fine di determinare l'intervallo di tempo entro cui calcolare il valor medio delle velocità turbolente, si è inizialmente calcolata la funzione di autocorrelazione della componente longitudinale della velocità di fluttuazione. Dalla funzione di autocorrelazione si sono calcolate la microscala e la macroscala temporale per i diversi esperimenti. Al fine di calcolare la velocità di attrito ed il parametro di scabrezza di Nikuradse, si è implementata la legge universale logaritmica delle velocità media per paretri scabre. Per ottenere questi parametri, si è realizzato il fitting lineare dei dati sperimentali: dalla stima della pendenza ed intercetta si sono ottenuti la velocità di attrito ed il parametro di scabrezza. Al fine di determinare l'esistenza di una relazione statisticamente significativa tra le rette di regressione (fitting lineare per i quattro ADV nelle 4 posizioni in cui sono stati disposti gli strumenti), si è calcolato l'errore standard per la pendenza e l'intercetta da cui si sono determinati i relativi intervalli di confidenza al 95 %. Sia la velocità di attrito sia il parametro di scabrezza sono risultati maggiori nei test con macroalghe piuttosto che nei test senza macroalghe, confermando quanto riscontrato in letteratura sul ruolo bio-stabilizzatore delle macroalghe. Sulla base degli sforzi di Reynolds e del gradiente di velocità media si è poi calcolato il profilo verticale degli sforzi tangenziali, i quali hanno dimostrato comportamenti differenti tra

i test con e senza macroalghe. Nel primo caso gli sforzi aumentano dal fondo fino ai primi centimetri per poi diminuire quasi linearmente fino alla superficie, mentre nel secondo caso diminuiscono linearmente dal fondo alla superficie. Infine con l'obiettivo di studiare la struttura della turbolenza, si è calcolato lo spettro monodimensionale dell'energia nel tempo, caratterizzato principalmente dalla presenza di vortici di piccole dimensioni corrispondenti alle alte frequenze. Per visualizzare il trend decrescente della densità di energia è stato calcolato il valor medio dell'energia (binning) nell'intervallo inerziale. Si è calcolato il fitting lineare da cui si è ottenuto il valore la pendenza. Dal confronto delle pendenze per i diversi test, si sono ottenuti valori minori per i test con macroalghe che per i test senza macroalghe, poichè si ritiene che queste ultime agiscano interferendo sulla struttura della turbolenza del campo di energia. Attraverso l'ipotesi di Taylor si è calcolata la macroscala spaziale sulla base delle fluttuazioni temporali precedentemente calcolate, in modo da produrre lo spetto monodimensionale dell'energia nello spazio. Anche in questo caso la pendenza nel test con macroalghe è risultata minore rispetto alla pendenza nei test senza macroalghe. Dall'osservazione diretta compiuta durante gli esperimenti e dai risultati ottenuti dall'elaborazione dei dati di velocità acquisiti dagli ADV, si conferma quanto riscontrato in letteratura riguardo al ruolo bio-stabilizzatore delle macroalghe, a cui si associa riduzione del campo di moto in prossimità del fondo, forme di fondo di dimensioni inferiori, minor quantità di materiale solido trasportato sia di fondo sia in sospensione.

Chapter 1

Introduction

Shallow tidal areas, such as tidal flats, salt marshes, sub-tidal areas, submerged aquatic vegetation, characterize the coastal and estuarine regions worldwide. Tidal flats are intertidal, non-vegetated, soft sediment habitats, found between mean high-water and mean low-water spring tide datums (Dyer *et al.*, 2000) and are generally located in estuaries and other low energy marine environments. Salt marshes are accessible coastal habitats, relatively elevated areas colonized by halophytic vegetation. Sub-tidal flats are unvegetated areas characterized by lower elevation (e.g. muddy platforms that do not emerge during ordinary low tide) (Allen, 2000), (Marani *et al.*, 2006).

Shallow tidal areas represent relevant areas of global interest, as more than 40% of the world's population resides on the world's coast (UNEP, 2006). They host high biodiversity and primary productivity, supporting a high biomass of micro and infaunal organisms, and play an important role in the tidal nutrient chemistry. Collectively these habitats are of great importance to large numbers of invertebrates and fish, supporting complex estuarine food webs and provide resting and feeding areas to large numbers indigenous and migratory birds. They have an important role in preventing erosion caused by wind and current action. Tidal flats often form the buffer zone between deeper reaches of the lagoon

thereby protecting intertidal habitats by dissipating wave energy, thus reducing erosion of salt marshes.

Shallow tidal areas are very fragile bio-geomorphological systems, vulnerable to irreversible changes partially due to anthropogenic impact (e.g. alteration of coastal hydrology, metal and nutrient pollution, introduction of non-native species etc.), thus affecting the ecology, and the socio-economy of coastal and estuarine regions worldwide.

The global distribution of salt marshes subjected to erosion and continuous changes is represented in Fig. 1.1 (Gedan *et al.*, 2009).

Studying sediment erosion, deposition and re-suspension processes in shallow tidal areas is thus important in order to achieve a better understanding of the bio-geomorphologic evolution of these ecosystems.

The first part of this study is concerned with erosion and deposition processes in the Venice lagoon (Italy) (see Chapter 2), which are analyzed using wind and turbidity observations. The Venice Lagoon, located in North-east Italy, is the largest lagoon in Italy, with an area of about 550 km^2, an average depth of about 1 m, and a semidiurnal tidal forcing with a mean tidal range from 50cm during neap tide to 100cm during spring tide.

The Venice Lagoon is a clear example of how the erosion processes are prevailing over sedimentation processes, mainly due to the increasing wave action (including all factors causing erosion, such as ship and boat wakes which, in the last few decades, have had as much impact as wind waves on the lagoon deterioration process (CVN, 2004)). As a consequence of the increasing erosive effects, salt marshes reduce and tidal flats elevation decreases. An example of salt marshes subjected to massive erosion and margin retreat in the Venice Lagoon, is shown in Figure 1.1 (l).

Defina *et al.* (2007) in particular describe the long-term evolution the Venice lagoon suffered during the last century, suggesting the existence of three different phases: firstly salt marshes deteriorate and progressively shrink supplying sediments to the near tidal flats, which can maintain their morphology; sec-

Figure 1.1: The global distribution of salt marshes (Chapman, 1977). (a) Tantramar Marshes in the Bay of Fundy.(b) Marshes in San Francisco Bay.(c) Graphic map of Terrebone Bay, Louisiana shows in red the trend of marsh loss from 1990 to 2000. (d) Marsh die-offs in Cape Cod. (e) As sea level rises, mangroves are overtaking salt marsh in Australia.(f) Invasive Spartina in China overtakes mudflat habitat and native plant zones.(g) Storm surge barriers in the Netherlands keep floodwaters out of reclaimed marshland that has subsided below sea level. (h) The port of Rotterdam, the Netherlands was built primarily on reclaimed salt marsh and has more than doubled in size in the past 50 years. (i) Salt marsh hay harvested in New England. (l) Venice lagoon. Eroded saltmarshes are pointed out in red, while the still present saltmarshes are pointed out in yellow. Elaboration based on data provided by the Ministero delle Infrastrutture e dei Trasporti- Magistrato alle Acque di Venezia.

ondly salt marshes lose too much sediment and are unable to provide it to the near tidal flats. Finally as a consequence, tidal flat elevation decreases with a deepening and homogenization of the whole bathymetry (Carniello *et al.*, 2009). This trend is shown in Fig. 1.2 by Carniello *et al.* (2009), where four different sceneries (from 1901 to 2003) illustrating salt marshes deterioration and tidal flat deepening in the Venice Lagoon are shown.

The second part of this study concerns mats of green macroalgae (*Ulva intestinalis*), which strongly interact with hydrodynamics and sediment dynamics of shallow tidal areas. Macroalgae are common in many coastal areas, especially those enriched in nutrients, due to the increasing of eutrophization. When forming dense mats, they cause the sediment to be enriched in organic matter, thus strongly impacting the benthic communities. In exposed ecosystems, such as coastal or estuaries waters, macroalgae grow attached to pebbles or shells, in order to prevent them from drifting. In such cases the interaction with flow may result in a stabilizing effect of the sediment with the generation of several small scale bedforms (small ripples). The quantification of the impact of macroalgae on sediment and flow dynamic is thus important in order to study the evolution of shallow tidal ecosystems.

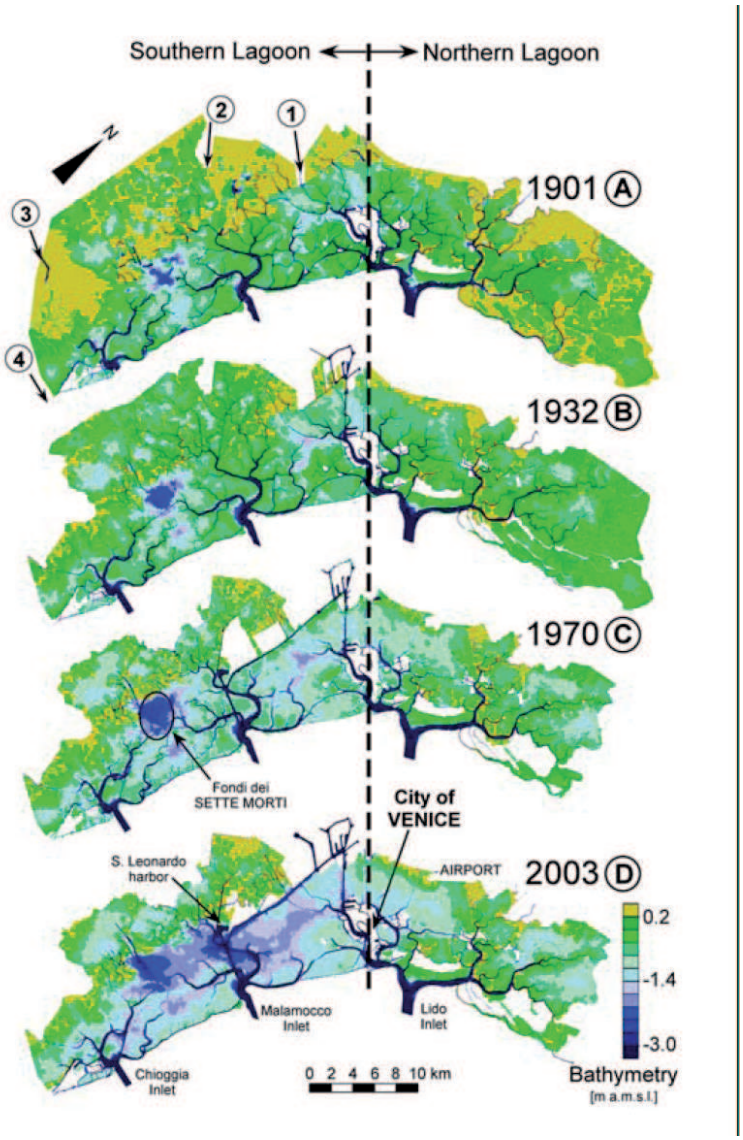

Figure 1.2: Bathymetry of the Venice lagoon, Italy, in (a) 1901, (b) 1932, (c) 1970, and (d) 2003. Elevations are in meters above mean sea level (m amsl) and they have been referred to the mean Adriatic Sea level recorded when each survey was performed.(Carniello *et al.*, 2009)

Chapter 2

Evaluation of sediment properties

2.1 Introduction

Tidal geomorphologies host high biodiversity and primary productivity, and are the site of important cultural and economic centers worldwide. In a time of anthropogenic and natural climate change, tidal bio-geomorphic systems are most exposed to changing rates of sea-level rise (SLR), which can produce dramatic structural changes in the system equilibrium states (Morris *et al.*, 2002),(Kirwan and Murray, 2007), (Marani *et al.*, 2007). In order to quantify sediment transport, deposition, and erosion processes at the system scale, observational methods of sediment properties must be aimed at spatial scales comparable to those of the system (as opposed to local, point measurement methods) and must not interfere with the biological state of the bottom sediment (e.g. superficial biofilms), which so importantly affects its mechanical properties (Paterson, 1964). In particular, observations of sediment properties, such as the settling velocity, the residual concentration which is supposed to never settle

within the lagoonal ecosystem, the erosion parameter, and the critical shear stress for erosion, are required for a better understanding of the underlying biophysical processes and to apply appropriate sediment transport models (Mehta, 1984). *In situ* measurement techniques are available, such as the Sea Carousel and the Cohesive Strength Meter (Paterson, 1964), (Amos *et al.*, 2004), allowing useful characterizations of the local sediment properties. However, some of the available methods refer to properties (e.g. the pressure of the jet used to induce erosion) only indirectly related to the mechanical characteristics of the sediment. Furthermore, while sediment resuspension by waves and tidal currents is controlled by sediment properties on a relatively large scale, existing methods can only provide very local estimates of sediment properties on areas of the order of a few to tens of square centimeters. Finally, it may be argued that the inappropriate application of field apparatuses may produce perturbations of the local physical and biological sediment status, thereby affecting the observed characteristics. The idea of estimating sediment properties from turbidity, wave and currents acquisitions has been already treated by several authors. (Traykovsky *et al.*, 2007) computes settling velocity from concentration observations, using a hindered settling velocity formulation to account for the high concentrations present in the wave boundary layer. (Kineke and Sternberg, 1989) compute suspended sediment concentrations from settling velocity measures directly acquired by in situ instrumentation, thus implementing a relation, which links the two variables. On the basis of this idea, the settling velocity, the residual concentration, critical shear stress for erosion as well as the erosion parameter are here evaluated through of a sediment balance equation in the water column. The sediment balance equation is solved by considering measured turbidity values and water levels, in which the erosion term depends on the wind-induced and tide current-induced Bottom Shear Stress (BSS), computed by using a point wave model forced by measured wind velocities, tidal levels and tidal velocity. The method provides estimates at a scale comparable to the wave size without interference with the local physical and biological sediment conditions.

2.2 Materials

In order to characterize the erosion and sediment processes in the lagoonal ecosystem through wind velocity and turbidity records, we estimate the parameters of incipient motion, entrainment and sedimentation, such as the settling velocity, the residual concentration, the critical shear stress for erosion, the erosion parameters. For this purpose we use anemometric, turbidimetric and mareographic data time series acquired in the study area, the Venice Lagoon, by the Venice Water Authority within a monitoring network, in the period 2004-2006, as well as two temporary stations, which were operated by the Venice Water Authority - Consorzio Venezia Nuova in the period 2002-2003 and acquired simultaneous turbidity, pressure, and anemometric data. The study sites are shown in Figure 2.1: each station corresponds to a sensor (turbidimetric sensors in red, anemometric sensors in blue, and hydrometric sensors in green), while the 1BF e 2BF sites, in violet, include turbidimetric, anemometric, and hydrometric sensors.

Wind velocity and direction observations from the monitoring network in the period 2004-2006 were recorded by MET-ONE anemometers at Coscritti, Valle Liona, Tessera, S.Andrea, S. Leonardo, Molo Ceppe, and Allacciante stations (see Figure 2.1 for station locations) every 15 minutes at a height of 5 m above mean sea level (MSL). The anemometers are equipped with both a wind speed sensor (Met One - model 014A, 1.5 % accuracy relative to the detection range) and a wind direction sensor (Met One - model 020C). The former consists of three paddles joined together to a body, which rotates according to the wind intensity. By means of a sealed magnetic read switch, an electrical signal at a rate proportional to wind speed is produced. The latter consists of a lightweight airfoil vane directly coupled to a single precision potentiometer, which produces a signal of 0 - 5 V corresponding to angle interval 0 to 360º.

Semi-hourly turbidity records are acquired by Seapoint turbidimeters, which are embedded in the Idronaut OS316 multiparametric sensors of the monitoring network of the Venice Water Authority (SAMANET monitoring program

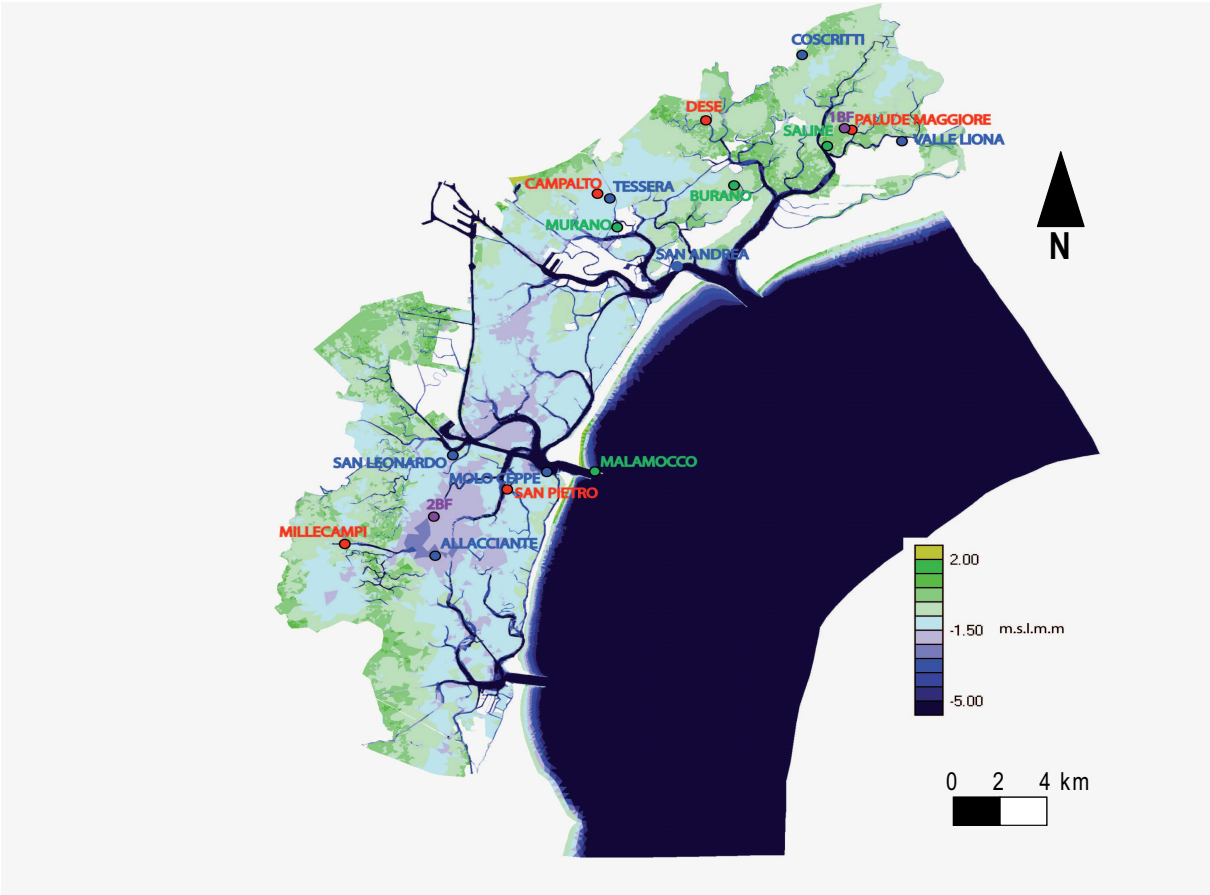

Figure 2.1: Bathymetry of the Venice Lagoon with anemometric (Coscritti, Valle Liona, Tessera, S.Andrea, S. Leonardo, Molo Ceppe, and Allacciante), turbidimetric (Palude Maggiore, Dese, Campalto, S. Pietro, and Millecampi), and mareographic stations (Saline, Burano, Murano, and Malamocco). 1BF (*S.Felice* area) and 2BF (*Fondo dei Sette Morti* area) acquire simultaneously turbidity, pressure, and anemometric data.

http://www.magisacque.it/sama.htm). Turbidimeters are located in sub-tidal areas at Palude Maggiore, Dese, Campalto, S. Pietro, and Millecampi stations (see Figure 2.1 for station locations). Turbidimeters are active optical sensors, which emit a light beam (at the 880 nm wavelength in the present case) and are equipped with a photodiode, which detect the light backscattered by particles suspended in water and generate an output voltage proportional to turbidity (FTU, Formazine Turbidity Units), which is a function of the amount of inorganic matter suspended in the water column. The resulting turbidity measurement is expressed in Formazine Turbidity Units (FTU). Turbidity and suspended sediment concentration are two parameters which can not be correlated, as are function of different variables. Suspended sediment concentration depends on the total weight of particles in suspension with a diameter bigger than 0.4 μm and thus is a direct function of the number, dimension and specific weight of particles. Instead turbidity is a direct function of the number, surface and index of refraction of the suspended particles and at the same time is an inverse function of the size of suspended particles. Water samples at the depth level and the time instant correspondent to turbidity records for 2BF station (see afterwards), are collected in order to calibrate the turbidimeters and to study a relation between turbidity and suspended particles. Water samples are filtered *in situ* to avoid sensitive variations in the chemical and granulometric composition, due to absorption, release or mineralization, thus the suspended sediment concentration is estimated by difference in weight between a polycarbonate membrane and the water volume filtered.

We also use hourly tidal levels measured at four tide gauges (Saline, Burano, Murano, and Malamocco (see Figure 2.1 for station locations), from the tidal level monitoring network of the Venice Municipality. Water level acquisitions are referred to the hydrometric level of Punta della Salute, that is correlated to the reference point of IGMI (Istituto Geografico Militare Italiano). The water level sensors are supplied with a 200 mm-diameter float, which converts its position to a digital record, with a 1 cm resolution and a $\pm$ 1 cm accuracy.

Raw data are processed in order to obtain a homogeneous data set of simultaneous semi-hourly observations. In particular, wind data are averaged at the 0.5 hour resolution, while hourly tidal levels are linearly interpolated to obtain half-hourly estimates. This latter operation, with a maximum tidal excursion during spring tides of 140 *cm* in 12 hours, is not deemed to produce significant inaccuracies.

In addition to the data systematically acquired by the observation network described, as mentioned above, we use observations from a temporary station, coded 1BF (*S.Felice* area, in the northern part of the Venice lagoon (see Fig. 2.1) and 2BF (*Fondo dei Sette Morti* area, in the southern part of the Venice lagoon (see Fig. 2.1), which were operated by the Venice Water Authority - Consorzio Venezia Nuova in the period 2002-2003 and acquired simultaneous turbidity, pressure, and anemometric data.

Turbidity was recorded by an optical backscatter sensor (OBS-3+ sensor), which works on the same physical principle as the Seapoint turbidimeter described above (operating at the 850 *nm* wavelength). The turbidity records from the 1BF and 2BF station were calibrated by the Venice Water Authority by collecting water samples for which the SSC was determined by filtering and accurate weighing. A linear relation between the SSC (mg/l) and the turbidity measurements was respectively deduced: SSC= 0.92 Turbidity ($R^2 = 0.07$) for 1BF site and SSC= 1.5 Turbidity ($R^2 = 0.99$) for 2BF site.

The water level is acquired by a Microcat sensor, which works at 0.002 % of full scale range of resolution and 0.1 % of full scale range of accuracy. Wind velocity and direction at 1BF and 2BF are measured by MET-ONE anemometers (see above), located at a height of 4 m above mean sea level (MSL).

Wave data were also acquired: the significant wave height is computed as the arithmetic mean of the wave heights observed in a fifteen period of time. Wind, wave, and turbidity data are acquired every fifteen minutes: the value recorded is the average among the values of the first height minutes of acquisition.

The stations considered are located in areas which are different both in terms

of abiotic (mean water levels, temperature, salinity, etc.) and biotic conditions. For example, algae (genus *Gracilaria* and *Ulva*) are found at Campalto and Palude Maggiore, while phanerogam meadows are found in proximity of S. Pietro and 2BF sites. For the 2004-2006 period the mean turbidity values are about 42 FTU for the Campalto site, 23 FTU for S. Pietro and 21 FTU Palude Maggiore and 11 FTU for 2BF; the mean temperature value is about 16 ^oC at Campalto and S. Pietro, and 11 ^oC for Palude Maggiore. The mean salinity is about 28 *psu* for Campalto, 34 *psu* for S. Pietro, and 32 *psu* for Palude Maggiore. The mean chlorophyll concentration is about 3.8 $\mu g/l$ for Campalto, 1.3 $\mu g/l$ for S. Pietro, and 0.2 $\mu g/l$ for Palude Maggiore.

The local median bottom sediment diameter is assumed to be in the range 17-47.5 μm on the basis of measurements by the Venice Water Authority (CVN, 2004) and inferred from nearby measurement by Amos *et al.* (2004).

A summary of all the above described site characteristics is reported in table 2.1.

Table 2.1: Measurement sites. Latitude and Longitude are in Gauss-Boaga coordinates. $< depth >$ is the average instantaneous water depth; distance sensor-bed is the distance of the turbidity sensor from the bed; d_{50}, the median sediment diameter, at 2BF was measured by the Venice Water Authority and was inferred from nearby measurement by Amos *et al.* (2004) for the remaining turbidimeters.; $< U >$ is the average wind velocity measured for the period of analysis and $< C >$ is the average turbidity measured for the period of analysis.

SITE	LAT	LON	¡depth¿	distance sensor-bed	d_{50}	$< U >$	$< C >$
	(m)	(m)	$(ma.m.s.l.)$	(m)	(m)	(m/s)	(FTU)
Allacciante	5019648	2299527	-	-	2.1		-
Campalto	5038699	2311679	-1.05	0.4	25.7	-	31
Coscritti	5046369	2321344	-	-	-	2.8	-
Dese	5042633	2316699	-2.5	0.4	27	-	58
Millecampi	5022722	2307295	-0.9	0.4	34	-	40
Molo Ceppe	5023688	2309187	-	-	-	3	-
Palude Maggiore	5042185	2323744	-1.9	0.4	19	-	22
S.Andrea	5034680	2315376	-	-	-	3.3	-
S.Leonardo	5024635	2304735	-	-	-	4	-
S.Pietro	5022722	2307295	-1.3	0.4	47.5	-	21
Tessera	5038570	2312059	-	-	-	3	-
Valle Liona	5041681	2326045	-	-	-	2.5	-
1BF	5042228	2323720	-1.10	0.4	19	4.6	16
2BF	5021189	2303812	-2.1	0.4	38	5	15

2.3 Methods

2.3.1 Wind wave and Tidal Current Model

In order to estimate sediment bed properties, we firstly compute the total bottom shear stresses, τ, on the basis of a point model (zero-dimensional), where both the wind wave and the tidal current contributions account (Soulsby, 1997):

$$\tau = \tau_{wind} + \tau_{curr} \left[1 + 1.2 \left(\frac{\tau_{wind}}{\tau_{wind} + \tau_{curr}} \right)^{3.2} \right] \tag{2.1}$$

where τ_{wind} is the wind-induced bottom shear stress, τ_{curr} is current-induced bottom shear stress.

The basic hypothesis for the implementation of the model are: 1) point model (0-dimensional), i.e. no spatial variation in the forcing or the bathymetry;
2) depth-limited conditions: in shallow waters wave height is in equilibrium with local water depth;
3) fetch-unlimited conditions (fetch is assumed to be large enough for waves to be fully developed. This assumption is justified at sites, like those where the turbidimeters are deployed, which are far from obstacles inducing wind sheltering effects, see Fig. 2.1.)

Wind wave model

The wind-wave model estimates the wave height, H_w, by writing an energy conservation equation (Hasselmann, 1974). Wind waves are generated by the transfer of wind energy to the free surface. Considering an undisturbed free surface waves grow until their height is stabilized due to energy dissipation by bottom friction, wave-breaking because of interactions with the bottom, and attainment of the steepness limit (*white capping*). Equilibrium is thus reached

when the rate of energy transfer from the wind field equals the rate of energy dissipation.

One may thus start by writing the following energy conservation equation, based on a linear theory for monochromatic waves (Hasselmann, 1974), (Gelci *et al.*, 1957):

$$\frac{\partial E}{\partial t} + \vec{\nabla} \cdot (\vec{c}_g E) = S = S_w - S_{bf} - S_{wc} - S_b \tag{2.2}$$

where E is the wave energy, $\vec{c}_g$ is the group celerity, S is a source term including: S_w is wave growth by wind action, S_{bf} is the energy dissipation due to bottom friction, S_{wc} is the energy dissipation due to whitecapping, S_b is the energy dissipation due to depth-induced breaking (Carniello *et al.*, 2005) and (Fagherazzi *et al.*, 2006).

For the model assumptions mentioned above, the spatial and temporal scales required to reach equilibrium are very small in shallow tidal areas (Fagherazzi *et al.*, 2006), thus the local rate of change of wave energy and its advection flux (second term on the left hand side of equation 2.2) may be neglected. Thus S=0 and a balance exists between all the source terms:

$$S_w = S_{bf} + S_{wc} + S_b \tag{2.3}$$

In eq.2.3, the energy growth of waves, S_w is expressed through the parameters α and β, (Cavaleri and Malanotte-Rizzoli, 1981):

$$S_w = \alpha + \beta E \tag{2.4}$$

where α (equation 2.5) and β (equation 2.6) are functions of frequency and wind characteristics (Phillips, 1957), (Barnett, 1968).

$$\alpha = \frac{80 \rho_s^2 \Omega}{g k^2} c_d^2 U_{wind}^2 \tag{2.5}$$

where ρ_s is the dimensionless ratio between ρ_a, air-density (1.25 kg/m^3) and ρ_w, water-density (1027 kg/m^3), Ω is $\frac{2\pi}{T_w}$, where T_w is the wave period as

expressed later in the text (see 2.15-2.16), k is the wave number as expressed later in the text (see 2.14), c_d is the drag coefficient equal to 0.0012, according to Smith and Banke (1975) for wind velocity between 5 and 15 m/s, and U_{wind} is wind intensity.

$$\beta = 5\frac{\rho_s U_{wind} k}{T_w \Omega} - 0.9 \tag{2.6}$$

In eq.2.3 S_{bf}, S_{wc}, and S_b are the factors contributing to wave decay.
S_{bf}, the energy dissipation due to bottom friction, is expressed as (Carniello *et al.*, 2005) (Fagherazzi *et al.*, 2006):

$$S_{bf} = -4\frac{c_{bf}\pi H_w k}{T_w sinh(kD) sinh(2kD)} \tag{2.7}$$

where c_{bf} is the coefficient of bottom friction set equal to 0.015 (Collins, 1972), and D is the instantaneous water depth.

S_{wc}, the energy dissipation due to whitecapping, is expressed as (Hasselmann, 1974):

$$S_{wc} = -0.0000333\Omega\frac{\gamma_{ws}}{\gamma_{pm}^2}, \quad \gamma_{ws} = \frac{1}{8}\frac{H_w^2\Omega^4}{g^2} \tag{2.8}$$

where γ_{ws} is the integral wave-steepness parameter, γ_{pm} =0.00457 is the theoretical value of wave-steepness for a Pierson-Moskovitz spectrum, which is the spectrum of a fully developed sea (Pierson and Moskowitz, 1989).

S_b, the energy dissipation due to depth-induced breaking, is expressed according to a probabilistic approach for the breaking criterion (Battjes and Janssen, 1978):

$$S_b = -2\frac{Q_{br}}{T_w \frac{H_w}{H_{max}^2}} \tag{2.9}$$

where Q_{br}, the probability that waves with height H_w will break, is expressed as:

$$Q_{br} = 1.8(\frac{H_w}{H_{max} - 0.4})^3 + 1.7(\frac{H_w}{H_{max} - 0.4})^2 \tag{2.10}$$

where H_{max} is the maximum wave height.

Finally the significant wave height, H_w, is expressed as (Longuet-Higgins and Stewart, 1962):

$$H_w = \sqrt{\frac{8S_w\Omega}{\rho_w g}} \tag{2.11}$$

H_w is iteratively computed by means of equations 2.4- 2.11. The convergence is reached whenever the energy growth of waves, S_w equals the sum of the dissipative terms (bottom friction (S_{bf}), whitecapping (S_{wc}), and depth-induced breaking (S_b)).

Once H_w has been determined, the wind-induced bottom shear stress, τ_{wind} can be computed by the quadratic form:

$$\tau_{wind} = \frac{1}{2}\rho_w \ f_w \ u_m^2 \tag{2.12}$$

where f_w is a wave friction coefficient, and u_m is the maximum horizontal orbital velocity at the bottom. Orbital velocity express in equation 2.13 represents the speed at which the water moves in wave orbits and is calculated from the length of time it takes a water particle to complete an orbit. For waves in shallow water depths, the maximum horizontal velocity near the bed is related to wave height, H_w, water depth, D, wave number, k and wave period, T_w.

f_w and u_m may be evaluated on the basis of the empirical relationship proposed by Soulsby (1997) and of wave linear theory:

$$f_w = 1.39\left[\frac{u_m T_w}{2\pi d_{50}/12}\right]^{-0.52}, \quad u_m = \frac{\pi H_w}{T_w \sinh(kD)} \tag{2.13}$$

where d_{50} is the local median bottom sediment diameter (see Table 2.1), according to available information, and k is the wave number determined through the classical dispersion relationship, upon the assumption of a monochromatic wave.

$$\sigma^2 = gk \tanh(k\mathcal{D}) \tag{2.14}$$

In our analysis we improve the wind-wave point-model (Fagherazzi *et al.*, 2006) by considering time-dependant water surface elevations, water depths, and wind velocities. We also relax the assumption of constant wave period, T_w (Carniello *et al.*, 2005),(Fagherazzi *et al.*, 2006), by computing the time dependant wave period on the basis of the relationship proposed by Young and Verhagen (1996a), Young and Verhagen (1996b) and recently reconsidered by Breugem and Holthuijsen (2007)

$$\hat{T}_w = \alpha \hat{D}^{\beta} \tag{2.15}$$

where $\hat{T}_w$ and $\hat{D}$ are the dimensionless wave period and water depth, respectively, computed as follows (Young and Verhagen, 1996a),(Young and Verhagen, 1996b), (Breugem and Holthuijsen, 2007)

$$\hat{T}_w = \frac{g\,T_w}{U_w}; \quad \hat{D} = \frac{DU_w}{g^2} \tag{2.16}$$

where g is gravity and U_w is the wind velocity.

The parameters (β=scaling exponent= 0.35 and α=intercept = 3.5) in eq. 2.15 are determined on the basis of 2BF data by Carniello *et al.* (2009). The assumptions for the validity of eq. 2.15 are depth-limited conditions, which is justified in the present case of shallow waters, and fetch unlimited conditions.

Tidal current model

The current-induced bottom shear stress, τ_{curr}, is computed as a function of the tidal velocity, u_{curr} (Fagherazzi *et al.*, 2003):

$$\tau_{curr} = \rho_w \; f_w \; u_{curr}^2 \tag{2.17}$$

where the velocity of the tidal current is computed as:

$$u_{curr} = u_{curr(0)} \left(\frac{1}{3} + \frac{2}{3} \frac{h}{h_{ref}} \right) \tag{2.18}$$

In eq.2.18 h is the tidal level and h_{ref} is a reference depth (assumed equal to 2.5 m). $u_{curr(0)}$ represents the velocity of the tidal current for the reference depth and is computed as a function of a maximum velocity, u_{max} (assumed 0.25 m/s for d_{50}= 22 μm and 0.30 m/s for d_{50}= 74 μm, see Fagherazzi *et al.* (2003)). We assumed u_{max} equal to 0.25 m/s for the 2BF site, and u_{max} equal to 0.30 m/s for the other stations.

$$u_{curr(0)} = u_{max}\left(\frac{\frac{dh}{dt}}{\frac{dh}{dt}_{max}}\right) \tag{2.19}$$

2.3.2 Suspended Sediment Concentration Model

We estimate bed sediment properties by means of the conservation of sediment mass in the water column:

$$\frac{dC'D}{dt} = -\vec{\nabla}\cdot(C'D\cdot\vec{u}) + \mu_e\left(\frac{\tau-\tau_c}{\tau_c}\right) - w_sC' \tag{2.20}$$

where $C' = C - C_0$ is the exceedance of the instantaneous Suspended Sediment Concentration (SSC), with C assumed to be homogeneous in the water column, with respect to a base SSC value and C_0 is introduced because observed time series indeed exhibit a background SSC value related to non-precipitable suspended matter. D is the instantaneous water depth; $\vec{u}$ is the velocity of the current; μ_e is the erosion parameter; τ is the total bottom shear stress (BSS); τ_c is the critical shear stress for erosion (Parchure and Mehta, 1985), H is the Heaviside step function (equal to zero for $\tau - \tau_c < 0$ and equal to one for $\tau - \tau_c > 0$); and w_s is the settling velocity.

Eq.2.20 recognizes that the time variation of the suspended sediment mass in the water column, CD, is determined by incoming and outgoing advective, erosion, and settling fluxes.

We next assume the SSC to be uniform over a local area surrounding the measurement station, such that the term $\vec{\nabla}\cdot(C'D\cdot\vec{u})$, the first term in the right-hand side of eq. 2.20, is equal to zero.

The continuity of water mass $\frac{\partial D}{\partial t} + \nabla\cdot(D\ \vec{u}) = 0$ can then be used to elimi-

nate what remains of the advection term, thus transforming eq. 2.20 into the following:

$$D\frac{\partial C}{\partial t} = \mu_e H\left(\frac{\tau - \tau_c}{\tau_c}\right) - w_s C' \tag{2.21}$$

Eq. 2.21 can be used to retrieve μ_e, τ_c, and w_s from observations once the bottom shear stress can be evaluated at each time. This is done here by computing the contributions to the total shear stress τ due to wind waves and tidal currents.

2.3.3 Estimation of sediment bed properties

In order to determine the settling velocity, w_s, and the residual concentration, C_0, eq. 2.21 we first analyze the sub-intervals of the observational time series in which the BSS is small, i.e. in which erosion is negligible. To ensure that only settling events are considered, we select only the time intervals in which: i) $\tau < 0.1Pa$, where τ is computed by eq.2.1 (experiments with thresholds between 0.1 and 0.3 Pa, low values ensuring that no erosion occurs, yield almost overlapping results); ii) $\frac{\partial C}{\partial t} < 0$, to ensure that only periods of undisturbed sediment settling after a resuspension event are considered.

Within the time intervals selected according to the above criteria, it is safe to assume that the erosion flux may be neglected, such that we can write:

$$D\frac{\partial C}{\partial t} = -w_s C + w_s C_0 \tag{2.22}$$

Observational SSC values allow the evaluation of $D\frac{\partial C}{\partial t}|_i \approx D_i\frac{C_{i+1}-C_i}{\Delta t}$, through forward finite differences, where D_i and C_i are quantities observed at time t_i, and Δt is the time step (fifteen minutes for the 1BF and 2BF site and half an hour for the remaining stations). We now study $D\frac{\partial C}{\partial t}|_i$ as a function of C_i, which, according to 2.22, must be a linear function with slope equal to $-w_s$ and intercept $w_s C_0$.

In order to obtain a more statistically robust estimation of w_s and C_0 we also carry out a binned averaging procedure, which consists in determining sub-

intervals of SSC values containing a constant number of experimental values (50 here, but tests with different numbers of experimental point lead to very similar results) and by representing the individual experimental values in each sub-intervals by the average values of $D\frac{\partial C}{\partial t}|_i$ and C_i.

Linear regression of the binned values now allows the estimation of C_0 and w_s. The latter takes the meaning of an average settling velocity, representative of a whole settling velocities distribution, in turn corresponding to a distribution of suspended sediment grain sizes. The distribution of settling velocities can also be evaluated by applying eq. 2.22 at each time interval:

$$w_{si} = -\frac{D_i}{C_i - C_0}\frac{C_{i+1} - C_i}{\Delta t} \tag{2.23}$$

where C_0 is now known.

The sediment diameter distribution can in turn be estimated by means of Stoke's Law:

$$D_{si} = \sqrt{\frac{18\nu w_{si}}{(\frac{\rho_s}{\rho_w} - 1)g}} \tag{2.24}$$

where $\nu = 1.112 \cdot 10^{-6} m^2/s$ is the kinematic viscosity, ρ_s is the density of the sediment (on the basis of in situ measurements by Amos *et al.* (2004) we assume $\rho_s = 1352 kg/m^3$ for the 2BF site, $\rho_s = 1783 kg/m^3$ at Tessera-Campalto, $\rho_s = 1795 kg/m^3$ at S.Leonardo-S.Pietro, $\rho_s = 1691 kg/m^3$ at Valle Liona-Palude Maggiore).

On the basis of the w_s and C_0 values determined above we can now compute the erosion rate, ϵ, for all observational intervals in which $\tau > \tau_c$. From 2.21:

$$\epsilon = \mu_e\left(\frac{\tau - \tau_c}{\tau_c}\right) = D\frac{\partial C}{\partial t} + w_s(C - C_0) \tag{2.25}$$

A binning of the BSS values into 0.05 Pa intervals has then been performed, subsequently inferring the critical shear stress for erosion, τ_c, and the erosion parameter, μ_e, by non-linear regression of observational ϵ vs BSS values using the Nelder-Mead simplex algorithm (Lagarias *et al.*, 1998).

2.4 Results

2.4.1 Wind wave model

Before describing in details the estimates of the sediment bed properties obtained from the above-mentioned methodology, we want to show how our computations of the wave height (see eq. 2.4- 2.11) are in good correlation with the measurements of the significant wave height measured at the 2BF site. Figures 2.2-2.5 shows this validation for three events characterized by Bora, Scirocco or Levante winds.

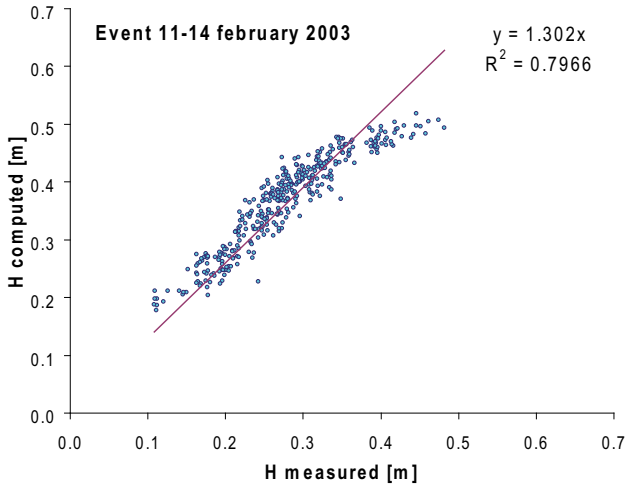

Figure 2.2: Correlation between the wave height simulated and the wave height measured at 2BF site for a Bora event during days 11-14 February 2003.

Our point model is also in good agreement with the 2-dimensional model, from which it has been derived and which assumes fetch limited conditions and no constraints for the complete development of the wave motion (H_w gradually reaches the equilibrium state) (Carniello *et al.*, 2005). Our model result solid and consistent with these simulations (see Fig. 2.6-2.9) in particularly for the Bora and Levante events.

We processed the available wind, water-level, and turbidity data to obtain a homogeneous set of simultaneous semi-hourly observations. Wind data were

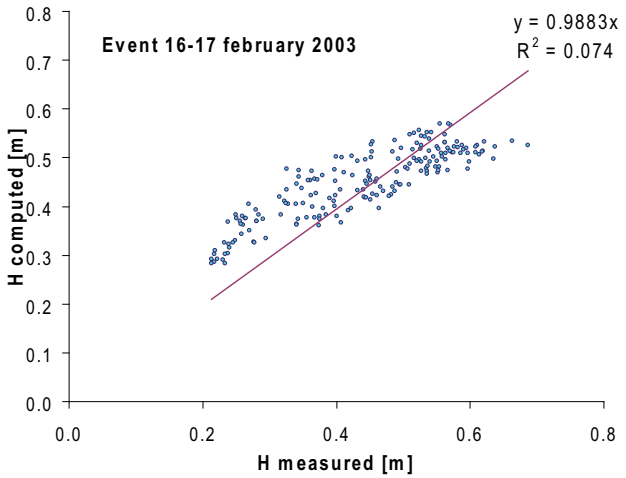

Figure 2.3: Correlation between the wave height simulated and the wave height measured at 2BF site for a Levante event during days 16-17 February 2003.

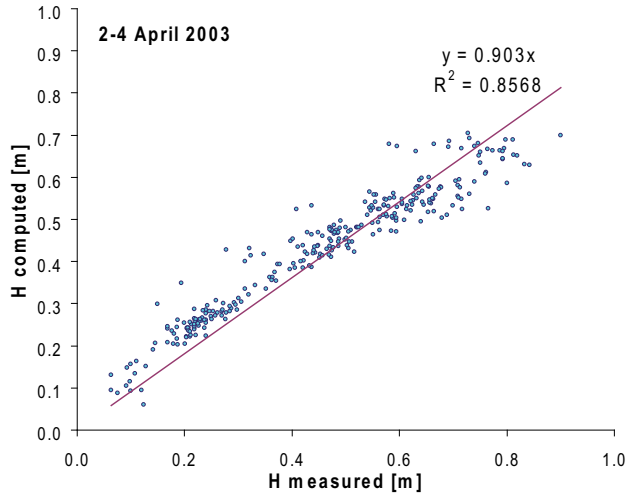

Figure 2.4: Correlation between the wave height simulated and the wave height measured at 2BF site for a Bora event during days 2-4 April.

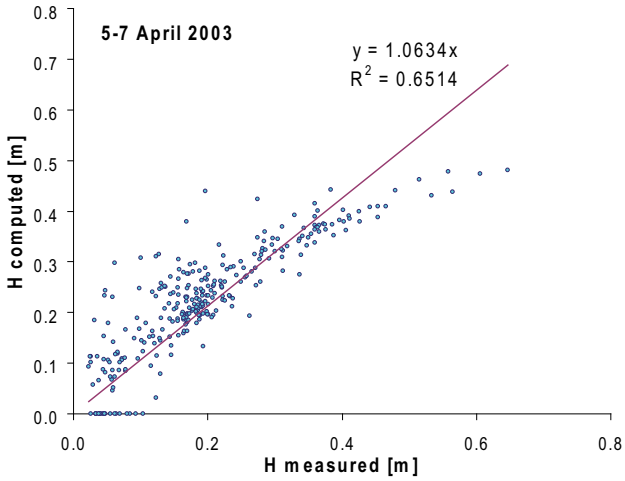

Figure 2.5: Correlation between the wave height simulated and the wave height measured at 2BF site for a Scirocco event during days 5-7 April.

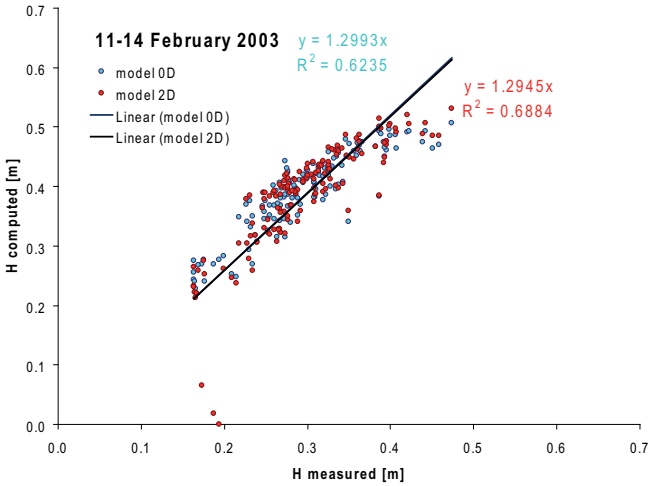

Figure 2.6: Comparison between the wave height simulated by the 0D model and the wave height simulated by the 2D model which accounts for depth and assumes no constraints for the complete development of the wave motion. Bora event (11-14 February 2003).

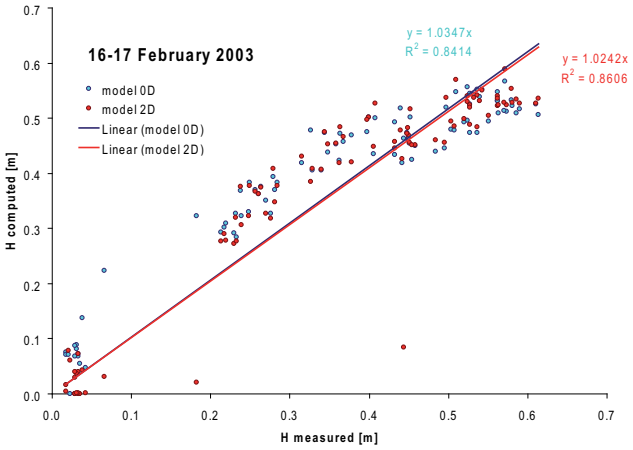

Figure 2.7: Comparison of the wave height simulated by the 0D model and the wave height simulated by a 2D model which accounts for depth and assumes no constraints for the complete development of the wave motion. Levante event (16-17 February 2003).

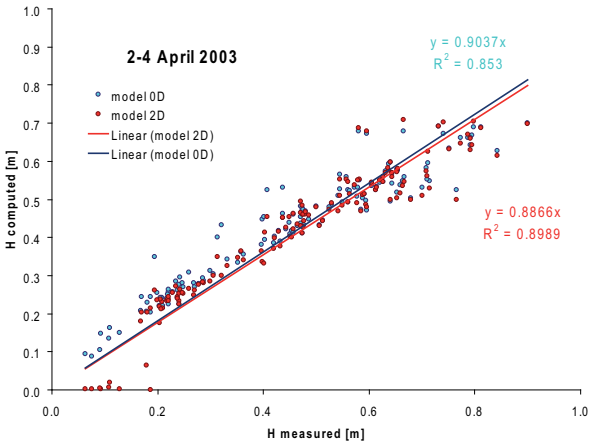

Figure 2.8: Comparison of the wave height simulated by the 0D model and the wave height simulated by a 2D model which accounts for depth and assumes no constraints for the complete development of the wave motion. Bora event (2-4 April).

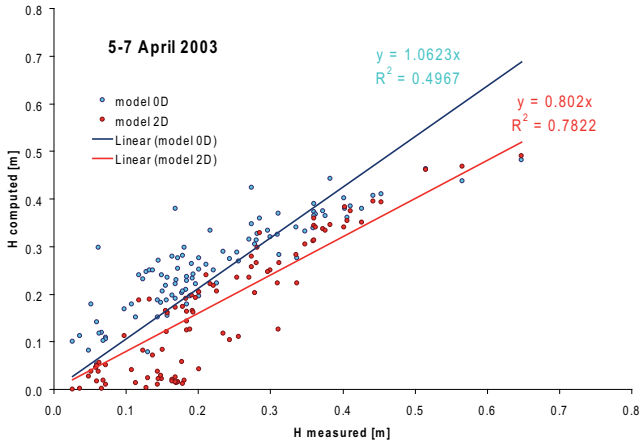

Figure 2.9: Comparison of the wave height simulated by the 0D model and the wave height simulated by a 2D model which accounts for depth and assumes no constraints for the complete development of the wave motion. Scirocco event (5-7 April).

averaged at the 0.5 hour resolution, while hourly tidal levels were linearly interpolated to obtain half-hourly estimates. Each turbidimeter was then associated with the closest anemometer and tide gauge, such that wave estimates obtained on the basis of the wind-wave model may be considered as representative of the wave action causing observed turbidity values. On the basis of this criterion and considering the quantity and the good quality of data recorded, we select the Campalto turbidimeter and associate with the Tessera anemometer, and the Murano tide gauge, the Palude Maggiore turnidimeter with the Valle Liona anemometer, and the Saline tide gauge. Finally, we select the S. Pietro turbidimeter and associate with the S. Leonardo anemometer wind observations, and the Malamocco tide gauge etc.

A seasonal analysis was also performed by subdividing the whole time series in winter-period, spring-period, summer-period and fall-period according to the astronomic subdivision.

In order to estimate the sediment bed properties we firstly compute the total bottom shear stresses by means of eq. 2.1. From a previous analysis of data time series, we observe that a signal between the turbidity and the

wind velocity, thus the bottom shear stresses, occurs. Figures 2.10 a,b,c clearly show this signal. The observations of tidal levels, wind intensities, and turbidity observations, respectively, for the semi-hourly 2004-2006 data at three-associated stations within the Venice Lagoon clearly display periods in which turbidity rapidly increases due to high-wind events, followed by periods of weaker wind, in which turbidity decays as a result of reduced turbulence. The bottom shear stresses computed by implementing eq. 2.1 for the semi-hourly 2004-2006 data at the Tessera-Campalto stations is shown in Fig. 2.10d. A correlation between the estimated bottom shear stresses and turbidity may be inferred, with turbidity increases lagging bottom shear stresses positive fluctuations.

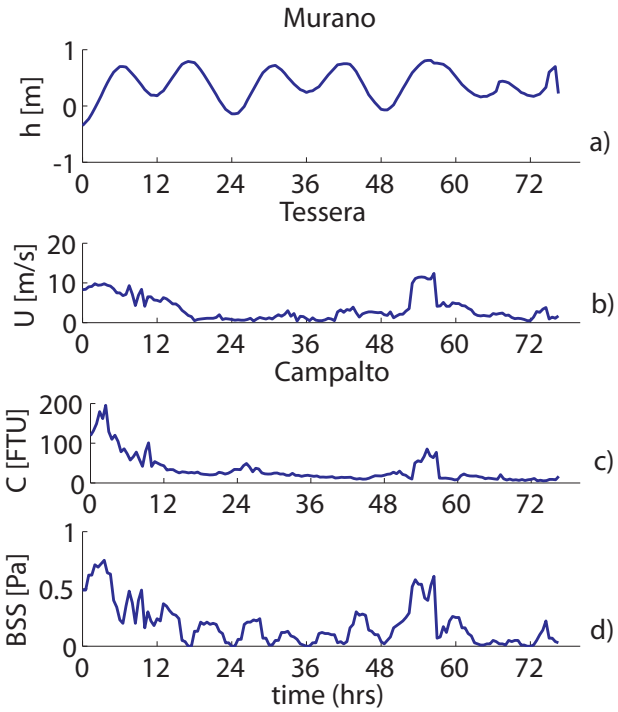

Figure 2.10: Time series of measured a) tidal level at Murano; b) wind velocity at Tessera; c) turbidity at Campalto; and d) computed BSS.

As mentioned in section Bottom Shear Stress, the total bottom shear stresses are due to both contribution of wind-induced shear stresses, τ_{wind}, and current-induced shear stresses, τ_{curr}. The frequency distribution (number of element

which falls within the interval obtained by subdividing the x-axis vector in 50 classes) for four main stations that we choose as the best representative for northern and southern lagoon, are reported in the following figures 2.11-2.14. Except Tessera-Campalto site, where the mean τ_{curr}=0.07 Pa is slightly higher than the mean τ_{wind}=0.05 Pa, in the other sites here analyzed the mean value of τ_{curr} is lower than τ_{wind}, such that for S.Leonardo-S.Pietro mean τ_{curr}=0.04 Pa and mean τ_{wind}=0.06 Pa; for Valle Liona-Palude Maggiore mean τ_{curr}=0.02 Pa and mean τ_{wind}=0.03 Pa; and for 2BF mean τ_{curr}=0.001 Pa and mean τ_{wind}=0.1 Pa. In the latter the current-induced shear stresses can be negligible compare to wind-induced shear stresses, as shown in Fig. 2.11.

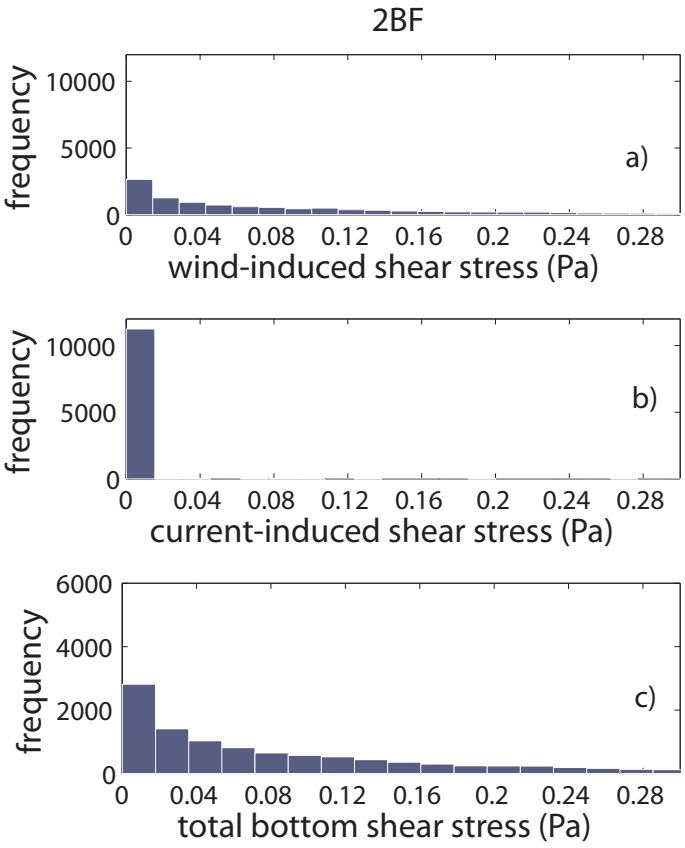

Figure 2.11: Frequency Distribution of bottom shear stresses for 2BF site. a) wind-induced bottom shear stress distribution. b) current-induced bottom shear stresses. c) total shear stress distribution.

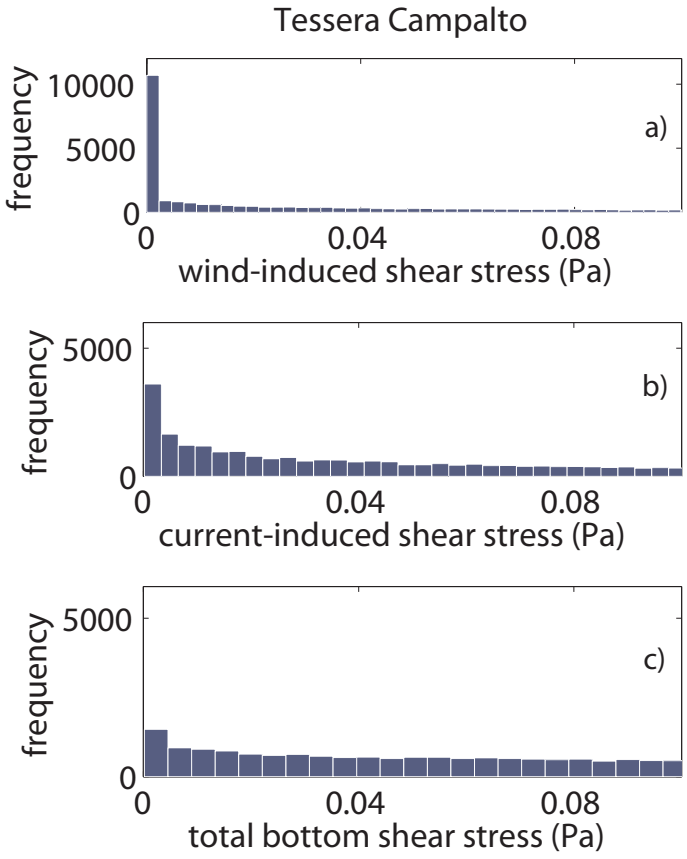

Figure 2.12: Frequency Distribution of bottom shear stresses for Tessera-Campalto site. a) wind-induced bottom shear stress distribution. b) current-induced bottom shear stresses. c) total shear stress distribution.

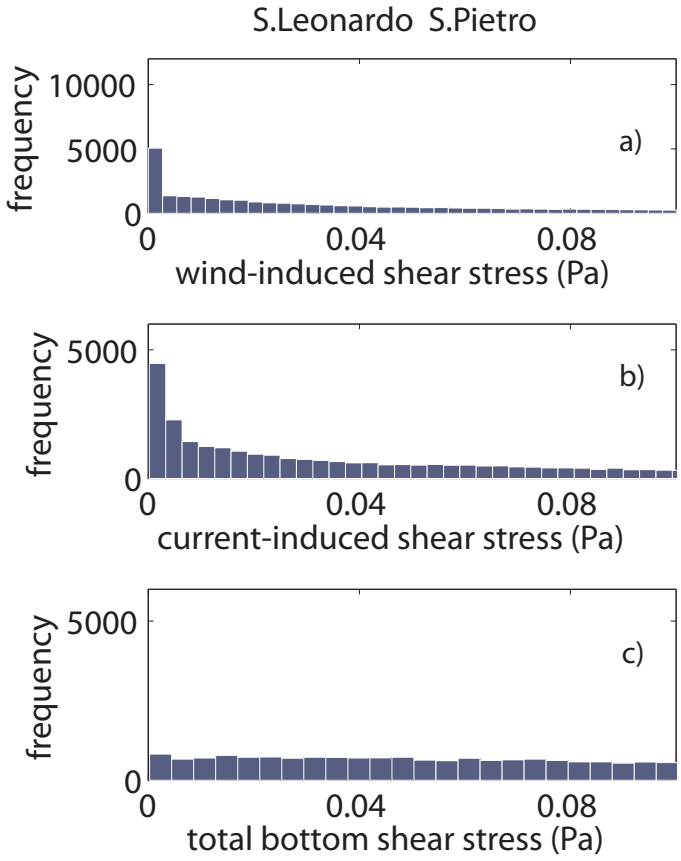

Figure 2.13: Frequency Distribution of bottom shear stresses for S.Leonardo-S.Pietro site. a) wind-induced bottom shear stress distribution. b) current-induced bottom shear stresses. c) total shear stress distribution.

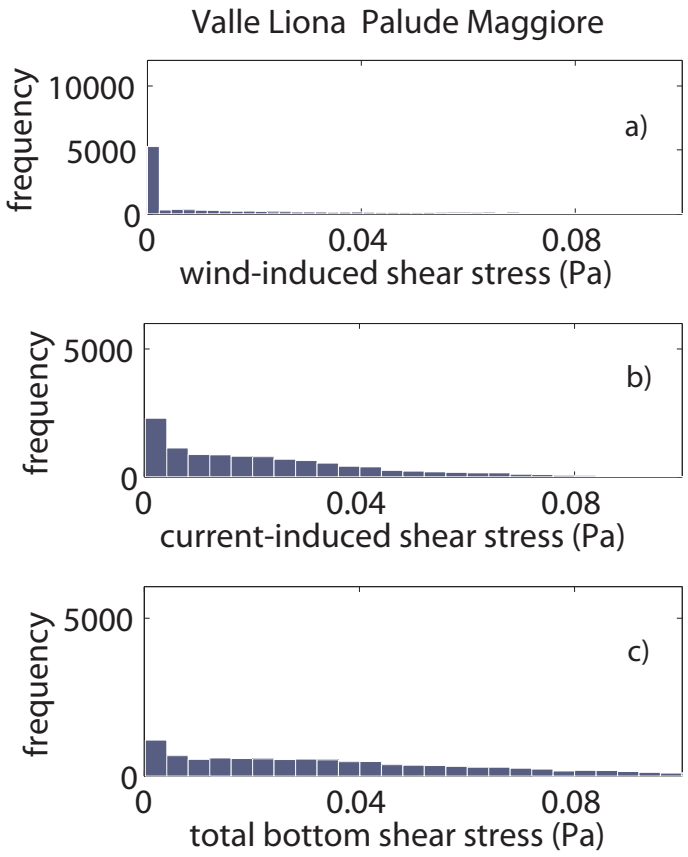

Figure 2.14: Frequency Distribution of bottom shear stresses for Valle Liona-Palude Maggiore site. a) wind-induced bottom shear stress distribution. b) current-induced bottom shear stresses. c) total shear stress distribution.

2.4.2 Bed Sediment Properties estimation

Once the total bottom shear stress have been computed, we proceed estimating the residual concentration, C_0, and the settling velocity, w_s by means of the linear fitting following as mentioned in section 2.3.3. The resulting linear fitting (eq. 2.22) of the points $D\frac{\partial C}{\partial t}$ vs C is shown in Figures 2.15-2.18.

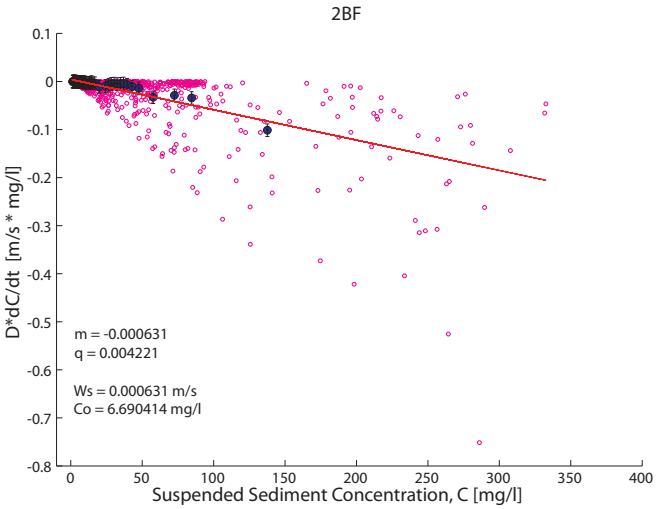

Figure 2.15: Linear Fitting of the points $D\frac{\partial C}{\partial t}$ vs C for 2BF site. A binning analysis is also performed to visualize the decreasing trend of the points and to reduce the large variability for high values of C.

We obtained values of w_s in the range $2.7 \cdot 10^{-4}\, m/s - 6.3 \cdot 10^{-4}\, m/s$, for all the stations (results are reported in Table 2.3). Our results show very low difference between the highest value, which belong to 2BF site possibly due to the presence of phanerogams, and the lowest values of w_s found in the stations Valle Liona-Palude Maggiore and S.Leonardo-S.Pietro.

Our results are in good general agreement with w_s estimates obtained by *in situ* devices (Amos *et al.*, 2004). In particular, all our values of w_s fall within the range of values obtained by Amos *et al.* (2004) at nearby locations. The value of the Tessera-Campalto stations, $w_s = 3.5 \cdot 10^{-4}\, m/s$, falls in the range $7.2 \cdot 10^{-5}\, m/s$-$1.3 \cdot 10^{-3}\, m/s$ in Amos *et al.* (2004). $w_s = 6.3 \cdot 10^{-4}\, m/s$ for the 2BF station falls within the range $w_s = 9 \cdot 10^{-5}\, m/s$-$7.3 \cdot 10^{-4}\, m/s$ obtained

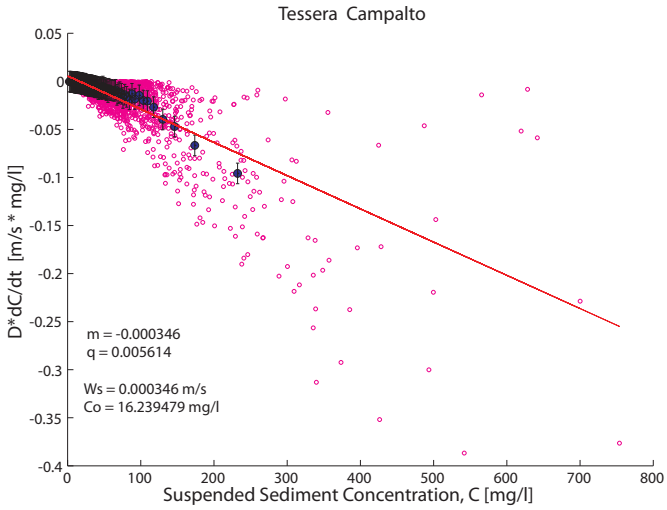

Figure 2.16: Linear Fitting of the points $D\frac{\partial C}{\partial t}$ vs C for Tessera-Campalto site. A binning analysis is also performed to visualize the decreasing trend of the points and to reduce the large variability for high values of C.

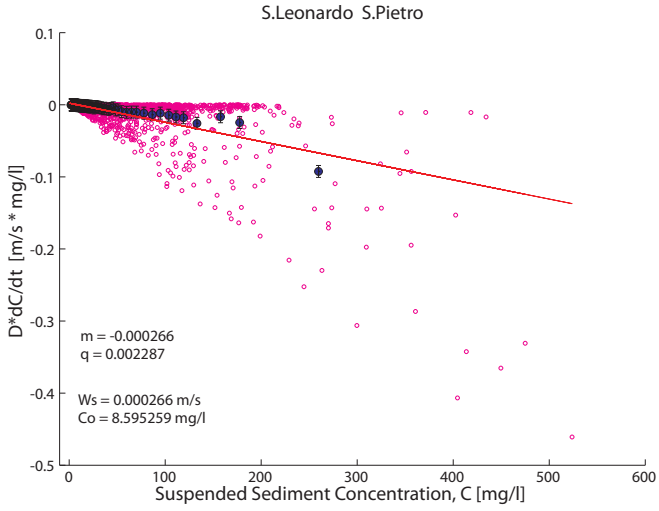

Figure 2.17: Linear Fitting of the points $D\frac{\partial C}{\partial t}$ vs C for S.Leonardo-S.Pietro site. A binning analysis is also performed to visualize the decreasing trend of the points and to reduce the large variability for high values of C.

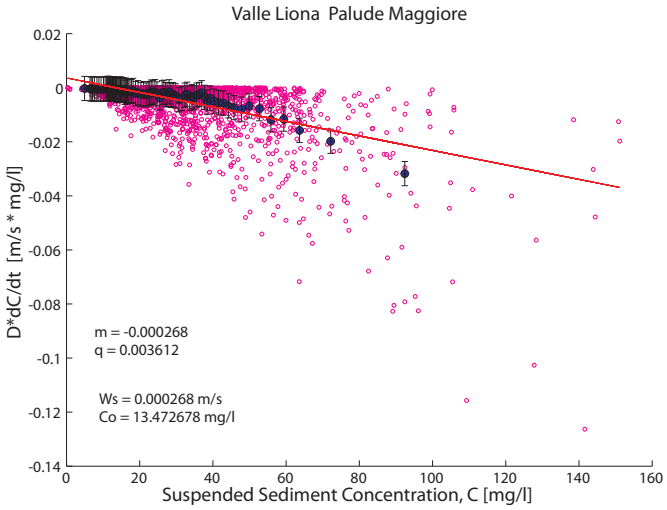

Figure 2.18: Linear Fitting of the points $D\frac{\partial C}{\partial t}$ vs C for Valle Liona-Palude Maggiore site. A binning analysis is also performed to visualize the decreasing trend of the points and to reduce the large variability for high values of C.

by Amos *et al.* (2004) at nearby locations. Our value for the S. Leonardo-S. Pietro stations, $w_s = 2.7 \cdot 10^{-4}\, m/s$, falls within the range $w_s = 6.7 \cdot 10^{-5}\, m/s$ - $2.8 \cdot 10^{-4}\, m/s$ provided by Amos *et al.* (2004), and the Valle Liona-Palude Maggiore stations, where we find $w_s = 2.7 \cdot 10^{-4}\, m/s$, falls within the range $w_s = 5 \cdot 10^{-5}\, m/s$ - $9.5 \cdot 10^{-4}\, m/s$ of Amos *et al.* (2004).

We also obtained reasonable values of residual suspended sediment concentration, C_0, which are supposed to remain in the flow and to never settle down in the range $6.7 - 16.2\ mg/l$ (see Table 2.3).

Moreover the values of w_s obtained from the linear fitting are slightly lower but still comparable with the mean values of the w_s distribution (see eq.2.23), computed on the basis of C_0 deduced by linear fitting. The relative frequency density for the instantaneous settling velocity is computed and plotted in Fig. 2.19, 2.20, 2.21, 2.22 (graphs above). From the settling velocity distribution a $16^{th} - 84^{th}$ percentile interval of values and the median settling velocity are deduced (see table 2.2):

Through eq.2.24 we compute the median sediment diameter, d_{50} (see table

Table 2.2: 16-84 percentile of settling velocity, median settling velocity, and median sediment diameter for the sites analyzed

site	16^{th} percentile w_s	84^{th} percentile w_s	median w_s	median d_{50}
	m/s	m/s	m/s	μm
Valle Liona-Palude Maggiore	$1.4 \cdot 10^{-5}$	$5.4 \cdot 10^{-4}$	$9.5 \cdot 10^{-4}$	17
Tessera-Campalto	$6.6 \cdot 10^{-5}$	$6.6 \cdot 10^{-4}$	$2.6 \cdot 10^{-4}$	27
2BF	$3.4 \cdot 10^{-5}$	$1.2 \cdot 10^{-3}$	$2 \cdot 10^{-4}$	36
S.Leonardo-S.Pietro	$2.5 \cdot 10^{-5}$	$6 \cdot 10^{-4}$	$1.3 \cdot 10^{-4}$	19

2.2), and the relative frequency density distributions are reported in Figures 2.19, 2.20, 2.21, 2.22 (graphs below).

We obtained values of the median sediment diameter, d_{50} in agreement with the values provided by CVN (2004), especially for 2BF, Tessera-Campalto and Valle Liona-Palude Maggiore sites, while for S.Leonardo-S.Pietro the value we obtained from the model is slightly lower. Anyway the results of sediment bed properties are consistent after increasing the d_{50} estimated for S.Leonardo-S.Pietro to 47 μm.

Finally by means of C_0 and w_s, computed by linear fitting, we compute the erosion rate, ϵ, for all observational intervals for which $\tau > \tau_c$.

Figures 2.23, 2.24, 2.25, 2.26 show respectively the values of the erosion rate vs the BSS, as obtained from eq. 2.1 for 2BF, Tessera-Campalto, S.Leonardo-S.Pietro, and Valle Liona-Palude Maggiore stations. As already mentioned to better identify the dependence of ϵ on τ and reduce noise, the data were partitioned into intervals of length 0.05 Pa, and all data falling within each interval were averaged to produce a binned representation of the relationship sought. Such a representation shows that ϵ does not depend on the BSS for values of τ smaller than a critical threshold, τ_c, consistently with the parameterization adopted for the erosion flux (Einstein and Krone, 1962), (Mehta, 1984), (Krone, 1987). Fitting the data allowed the estimation of τ_c and μ_e with the results listed in Table 2.3. The results are in line with what is expected for the sandy

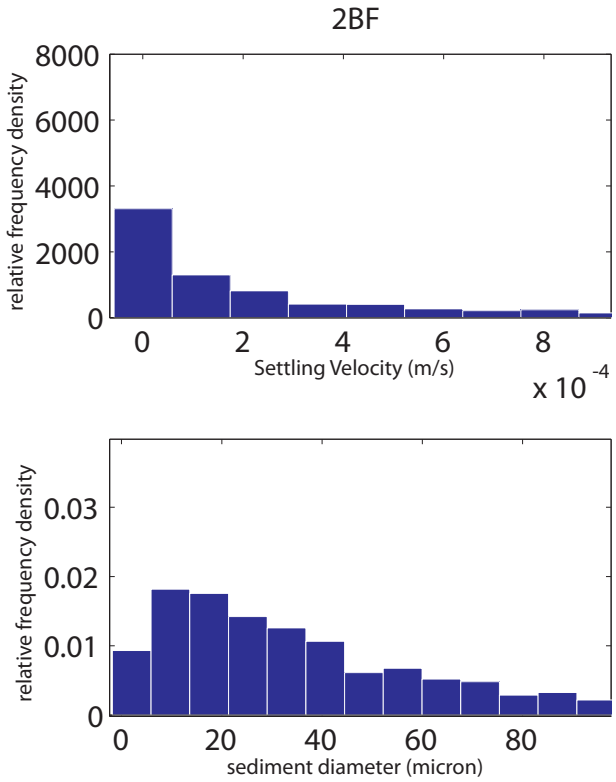

Figure 2.19: 2BF site. Frequency distribution of Settling Velocity, w_s (above) and Sediment Diameter, D_s (below)

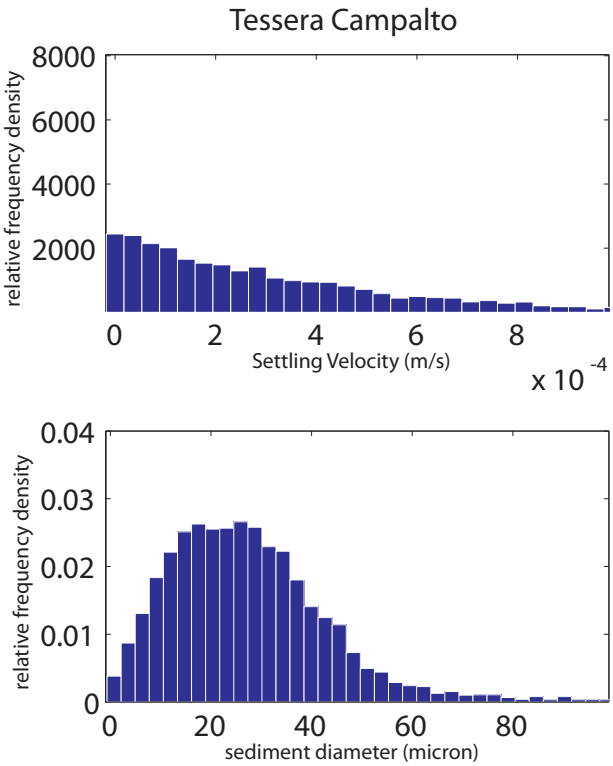

Figure 2.20: Tessera Campalto site. Frequency distribution of Settling Velocity, w_s (above) and Sediment Diameter, D_s (below)

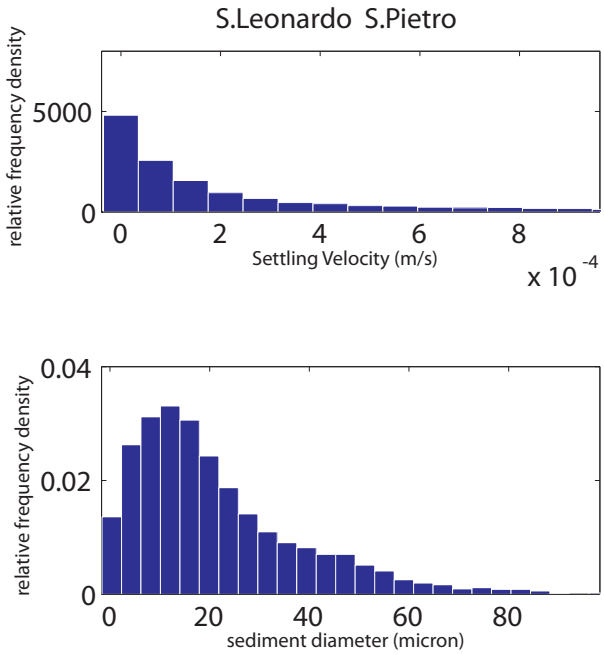

Figure 2.21: S.Leonardo S.Pietro site. Frequency distribution of Settling Velocity, w_s (above) and Sediment Diameter, D_s (below)

silt bottom sediments found at our sites (Houwing, 1999). It is informing to compare our estimates of the critical BSS with those obtained by Amos *et al.* (2004), Amos *et al.* (2010) at corresponding sites. The estimates of τ_c are in good agreement with those of Amos *et al.* (2004) both in the northern Venice lagoon (Valle Liona-Palude Maggiore, $\tau_c = 0.5Pa$, and Tessera-Campalto, $\tau_c = 0.2Pa$, where Amos *et al.* (2004) find values in the range $0.2\ Pa - 2.3\ Pa$) and at the southern site 2BF ($\tau_c = 0.3Pa$ is comparable with the values observed by Amos *et al.* (2004) in the range $0.4\ Pa - 1.6\ Pa$). In S. Leonardo-S. Pietro the resulting $\tau_c = 0.1Pa$ is instead smaller than the values in Amos *et al.* (2004) in the range $0.4\ Pa - 0.6\ Pa$. Our estimates of critical shear stresses do not count for the vegetation effect, such that our method underestimates the results for Palude Maggiore and S.Pietro, characterized by the presence of macroalgae, and Campalto and 2BF, characterized by the presence of phanerogams.

Finally values of the erosion parameter, μ_e in the range $2 \cdot 10^{-6}\, kg/sm^2$ - $3.1 \cdot 10^{-4}\, kg/sm^2$ are then obtained on the basis of the erosion Rate values, ϵ,

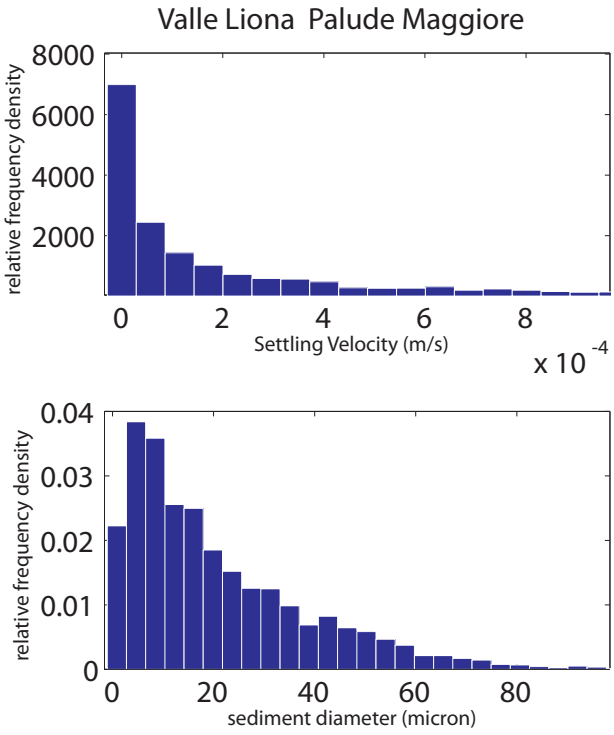

Figure 2.22: Valle Liona Palude Maggiore site. Frequency distribution of Settling Velocity, w_s (above) and Sediment Diameter, D_s (below)

Table 2.3: w_s, τ_c and μ_e values for the sites analyzed.

site	$w_s(m/s)$	$C_0(mg/l)$	μ_e (kg/sm^2)	τ_c (Pa)
Valle Liona-Palude Maggiore	$2.7 \cdot 10^{-4}$	13.5	$3.1 \cdot 10^{-4}$	0.5
Tessera-Campalto	$3.5 \cdot 10^{-4}$	16.2	$3.3 \cdot 10^{-5}$	0.2
2BF	$6.3 \cdot 10^{-4}$	6.7	$1.6 \cdot 10^{-4}$	0.3
S.Leonardo-S.Pietro	$2.7 \cdot 10^{-4}$	8.6	$2 \cdot 10^{-6}$	0.1

which, considering all our stations, are included in the interval $-1.4 \cdot 10^{-3} - 1.9 \cdot 10^{-3} kg/ms^2$. Erosion Rates are also comparable with the values measured *in situ* by benthic Sea Carousel (Amos *et al.*, 2010), whose minimum erosion rate is approximately constant around $1 \cdot 10^{-4} kg/ms^2$.

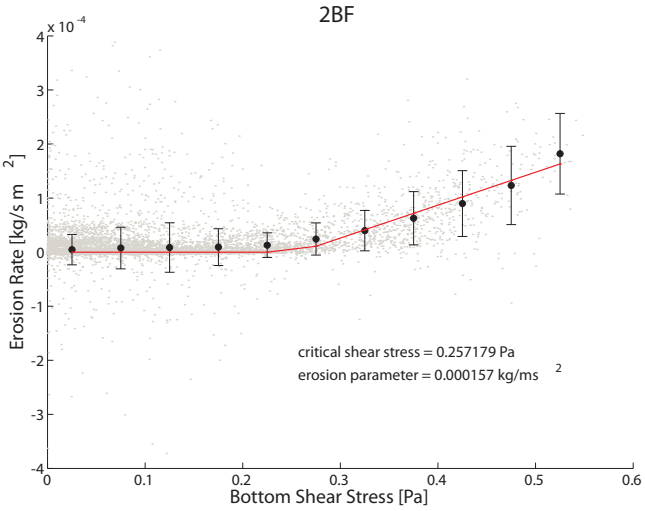

Figure 2.23: Mean value of the erosion rate (black circle) vs BSS for 2BF site. The red curve is the regression curve of the binned values.

For S.Leonardo-S.Pietro site the mean values of the erosion rate are approximately over a line parallel to the x-axis, such that the very low critical shear stress is due to the very soft slope chancing in correspondence of low bottom shear stresses.

For Valle Liona-Palude Maggiore site, the critical shear stress might be over-

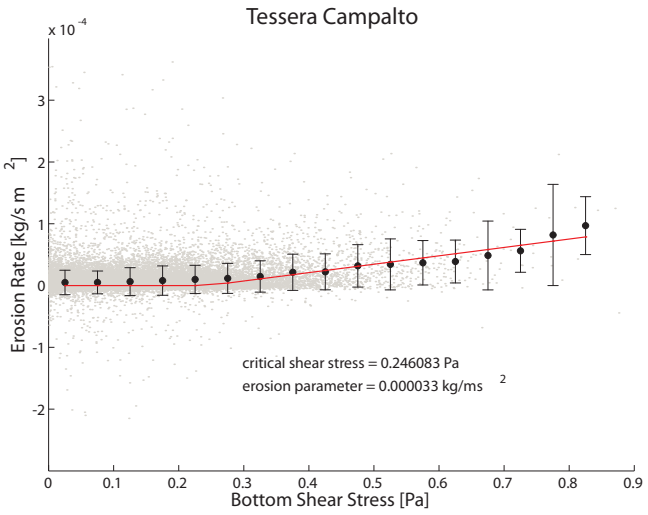

Figure 2.24: Mean value of the erosion rate (black circle) vs BSS for Tessera-Campalto site. The red curve is the regression curve of the binned values.

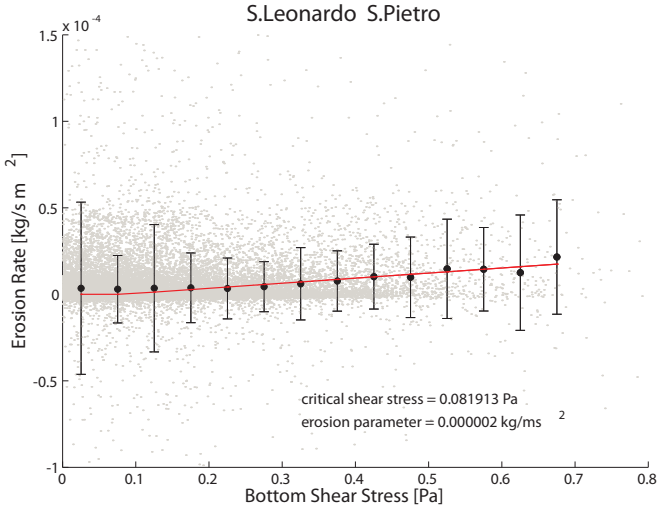

Figure 2.25: Mean value of the erosion rate (black circle) vs BSS for S.Leonardo-S.Pietro site. The red curve is the regression curve of the binned values.

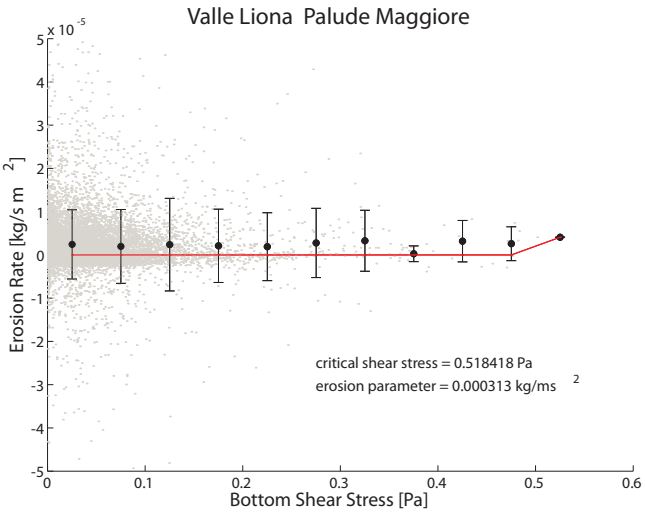

Figure 2.26: Mean value of the erosion rate (black circle) vs BSS for Valle Liona-Palude Maggiore site. The red curve is the regression curve of the binned values.

Table 2.4: Seasonal values of w_s, τ_c and μ_e for 2BF site.

	$w_s(m/s)$	$C_0(mg/l)$	μ_e (kg/sm^2)	τ_c (Pa)
winter	$2.3 \cdot 10^{-4}$	3.3	$3.1 \cdot 10^{-5}$	0.3
spring	$7.5 \cdot 10^{-4}$	1.92	$1.8 \cdot 10^{-5}$	0.4
summer	–	–	–	–
fall	$1.4 \cdot 10^{-4}$	5.2	$5 \cdot 10^{-4}$	0.4

estimated as resulting from a fitting carried out for few erosion rate values in correspondence of higher bottom shear stresses.

A seasonal analysis is also performed. Results are summarize in tables 2.4-2.7.

From results reported in tables 2.4-2.7 we may note that the highest values of w_s are found during summer-period for Valle Liona-Palude Maggiore and S.Leonardo-S.Pietro sites, while the lowest value of w_s are obtained for fall-period for 2BF site and winter-period for the other sites, suggesting that there can be a kind of couple of trend, as also observed by Amos *et al.* (2004): during summer time, when turbidity is lower, suspended sediment particles settle

Table 2.5: Seasonal values of w_s, τ_c and μ_e for Tessera-Campalto site.

	$w_s(m/s)$	$C_0(mg/l)$	μ_e (kg/sm^2)	τ_c (Pa)
winter	$2.5 \cdot 10^{-4}$	12.9	$9.7 \cdot 10^{-7}$	0.03
spring	$3.9 \cdot 10^{-4}$	18.6	$7.6 \cdot 10^{-6}$	0.1
summer	$3.1 \cdot 10^{-4}$	18.2	$3.7 \cdot 10^{-6}$	0.05
fall	$4.1 \cdot 10^{-4}$	14.7	$5.3 \cdot 10^{-5}$	0.25

Table 2.6: Seasonal values of w_s, τ_c and μ_e for S.Leonardo-S.Pietro site.

	$w_s(m/s)$	$C_0(mg/l)$	μ_e (kg/sm^2)	τ_c (Pa)
winter	$1.3 \cdot 10^{-4}$	4.9	$2.8 \cdot 10^{-9}$	0
spring	$3.5 \cdot 10^{-4}$	7.6	$1.5 \cdot 10^{-8}$	0
summer	$4.3 \cdot 10^{-4}$	8	$3.2 \cdot 10^{-6}$	0.1
fall	$1.5 \cdot 10^{-4}$	2.9	$2.2 \cdot 10^{-4}$	0.6

Table 2.7: Seasonal values of w_s, τ_c and μ_e for Valle Liona-Palude Maggiore site.

	$w_s(m/s)$	$C_0(mg/l)$	μ_e (kg/sm^2)	τ_c (Pa)
winter	$1.4 \cdot 10^{-4}$	5.1	$2 \cdot 10^{-4}$	0.6
spring	$3 \cdot 10^{-4}$	18	$4.5 \cdot 10^{-4}$	0.4
summer	$3.1 \cdot 10^{-4}$	13.8	$2 \cdot 10^{-4}$	0.6
fall	$1.5 \cdot 10^{-4}$	6.7	$1 \cdot 10^{-4}$	0.7

with higher velocity, while during fall-winter time, when turbidity is higher, suspended particles settle with a lower velocity. Finally τ_c and μ_e result higher mainly during fall-period, probably because of summer effects, while lower values of τ_c and μ_e are obtained mainly during winter-period.

2.5 Discussion

In summary, our estimates of bed sediment properties based on observations of water depth, SSC and wind velocity in the Venice lagoon give a settling velocity in the range $2.7 \cdot 10^{-4} - 6.3 \cdot 10^{-4} m/s$ and a residual concentration which is supposed to never settle in the lagoonal ecosystem in the range $6.7 - 16.2 mg/l$. These estimates correspond to deduced values for the critical shear stresses for erosion in the range $0.1 - 0.5 Pa$ and for the erosion parameter in the range $2 \cdot 10^{-6} - 3.1 \cdot 10^{-4} kg/ms^2$. Results are in line with what is expected for sandy-silt sediment and are consistent with independent *in situ* estimates. The method developed here appears to have distinct advantages over more traditional in situ procedures (e.g. the Sea Carousel or the Cohesive Strength Meter) because it does not interfere with the surface biofilm and provides a direct and quantitative physical estimate of the critical-shear stress. The method proposed is thus effective in studying and monitoring bed sediment properties on larger spatial scales and on longer temporal scales than those afforded by *in situ* observations.

Chapter 3

Experimental Analysis on Macroalgae

3.1 Macroalgae and sediment stability and flow dynamics

The growth of green macroalgal mats, and concomitant loss of seagrasses, is becoming increasingly common in many coastal and estuarine intertidal habitats (e.g. (Bolam *et al.*, 2000), (Silva *et al.*, 2004). Macroalgal mats influence flow and sediment dynamics, as well as chemical aspects and, as a result, can cause major changes to the ecology of the local ecosystem. This can determine a general decline in species richness resulting in changes in the numbers of shorebirds and fish. It therefore appears that detailed knowledge of the effect that macroalgal mats have on sediment stability and flow dynamics is required for understanding their impact on the ecology of inter-tidal sand flats. Such knowledge is also important for improving numerical models which predict tidal circulation. Macroalgae play a role in stabilizing intertidal sediments (Silva *et al.*, 2004), exerting a binding and baffling effect, thereby inhibiting erosion and maximizing

sedimentation from suspension (Frostick and McCave, 1979). Vegetation indeed creates regions of diminished bed stress that promote sedimentation and the retention of particles (Lopez and Garcia, 1998). Similar findings have been made in annular flume studies in which *Enteromorpha* caused physical protection of the bed and reduced sediment erosion by 60% at 10% coverage and 90% at 60% coverage (Romano *et al.*, 2003). The algal growth is restricted to bottom areas which are very shallow, at low water tide. These areas are subject to wave current flows capable of resuspending the sediments and so interacting with the macroalgae. It is expected that this interaction will change as low water depth varies in these shallow areas. However, no systematic study has been made on how twice daily changes in water depth associated with tidal rise and fall influence the effect of macroalgal mats on sediment transport, nor on its effects in wave-current flows. Macroalgal mats also have a key impact on the hydrodynamics of estuaries and coastal lagoons, but only two studies have attempted to examine this affect. Romano *et al.* (2003) revealed, using velocity measurements taken at one location over the bed, that *Enteromorpha* significantly increases flow resistance. It was shown to cause an overall reduction in mean flow velocity in the range 18% and 56% . Escartin and Aubrey (1995) used a recirculating flume to examine the influence of a mat of *Cladophora* on hydrodynamics and discovered that it caused an increase in roughness length and turbulent kinetic energy. However, both of these studies were made in current driven flows and they were unable to characterize both the temporal and spatial dynamics of the flow, which are key to fully understanding the momentum transfer mechanisms (Nikora *et al.*, 2001) and their influence on flow resistance (Nikora *et al.*, 2004). Therefore a more complete study is required on the influence of macroalgal mats on flow dynamics, by investigating wave-current flows which more accurately simulate conditions in estuarine channels. A depth-limited submerged canopy (Nepf and Vivoni, 2000), (Nepf and Ghisalberti, 2008) is here investigated, characterized by a vertical exchange zone (upper canopy) where the vertical turbulent exchange with the overlying water is dynamically significant

to the momentum balance and turbulence, and turbulence produced by mean shear at the top of the canopy is important; and a longitudinal exchange zone (lower canopy), where turbulence is generated locally by the canopy elements and the momentum badget is a balance of vegetative drag and pressure gradient. The objectives are to quantify, for the first time, under a range of water depths, the influence of high densities of *Enteromorpha sp.*, which are known to be highly tolerant to sedimentation (Eriksson and Johansson, 2005) on sediment and flow dynamics. This will help determine whether or not these algal mats promote bed stability and increase flow resistance and therefore reduce the risk of tidal flooding. This will be of benefit to coastal engineers and managers who are faced with the problem of devising novel strategies to accommodate tidal inundation.

3.2 Materials and Methods

3.2.1 Macroalgae species

The species selected for the present experiments was *Ulva intestinalis*, a common macroalga, which can be very abundant in nutrient enriched coastal systems. The area selected for collecting the large number of specimens needed was the National Natural Reserve of Budle Bay, in north-east England. Satellite images obtained from Google Earth (see Fig. 3.1), showed that in this bay the bed is covered by a continuous mat of macroalgae, close to the stream inlet and by a sparse cover in the intertidal flats in the middle section of the bay.

Figure 3.1: Satellite image obtained from Google Earth showing the area selected for collecting *Ulva intestinalis*: National Natural Reserve of Budle Bay, in north-east England. The bed is covered by a continuous mat of macroalgae close to the stream inlet, and by a sparse cover in the intertidal flats in the middle section of the bay.

This was the area selected for collecting the macroalgae as it allowed removing strands attached to pebbles (about 3 cm in diameter) and thus to transplant the macroalgae in the flume, as will be explained afterwards. The strands of *Ulva intestinalis* have a length ranging from 5 to 60 cm, mean length of 25 cm, mean width of 2.2 cm, mean weight of 49 g, and the clasts to which they are attached are 4 x 2 x 1 cm^3 in volume.

3.2.2 Sediment

The sediment chosen for the experiments is non cohesive artificial fine sand, characterized by a median grain size, D_{50} of $135\mu m$. The choice arises from the fact that the sediments collected at Budle Bay, where we sampled *U.intestinalis*, are characterized by similar grain size.

3.2.3 Facility and Instruments

Total Environment Simulator (TES)

The experiments were conducted in the Total Environment Simulator (TES) recirculating flume at the the University of Hull, UK. The flume tank is 11 m long and 2 m wide. A 20 cm horizontal and flat sediment layer has been created using the type of sediment specified above. The apparatus is supplied with flow and waves generators. The 2 m^3 study volume, where velocity, water surface and bed level were measured, is located approximately at the center of the flume, and limited by a prospect acrylic window, as depicted in Fig.3.2.

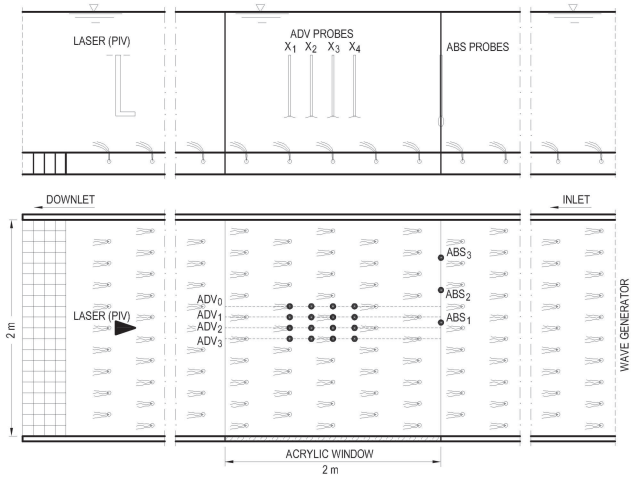

Figure 3.2: Side and plan view of the experimental flume. The study volume is located at the center of the flume, limited by a prospect wall.

Velocity Measurements: ADV

Velocity, water and bed level measurements were acquired in the sampling volume located approximately at the center of the flume, corresponding to the acrylic window wall used also for PIV observations (see Fig.3.2). The longitudinal, lateral and vertical velocity components, (u_x, u_y, u_z), were measured at a set of selected points by using four Nortek ADV, denoted as ADV0, ADV1, ADV2, ADV3 in Fig.3.2. These devices are located 1.2, 1.1, 1.0 and 0.9 m from the window wall and are moved longitudinally to monitor the along-flow positions X_1, X_2, X_3, X_4 located 0.8, 1.0, 1.2 and 1.4 m from the upstream limit of the measuring area. About 10 different points, depending on the flow depth, were sampled along a given vertical. At each measuring point the velocity components were sampled at a frequency of 25 Hz for an acquisition time of 120 s (implying a record containing about 3000 data).

Velocity Measurements: PIV

The spatial distribution of the mean flow along the center line of the channel was also measured through a three-dimensional PIV system, consisting of a vertical laser sheet located along the flume axis, and two submersible cameras, positioned outside the channel. The cameras, are directed towards the laser sheet emitted with two different angles and can be located at four different longitudinal positions, in order to cover the whole study area.

Bed and Flow Surface Measurements

Three ABS sensors (denoted as ABS3, ABS2, ABS1 in Fig.3.2) were located in a fixed position at the upstream end of the study area. These sensors operate at a frequency of 4 MHz, 2 MHz and 1 MHz respectively and record the bed surface position over time. The suspended sediment concentration can be estimated from backscatter intensity.

Sediment Transport Measurements

The total mass sediment transported along the flume was measured at the end of each run by determining the mass collected within traps located at the downstream end of the flume. Towards the end of each experiment pumped water samples were collected, to determine directly the concentration of suspended sediment.

Experimental Programme

The specimens of *U. intestinalis*, attached to the pebbles, once collected, were planted in the sand in a regular diamond pattern with lateral and longitudinal spacing equal to 20 cm and 40 cm, respectively, corresponding to a density of 12 points per m^2 (see Fig. 3.2). The large number of fronds attached to each pebble generated a fan shape covering up to 20 cm of bed.

The experimental programme involved several runs (Table 3.1) carried out by considering three different water depths D and uniform unidirectional flow

Table 3.1: Table summarizing the experimental programme, which consists of 12 runs conducted at three different water depths, with unidirectional flow conditions (M2,B2; M3,B3; M6,B6) and waves superposed to a uniform flow (M1,B1; M4,B4; M5,B5). M1, M2, M3, M4, M5, M6 denote the runs conducted over a bed covered by macroalgae, while B1, B2, B3, B4, B5, B6 denote the runs conducted over a bare bed.

	M1 B1	M2 B2	M3 B3	M4 B4	M5 B5	M6 B6
DEPTH (m)	0.22	0.22	0.31	0.31	0.25	0.25
FLOW VELOCITY (m/s)	0.25	0.25	0.25	0.25	0.25	0.25
FLOW RATE (l/s)	90	90	124	124	102	102
WAVE HEIGHT (m)	0.09	/	/	0.12	0.1	/
WAVE PERIOD (s)	1	/	/	1.1	1	/

conditions obtained by pumping a discharge Q such that to ensure a constant mean flow velocity, $U_x = 0.20ms^{-1}$. Experimental programme involve also runs conducted with wave superposed to a uniform flow, where the wave height, H and period, T were selected to represent fully developed wind wave conditions for each water depth.

A first series of experiments (hereinafter denoted as M) was conducted with the sandy bed covered with *Ulva intestinalis* and salt water. The macroalgae were then removed from the flume, the salt water was replaced with fresh water and, after flattening the bed, a second series of tests (hereinafter denoted as B) were carried out under the same hydrodynamic conditions of M runs.

The mean overall velocity in the longitudinal direction was computed as:

$$U_x = \frac{1}{A}\int u_x dA = \frac{Q}{A} \tag{3.1}$$

where A is the study area, equal to 4 m^2, and Q is the discharge of the study area.

3.3 Data Analysis

3.3.1 Introduction to Data Analysis

The ADV time series were firstly filtered, removing erroneous values and correcting for tilt and misalignment of the probes. In particular, the removed data consisted of i) measurements closer than 0.5 cm to the bed and ii) measurements containing more than 5% of bad data, namely points for which the mean and the minimum correlation were < 70 and < 50, while the mean and the minimum signal to noise ratio (SNR) were < 15 and < 5, respectively. A detection routine to remove spikes and other unusually large velocities was also used. The corrections for probe tilt and misalignment involved rotating the velocity vectors in the horizontal and vertical planes such that the average lateral and vertical velocities within the ADV measurement volume were zero.

After these preliminary operations, the mean velocity vector $\vec{\overline{u}}$ was calculated at each sampling point, by averaging over the acquisition time (120 s), adopting a statistical approach. For the experiments carried out without waves (M2-B2, M3-B3, M6-B6) the flow field is assumed to be statistically steady (the mean value does not change during time) and can be described by summing a mean term to a fluctuating term. The Reynolds Decomposition of the instantaneous velocity, $\vec{u}$ thus yields:

$$\vec{u} = \vec{\overline{u}} + \vec{u}' \tag{3.2}$$

where $\vec{u} = (u_x, u_y, u_z)$ is the turbulent velocity vector; $\vec{\overline{u}} = (\overline{u_x}, \overline{u_y}, \overline{u_z})$ is the mean velocity vector, and $\vec{u}' = (u_x', u_y', u_z')$ is the fluctuating velocity vector.

The Turbulent Kinetic Energy, e_k, which we refer to in the text afterwards is computed as follows:

$$e_k = \frac{u_x^{'2} + u_y^{'2} + u_z^{'2}}{2} \tag{3.3}$$

3.3.2 Overall distribution of the velocity field

Before analyzing in detail the specific features emerging from the analysis of the distributions of $\vec{\overline{u}}$ and $\vec{u'}$ it is worthwhile to discuss the overall structure of the velocity field obtained by operating a spatial interpolation of $\vec{\overline{u}}$ in an horizontal plane close to the bed and the three dimensional flow structure resulting from PIV measurements.

Correcting geometrically the photos taken during each experiment in the working area, we have reconstructed the spatial distribution of macroalgae and of bed topography in the measuring area. The location of the macroalgae, the bed topography and the velocity field shown in Figure 3.3 suggest a meandering of the flow around the lines of *Ulva Intestinalis* strands, generating a sort of small bedforms (2 centimetres high on average), properly around the point of attachment of the Enteromorpha. It is interesting to note that depths recorded by the ADVs over macroalgae are on average few millimeters higher than depths over bare bed, suggesting that the Enteromorpha tend to lay parallel to the bed during our experiments moving sinusoidally with the flow, unlike the great majority of experiments carried out in laboratory flumes with other plants.

Figure 3.4 shows the velocity field along a longitudinal transect obtained by plotting the vertical velocity profile measured by ADV0 at four locations over the contour plot of the cross-stream velocity. We can clearly note the flow in the layer close to the bottom is meandering around Enteromorpha strands.

We report here few examples of the 3D mean velocity field resulting from mean velocity vector ($\vec{\overline{u}}$), which will be used to relate the flow field to the degree of bio-stabilization to the relevant flow parameters. While figure 3.7 refers to run M1, in which waves are superposed to a unidirectional flow (see Table. 3.1), while Figures 3.6 and 3.5 refer respectively to runs M2, M3, characterized by

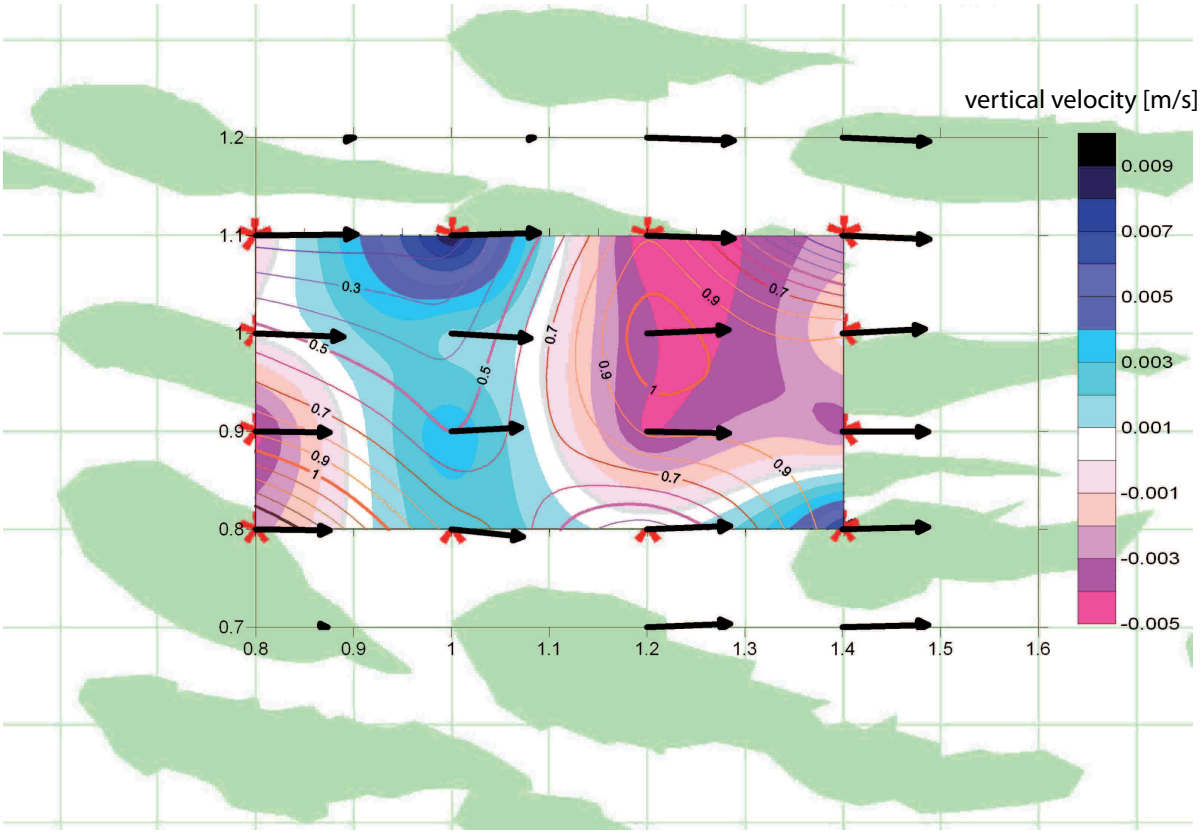

Figure 3.3: run M3, depth level 0.02 m. Areas covered by macroalgae (in green) together with the bed forms elevation (bathymetric lines) and the velocity vectors (the contour fill represents the magnitude of the velocity vector by spatial interpolation). All units are expressed in meters, except for bathimetric lines which are in centimeters. Flow is from left to the right.

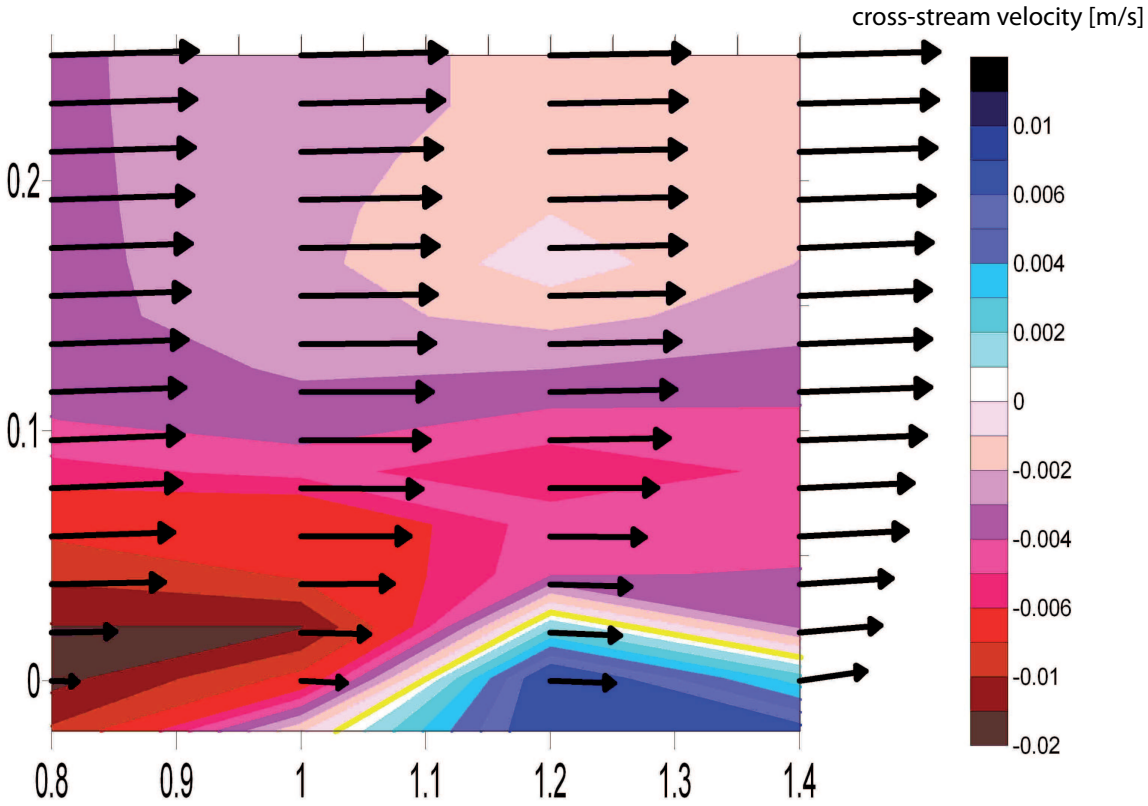

Figure 3.4: run M3. The vertical velocity profile of ADV0 is plotted over the contour plot, which represents the cross-stream velocity. All units are expressed in meters.

unidirectional flow hydrodynamic conditions. According to Fig. 3.3 discussed in the previous section, and assuming x-axis=downstream direction, y-axis=cross-stream direction, macroalgae are present at points (x=1, y=0.8); (x=1.4, y=1); (x=1.6, y=1); (x=1.4, y=1.4), denoted by yellow circles. In these points the velocity vectors attain a lower magnitude, demonstrating the role of macroalgae in decreasing the mean flow velocity close to the bed.

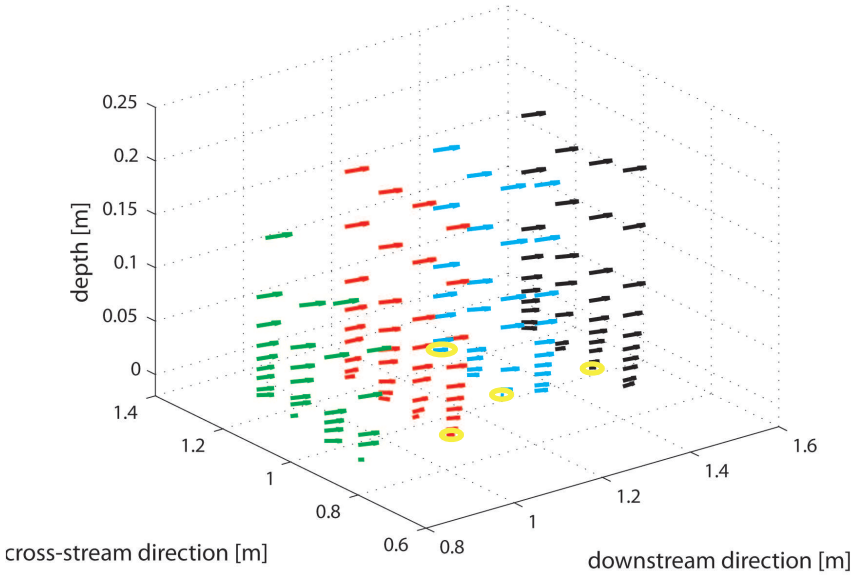

Figure 3.5: 3D velocity vector field for M3 run (unidirectional flow hydrodynamic conditions)

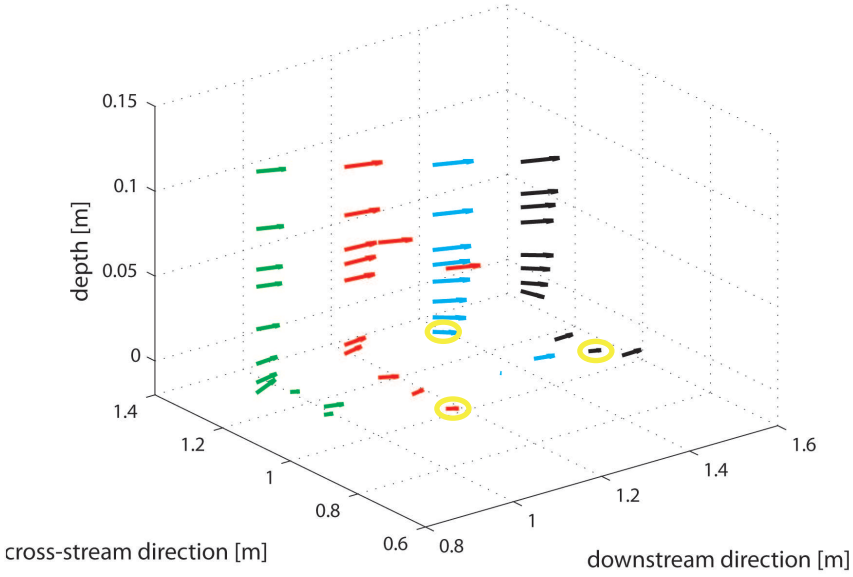

Figure 3.6: 3D velocity vector field for M2 run (unidirectional flow hydrodynamic conditions)

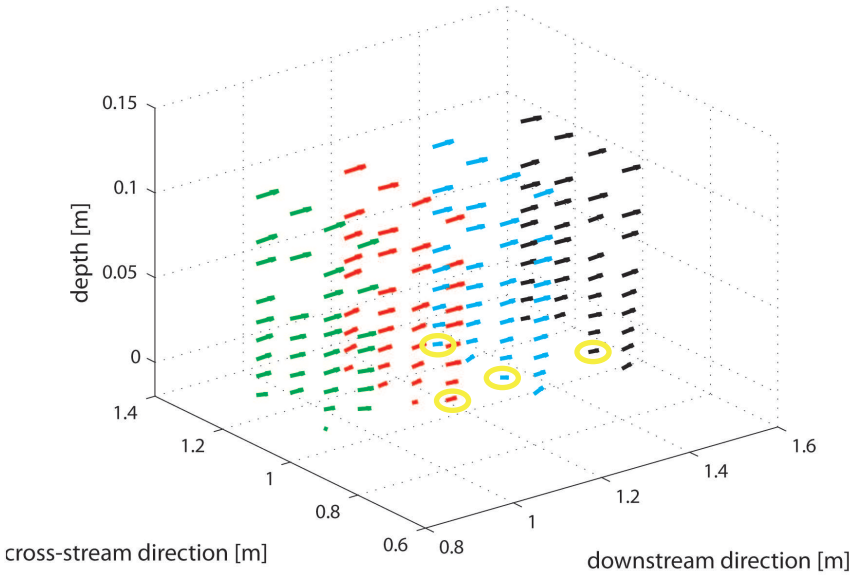

Figure 3.7: 3D velocity vector field for M1 run (waves superposed over a unidirectional flow hydrodynamic conditions)

Table 3.2: Mass collected within traps at the end of runs conducted over a macroalgae bed and over a bare bed.

test number	sediment transported run over macroalgae $kg/m/h$	sediment transported run over bare bed $kg/m/h$
1	3.65	4.46
2	0.00	0.30
3	0.02	0.22
4	4.42	5.56
5	0.27	5.45
6	5.89	5.40

3.3.3 Sediment Transport Data

A sediment transport analysis is briefly carried out on the basis of sediment traps data collected after each run. As it is possible to observe in table 3.2, the value of sediment transported for run with macroalgae is generally lower than the corresponding value for runs conducted over bare bed, demonstrating that macroalgae play a role in trapping sediment transported along the flume. This result is much more evident for test conducted with unidirectional flow conditions and waves superposed to a uniform flow (M1-B1, M4-B4, M5-B5).

3.3.4 PIV Analysis

Here we report a few images obtained by PIV data, in run M5 (waves superposed on unidirectional flow and over a macroalgae bed). The side view image of Fig.3.8 reports the downstream and vertical velocity vectors over photos taken by the cameras. Two distinct layers clearly appear: one over the macroal-

gae, characterized by nearly uniform conditions, and the other one through the macroalgae, exhibiting a definitely lesser uniform flow. In Figure 3.9 the downstream and vertical velocity vectors are plotted over a contour fill plot showing the velocity magnitude: it clearly appears a significant decrease of the velocity magnitude in correspondence of macroalgae. Figure reports 3.10 the downstream and vertical velocity vectors plotted over a contour fill plot showing the Turbulent Kinetic Energy. The areas characterized by the highest Turbulent Kinetic Energy, e_k (see Eq.3.3) correspond to macroalgae locations.

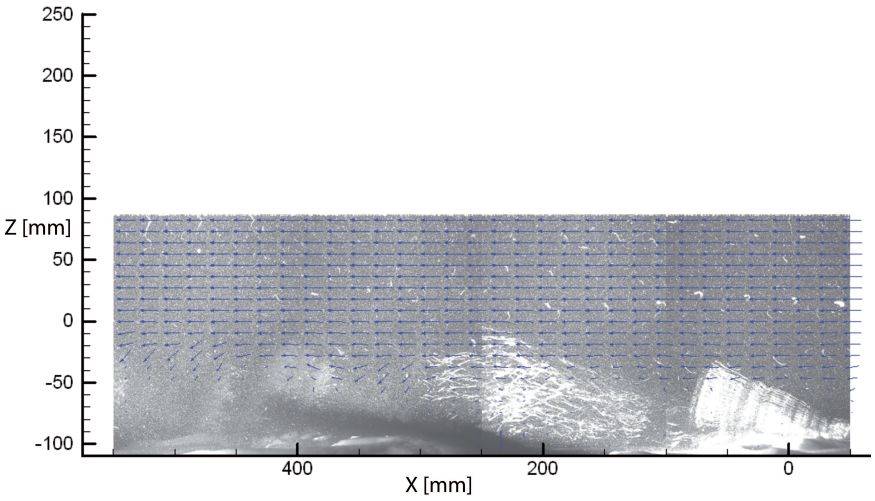

Figure 3.8: run M5. Side view image of the downstream and vertical velocity vectors superposed to photos taken by cameras (flow goes from right to left).

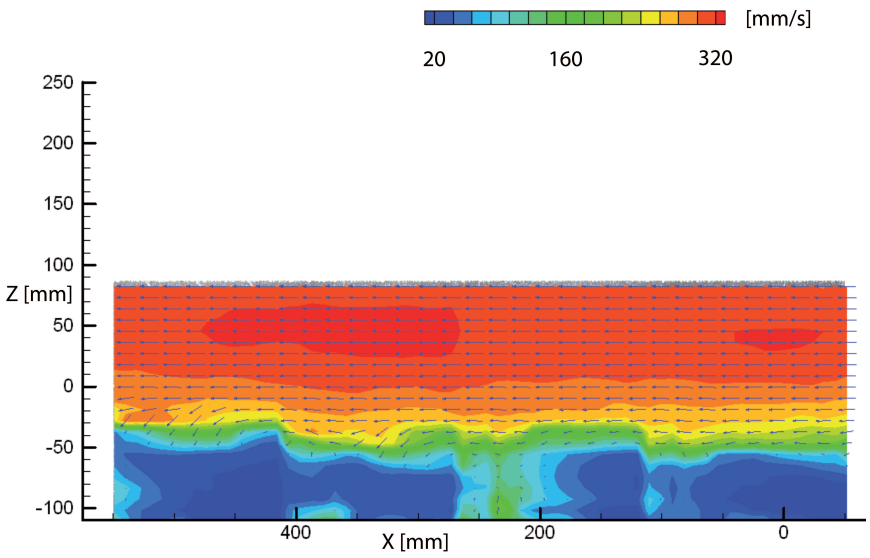

Figure 3.9: run M5. Side view image of the downstream and vertical velocity vectors plotted over a contour fill plot showing velocity magnitude (flow from right to left).

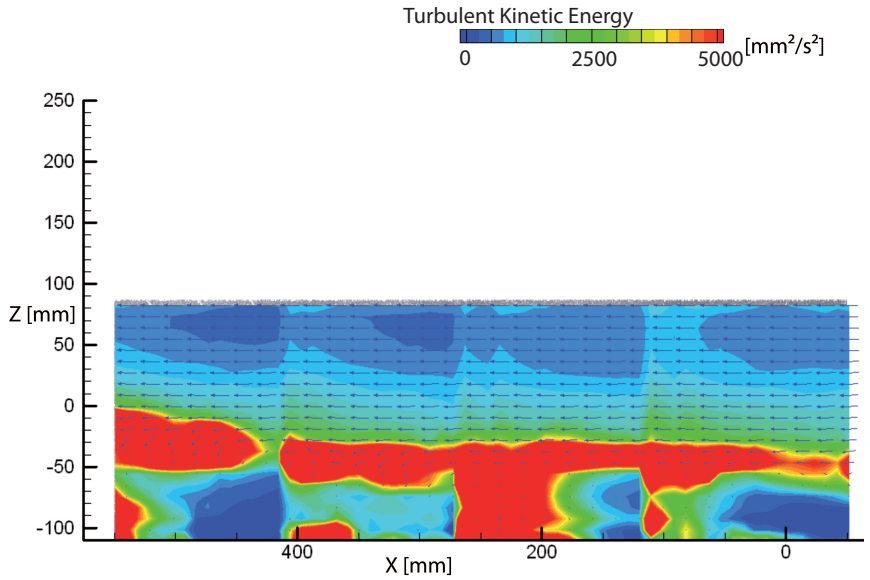

Figure 3.10: run M5. Side view image of the downstream and vertical velocity vectors plotted over a contour fill plot showing the Turbulent Kinetic Energy.

3.3.5 Autocorrelation Analysis

In order to quantify the features of turbulence and to determine the time interval over which computing the averages of the turbulent velocity components, we compute time autocorrelation of the longitudinal component of the fluctuating velocity, $u_x^{'}$. This Eulerian correlation relates the values of $u_x^{'}$ measured at a fixed point at two different instants t and $t+\tau$. Assuming that the mean flow is homogeneous and steady, the coefficient the Eulerian correlation is expressed as (Hinze, 1959):

$$R_t(\tau) = \overline{u_x'(t) \cdot u_x'(t+\tau)} \tag{3.4}$$

where the overbar denotes the average taken with respect to time t, while τ is the time lag. Figures 3.11 to 3.14 report the autocorrelation functions for the longitudinal direction, $u_x^{'}$ for both a uniform flow run with macroalgae, M3 and the relative one without macroalgae, B3.

Figures 3.11 and 3.12 refer to a depth level (0.15 m) close to the surface, while figures 3.13 and 3.14 refer to a depth level (0.03 m) close to the bottom, i.e. within the macroalgae layer.

Graphs (a) in Fig. 3.11-3.14 show the autocorrelation curves forr a 20 s time period: four curves corresponding to four ADVs in the X_1 ($0.8m$ from the upstream limit of the measuring area) location for Fig. 3.11 and 3.13, while sixteen curves corresponding to four ADVs in the X_1, X_2, X_3, X_3 locations (see section 3.2.3) for Fig. 3.12 and 3.14.

In order to better visualize the decreasing trend of $R_t(\tau)$ and better identify the intersection of $R_t(\tau)$ with the x-axis, a spatial average of the autocorrelation curves (binning analysis) has been performed: a mean value among the four/sixteen $R_t(\tau)$ functions has been computed for several τ intervals, as reported in Fig. 3.11-3.14 (b).

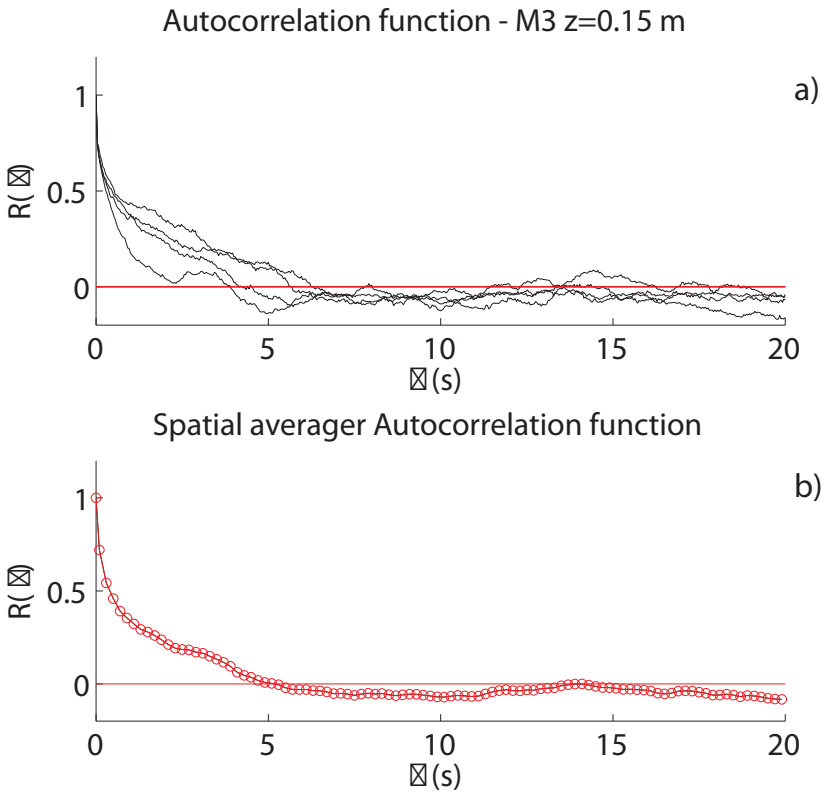

Figure 3.11: run M3 (uniform flow over a macroalgae bed) at the depth level z=0.15 m. a) plot of four autocorrelation curves corresponding to four ADVs in the X_1 ($0.8m$ from the upstream limit of the measuring area) location. b) spatial average autocorrelation function resulting from the mean value among the four $R_t(\tau)$ in a) for several τ interval

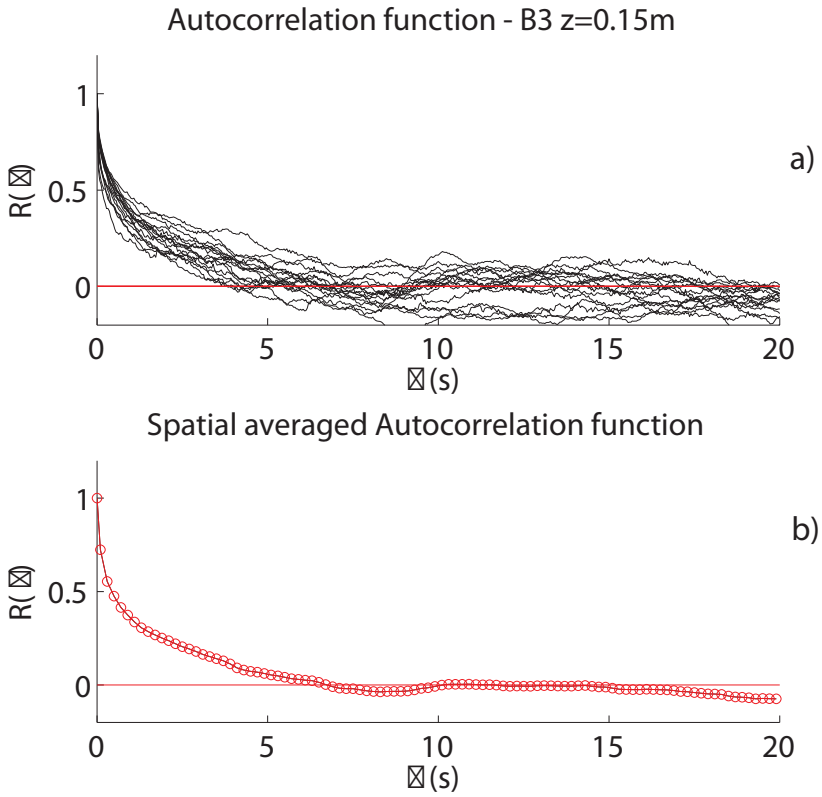

Figure 3.12: run B3 (uniform flow over a bare bed) at the depth level z=0.15 m. a) plot of sixteen autocorrelation curves corresponding to sixteen ADVs in the X_1, X_2, X_3, X_3 locations. b) spatial average autocorrelation function resulting from the mean value among the sixteen $R_t(\tau)$ in a) for several τ interval

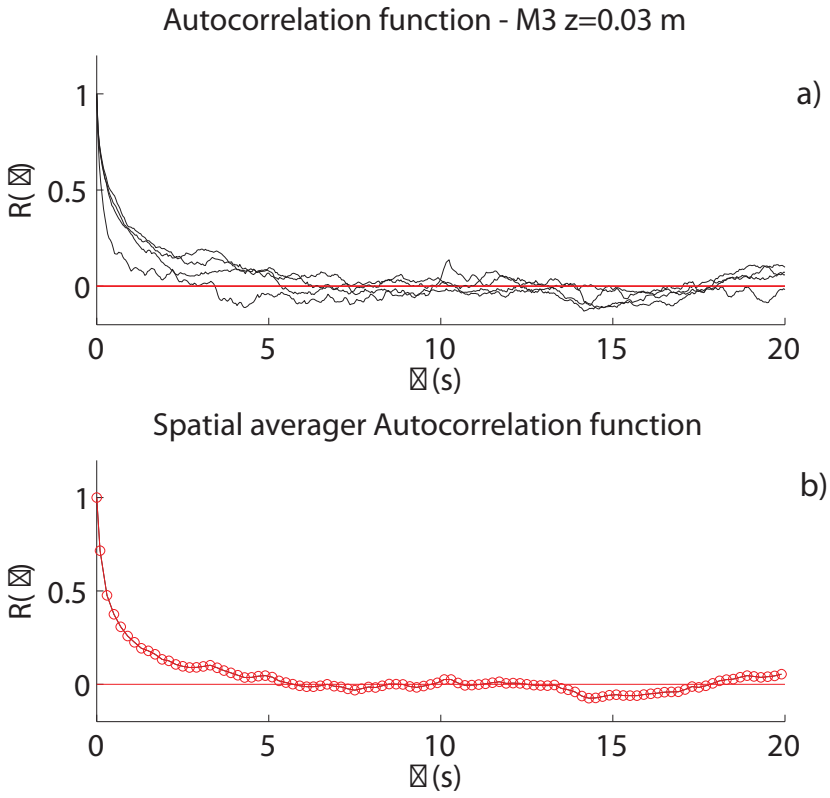

Figure 3.13: run M3 (uniform flow over a macroalgae bed) at the depth level z=0.03 m. a) plot of four autocorrelation curves corresponding to four ADVs in the X_1 ($0.8m$ from the upstream limit of the measuring area) location. b) spatial average autocorrelation function resulting from the mean value among the four $R_t(\tau)$ in a) for several τ interval

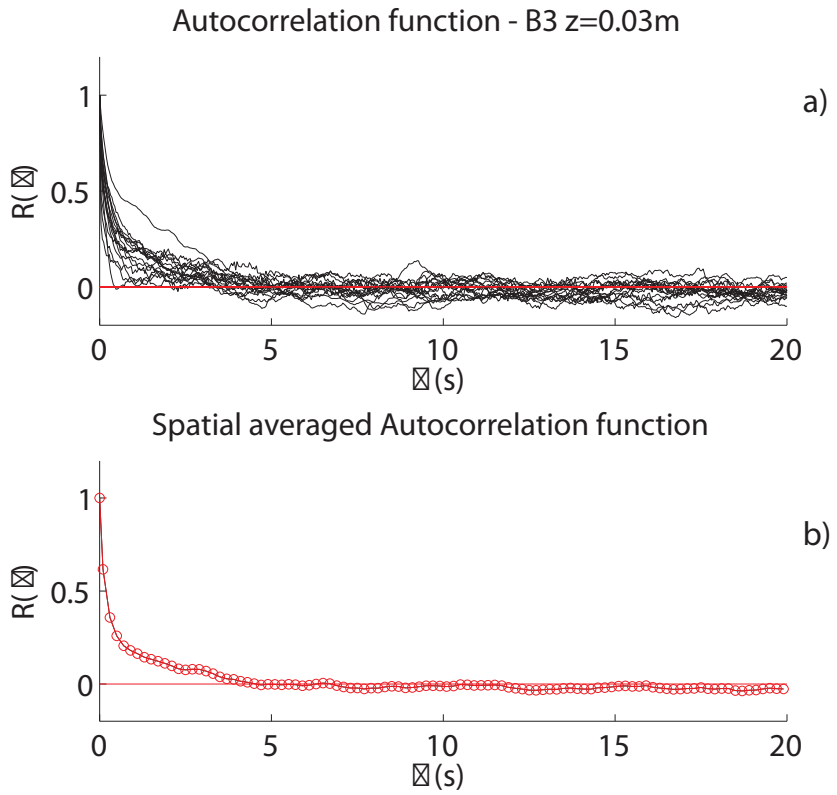

Figure 3.14: run B3 (uniform flow over a bare bed) at the depth level z=0.03 m. a) plot of sixteen autocorrelation curves corresponding to sixteen ADVs in the X_1, X_2, X_3, X_3 locations. b) spatial average autocorrelation function resulting from the mean value among the sixteen $R_t(\tau)$ in a) for several τ interval

In order to define the macroscales of the eddies which characterize the energy spectrum at high frequencies, we compute the Time Macroscale of vortex, τ_E (eq. 3.5) from the autocorrelation function, $R_t(\tau)$.

$$\tau_E = \int_0^\infty R_t(\tau) d\tau \tag{3.5}$$

By means of the trapezoid rule the integral of the autocorrelation function (eq. 3.5) is computed and the resulting Time Macroscale, τ_E for M3 and B3 runs at each depth level recorded by ADVs are reported in Table 3.3.

By means of the Taylor's hypothesis applied to relate temporal to spatial fluctuations in turbulent flow, the Spatial Macroscale of vortex, L_E (eq. 3.6) is now deduced, on the basis of the mean velocity value, $\overline{u_x}$ computed at each depth level, and the Time Macroscale, τ_E (see table 3.3 also for $\overline{u_x}$ and L_E results).

$$L_E = \overline{u_x}\tau(E) \tag{3.6}$$

From results in Table 3.3, we may infer that spatial averaged mean velocity over a macroalgae is generally lower than $\overline{u_x}$ over a bare bed, suggesting that macroalgae act decreasing the mean flow velocity. Results also show that the Temporal and Spatial Macroscale over a macroalgae bed are generally higher than the relative Macroscales over a bare bed. The vortex scales are bigger in the former case, suggesting that macroalgae strongly interact with the turbulence structure.

A summary of the Spatial Macroscale presented in table 3.3 is show in Fig.3.15 where the Spatial Macroscale normalized by the water depth, D (0.31 m for M3 and B3 run) is plotted over the depth level, z normalized by the water depth, D.

Table 3.3: run M3, carried out with uniform flow conditions and macroalgae, and the relative one without macroalgae, B3. Eulerian Temporal Macroscale, τ_E, Eulerian Spatial Macroscale, L_E, and spatial averaged mean velocity, $\overline{u_x}$

depth level, z	M3 τ_E	B3 τ_E	M3 L_E	B3 L_E	M3 $\overline{u_x}$	B3 $\overline{u_x}$
m	s	s	m	m	m/s	m/s
0.2	-	0.20	-	0.06	-	0.3
0.15	-	0.21	-	0.06	-	0.29
0.12	0.17	-	0.05	-	0.29	-
0.1	-	0.26	-	0.07	-	0.28
0.09	0.29	-	0.08	-	0.27	-
0.07	0.26	0.23	0.07	0.06	0.26	0.26
0.06	0.30	-	0.07	-	0.24	-
0.05	0.16	0.17	0.04	0.04	0.23	0.24
0.04	0.18	0.10	0.04	0.02	0.19	0.23
0.03	0.21	0.12	0.03	0.02	0.17	0.20
0.02	-	0.17	-	0.03	-	0.18
0.01	0.15	0.13	0.02	0.02	0.15	0.17
0	0.11	0.05	0.01	0.002	0.09	0.05

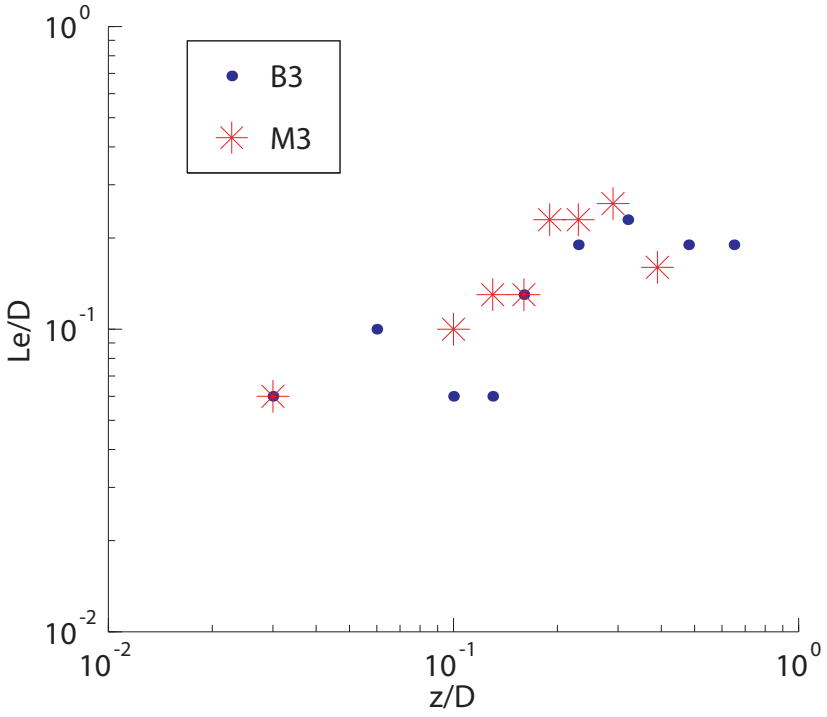

Figure 3.15: Spatial Macroscale normalized by the water depth, D (0.31 m for M3 and B3 run) is plotted over the depth level, z normalized by the water depth, D

3.3.6 Vertical Distribution of the longitudinal Velocity

In fully developed turbulent flows occurring over a rough wall, the vertical distribution of the longitudinal velocity averaged over turbulence is typically well approximated by a logarithmic law of the form (Hinze, 1959):

$$\frac{\overline{u_x}}{u^*} = 5.75 log \frac{z}{e_s} + 8.5 \tag{3.7}$$

where u^* is the friction velocity, e_s is the Nikuradse roughness parameter and z is the elevation over the mean bed surface.
In order to analyze how this profile modifies owing to the presence of macroalgae, $\overline{u}_x$ has been plotted versus z in a log-log plot 3.16.

We have already seen that in the presence of vegetation two distinct flow layers are present (see Fig.3.8-3.9). The logarithmic distribution of velocity has been stated only in the upper layer, i.e., outside the macroalgae layer over topping the sediment bed. The velocity profiles in presence of bare bed are characterized by a steeper growth (see Fig. 3.16 a). In particular, the difference is remarkable in runs M6-B6.

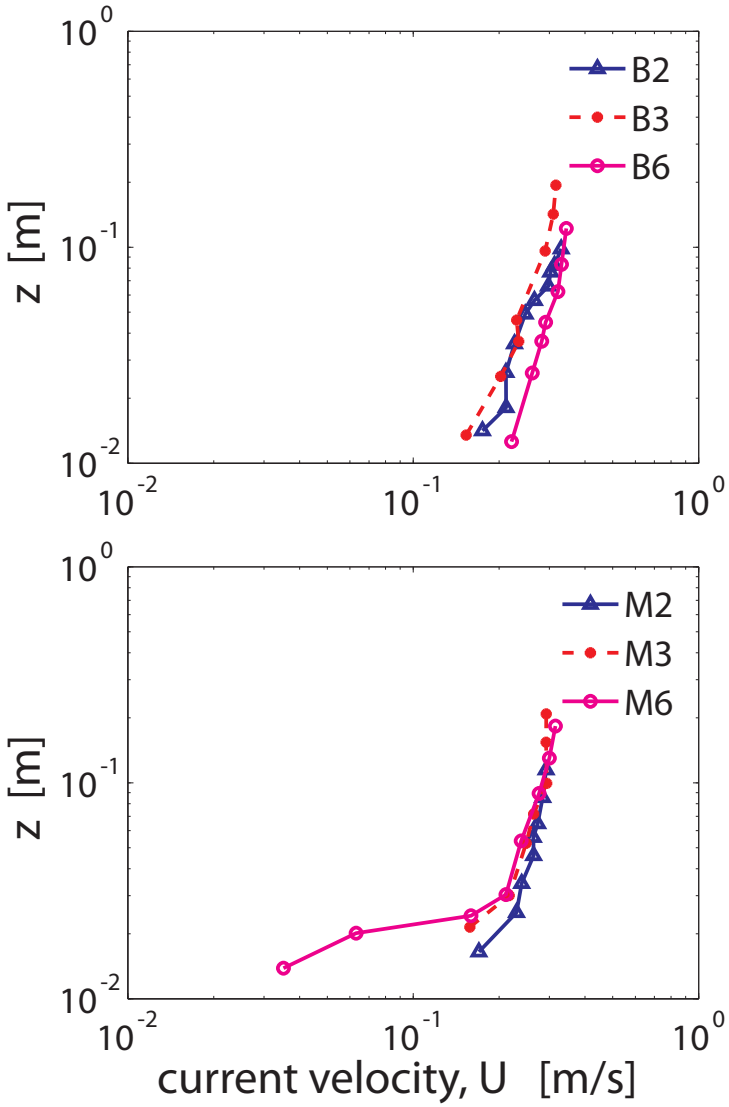

Figure 3.16: Vertical distribution of the longitudinal velocity component, averaged over turbulence, $\overline{u}_x$ observed in runs 2, 3 and 6 carried out with a) a bare and b) a macroalgae covered sandy bed. The investigated vertical is located just over a macroalgae stem.

Shear Velocity and Nikuradse Roughness

In order to quantify the differences/similarities between the vertical distributions of $\overline{u}_x$, we have determined u_* and e_s by plotting the quantity $5.75log_{10}(z)$ as a function of $\overline{u}_x$ in a log-log plot. A linear fitting of the experimental data has been performed and the correlation coefficient measuring the reliability of the fitting has been estimated. The slope m and the intercept b of the straight fitting line allow us to estimate the friction $u_* = 1/m$ and the roughness coefficient $e_s = 10^{(b+8.5)/5.75}$. For each run we obtained 16 fitting lines (one for each vertical measured through ADV). We can link each fitting to a specific location of the monitored vertical: over sand, over the attachment points of a macroalga, over a macroalga (see Figure 3.3). A typical example of this analysis is reported in Figure 3.17. We report here a few examples (Figures 3.17 and 3.18) relative to ADV1, for runs carried out under uniform flow conditions (runs M3, M6 over macroalgae bed, are compared with runs B3, B6 over bare bed).

It clearly appears that the presence of a stem leads to a significant departure of the velocity profile from the logarithmic one close to the bed, while the upper part of the velocity profile would suggest an appreciable increase of roughness and a slightly larger friction velocity. On the other hand, direct visual observation of the sandy bed indicate that macroalgae inhibit the formation of bedforms, thus implying a reduction of the overall bed friction.

A summary of all u^* and e_s resulting from the analysis of the six runs carried out under uniform flow conditions (M2 and B2, M3 and B3, M6 and B6) is reported in Table 3.19, where the averages of both parameters are computed for the three groups of points (over sand, over attachment points of macroalgae, and over macroalgae).

The presence of a stem leads to a significant departure of the velocity profile from the logarithmic one close to the bed, while the upper part of the velocity

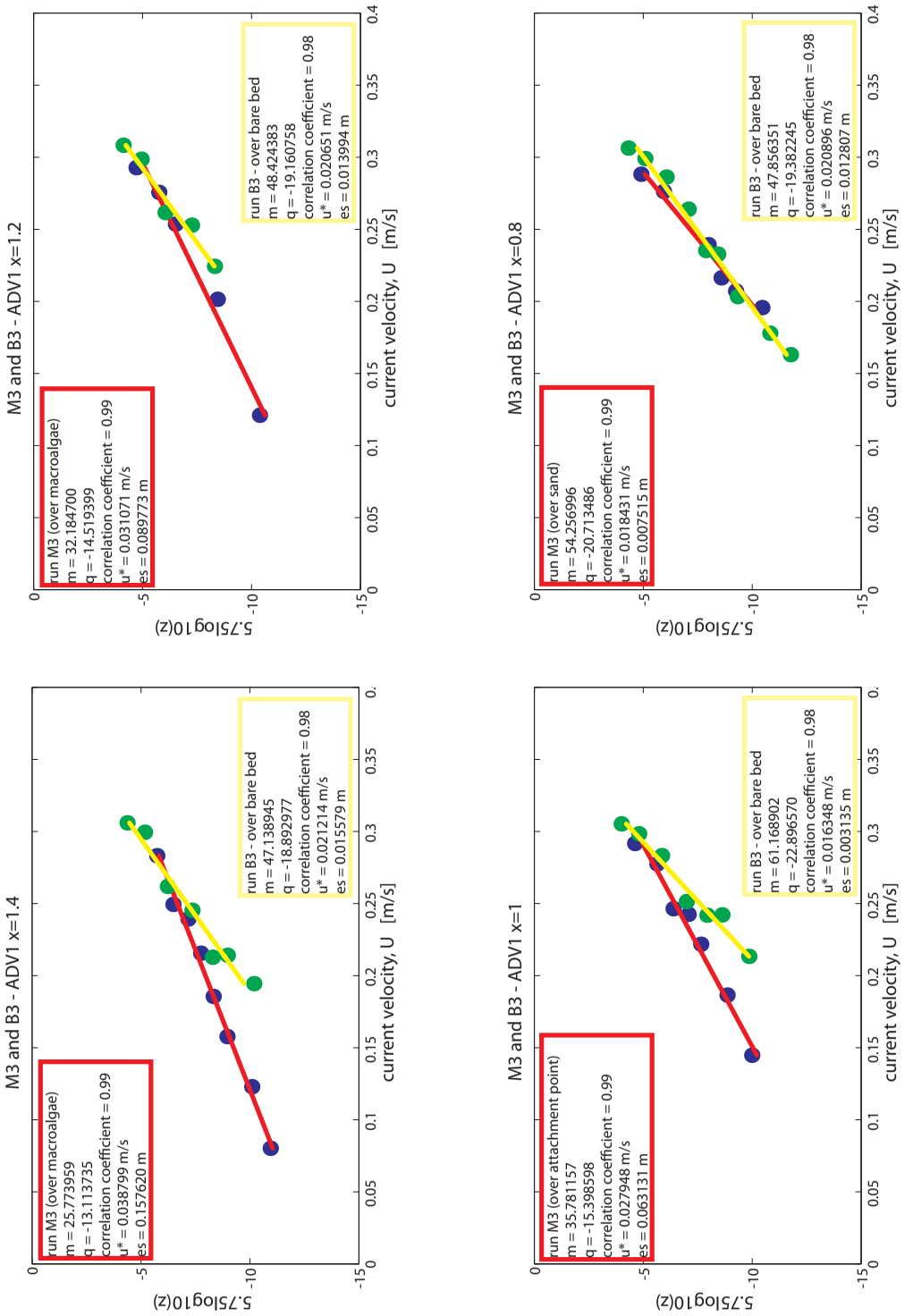

Figure 3.17: Fitting of experimental data using the logarithmic law (Eq. 3.7) and estimate of the friction velocity u_* and of the roughness factor e_s. The hydraulic conditions are those of run 3 and the data refer to ADV1. Plates a), b), c) and d) refer to longitudinal locations denoted as X_1 X_2, X_3 and X_4 in Figure 3.2

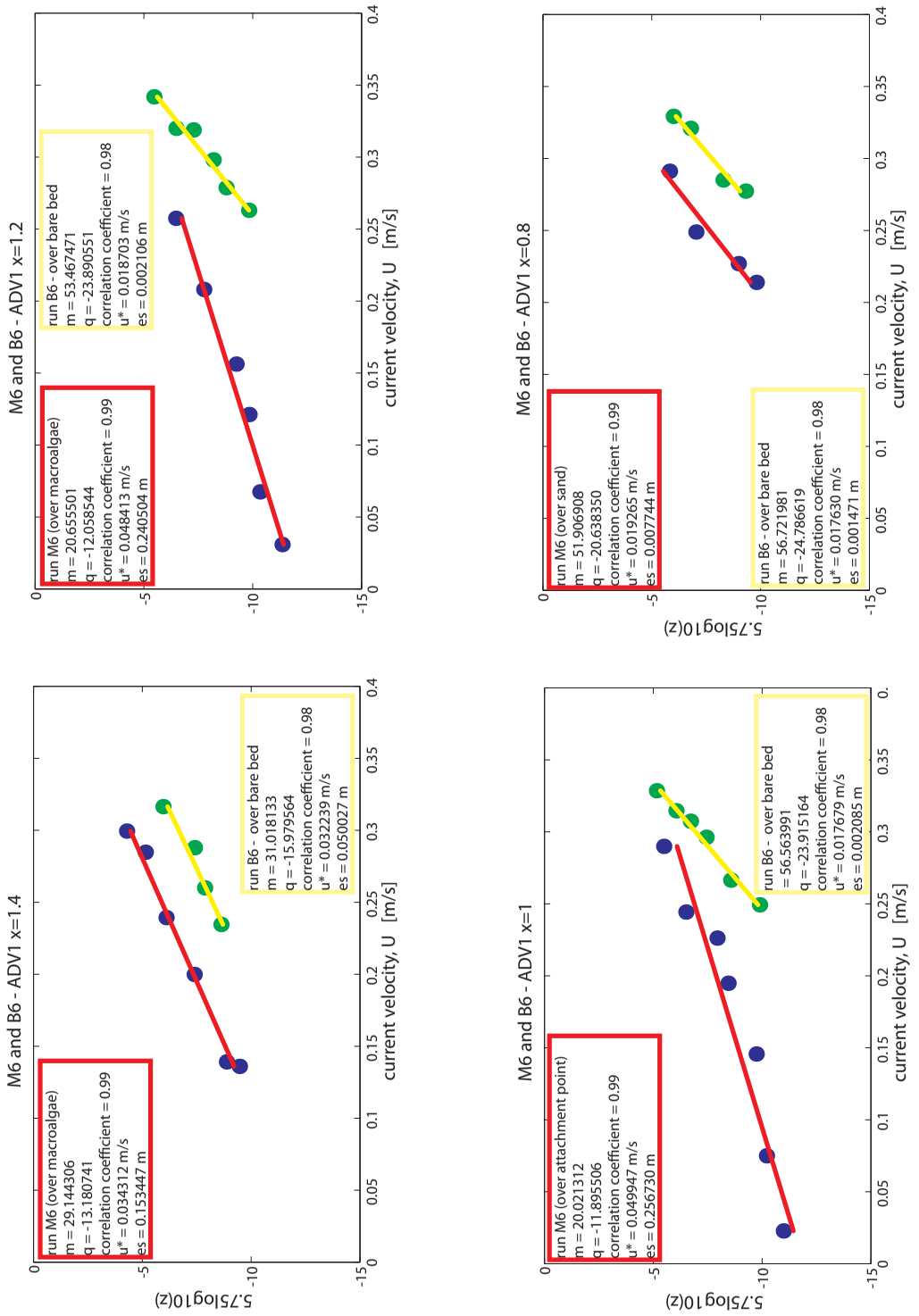

Figure 3.18: Fitting of experimental data using the logarithmic law (Eq. 3.7) and estimate of the friction velocity u_* and of the roughness factor e_s. The hydraulic conditions are those of run 6 and the data refer to ADV1. Plates a), b), c) and d) refer to longitudinal locations denoted as X_1 X_2, X_3 and X_4 in Figure 3.2

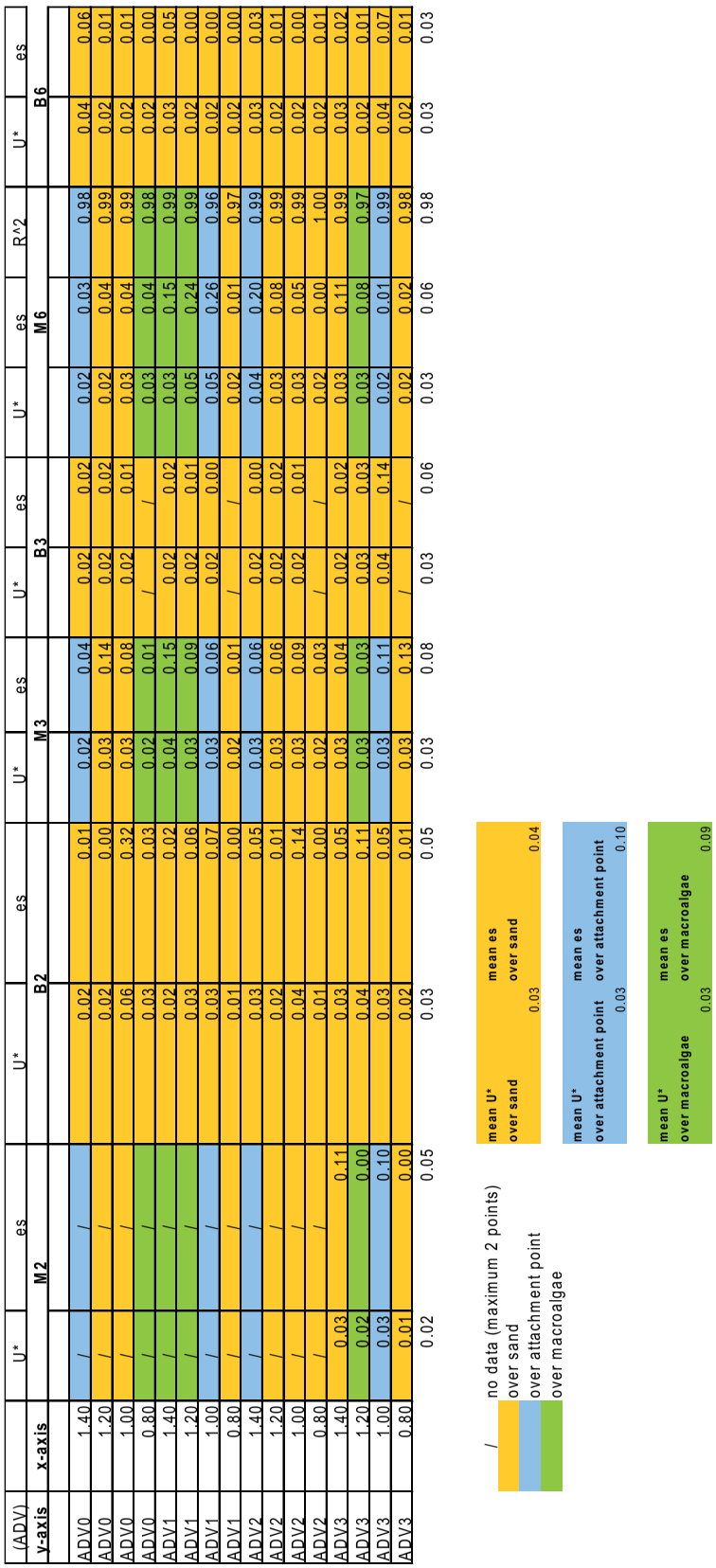

Figure 3.19: Summary of all the Shear Velocity and Nikuradse Roughness values resulting from six runs with just flow hydro condition (M2 and B2, M3 and B3, M6 and B6). At the bottom the averages values of both parameters are reported.

profile would suggest an appreciable increase of roughness and a slightly larger friction velocity. On the other hand, direct observation of the sandy bed indicate that macro-algae inhibit the formation of bedforms, thus implying a reduction of the overall bed friction. On average, runs over macro-algae exhibit, on average, a slightly higher number of bedform crests per unit length and a slightly lower wavelength than runs carried out over bare bed. In particular, smalls bedform (2 centimetres high on average) have been observed to form around the point of attachment of macro-algae strands.

Friction velocity, u^*, is the typical velocity scale adopted for normalizing mean velocity and turbulent quantities (Nezu and Nakagawa, 1993).

Figures 3.20 and 3.21 show the velocity profiles measured in algae covered bed tests (M2, M3 and M6), normalized with the mean flow velocity and those sampled under bare bed conditions in runs B2, B3 and B6, normalized by u^*.

The Reynolds Number, computed on the basis of the Friction velocity, u^*, Nezu and Nakagawa (1993):

$$Re = \frac{u^* \cdot D}{\nu} \tag{3.8}$$

(with D the flow depth, and ν the cinematic viscosity $\approx 1.2710^{-6} m^2/s$) is included in range 4724 - 6834 (see table 3.19) confirming the turbulent nature of the examined flow conditions.

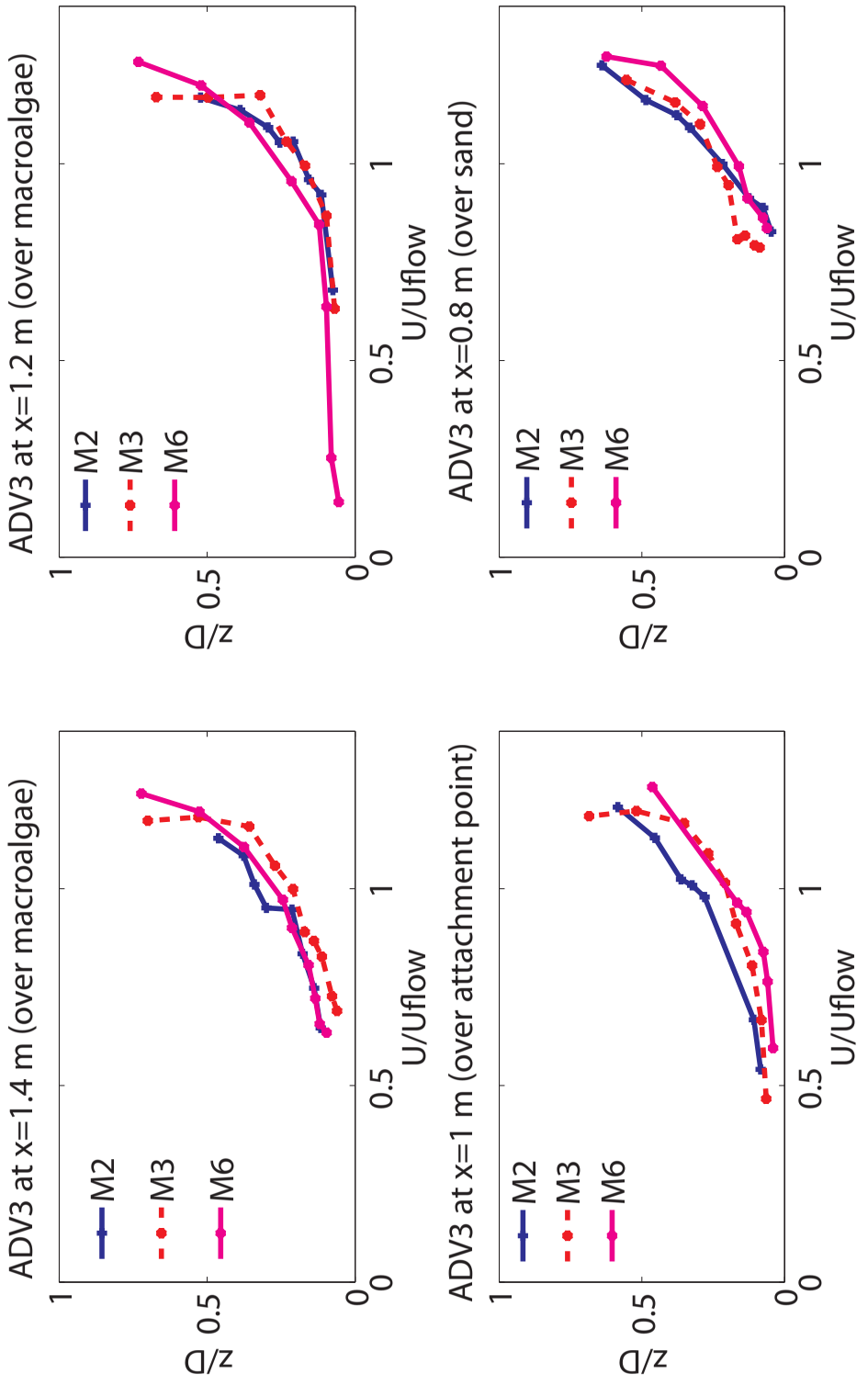

Figure 3.20: Vertical Velocity profile normalized by Friction velocity from ADV3 data for M2, M3 and M6.

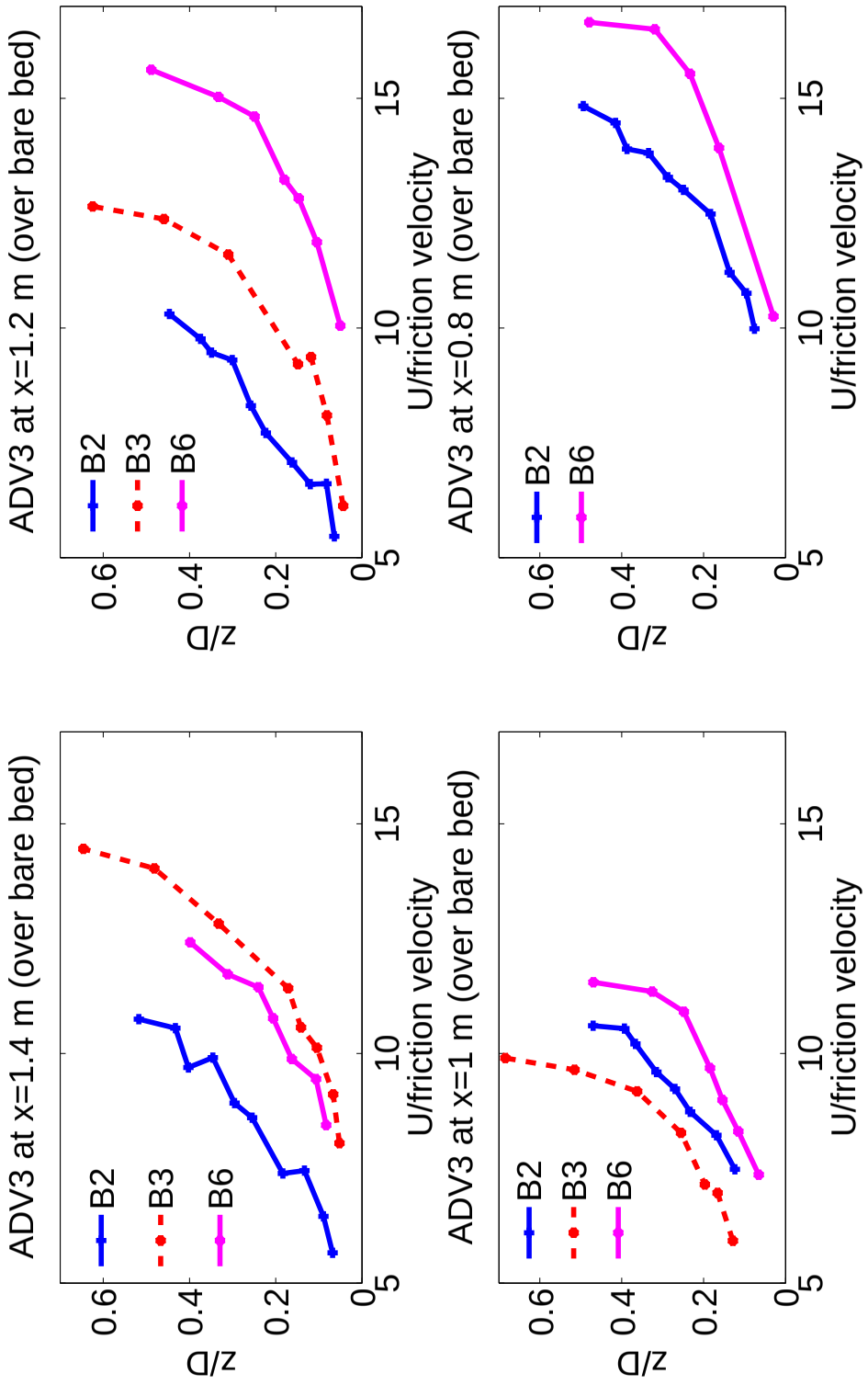

Figure 3.21: Vertical Velocity profile normalized by Friction velocity from ADV3 data for B2, B3 and B6.

Statistical Analysis

The sixteen linear regression lines obtained for the measured velocity profiles have been analyzed from a statistical point of view. We firstly compute the Standard Error for the slopes and for the intercepts emerging from linear regressions, namely:

$$SE_m = \sqrt{\frac{\frac{\sum_n^{i=1}(y_i-\hat{y})^2}{n-2}}{\sum_n^{i=1}(x_i-\overline{x})^2}} \tag{3.9}$$

$$SE_b = \frac{\sum_n^{i=1}(y_i-\hat{y})^2}{n-2}\sqrt{\frac{1}{n}+\frac{\overline{x}^2}{\sum_n^{i=1}(x_i-\overline{x})^2}} \tag{3.10}$$

where: y_i is the independent variable ($5.75log_{10}(z)$); $\hat{y}$ is= $mx+b$; n is the number of values; x_i is the dependent variable (u_x); $\overline{x}$ is the average of u_x.

From the Standard Errors we have determined the 95% confidence intervals (see Eq. 3.11-3.14) for m and b and, hence, for the shear velocity and roughness parameter:

$$LowerBound_m = m - 1.96 \cdot SE_m \tag{3.11}$$

$$UpperBound_m = m + 1.96 \cdot SE_m \tag{3.12}$$

$$LowerBound_b = b - 1.96 \cdot SE_b \tag{3.13}$$

$$UpperBound_b = b + 1.96 \cdot SE_b \tag{3.14}$$

In Fig. 3.22 (a) we report the friction velocity and its confidence range for runs with and without macroalgae (see also the data reported in Table 3.23). The confidence interval has been inferred from the Lower and Upper bounds

computed for the slope parameter $m = 1/u^*$. It clearly appears that the friction velocity is generally attains larger values over macroalgae than over bare bed, even though the differences are very small. Indeed, the value of u_* obtained by averaging all the data corresponding to points over macroalgae is $0.03m/s$, while that referring to points over sand is $0.02m/s$. In Fig. 3.22 (b) we then report the roughness coefficient and its confidence range for runs with and without macroalgae (see also data in Table 3.24). In this case the confidence interval is inferred for friction velocity is inferred from the Lower and Upper bounds values computed for the intercept parameter. The influence of macroalgae is more marked in the case of the roughness parameter. As shown in Figure 3.22 (b) the values of e_s over macroalgae are bigger than those estimated over a bare bed, the average value over macroalgae and bare sand points being $0.09m$ and $0.04m$, respectively.

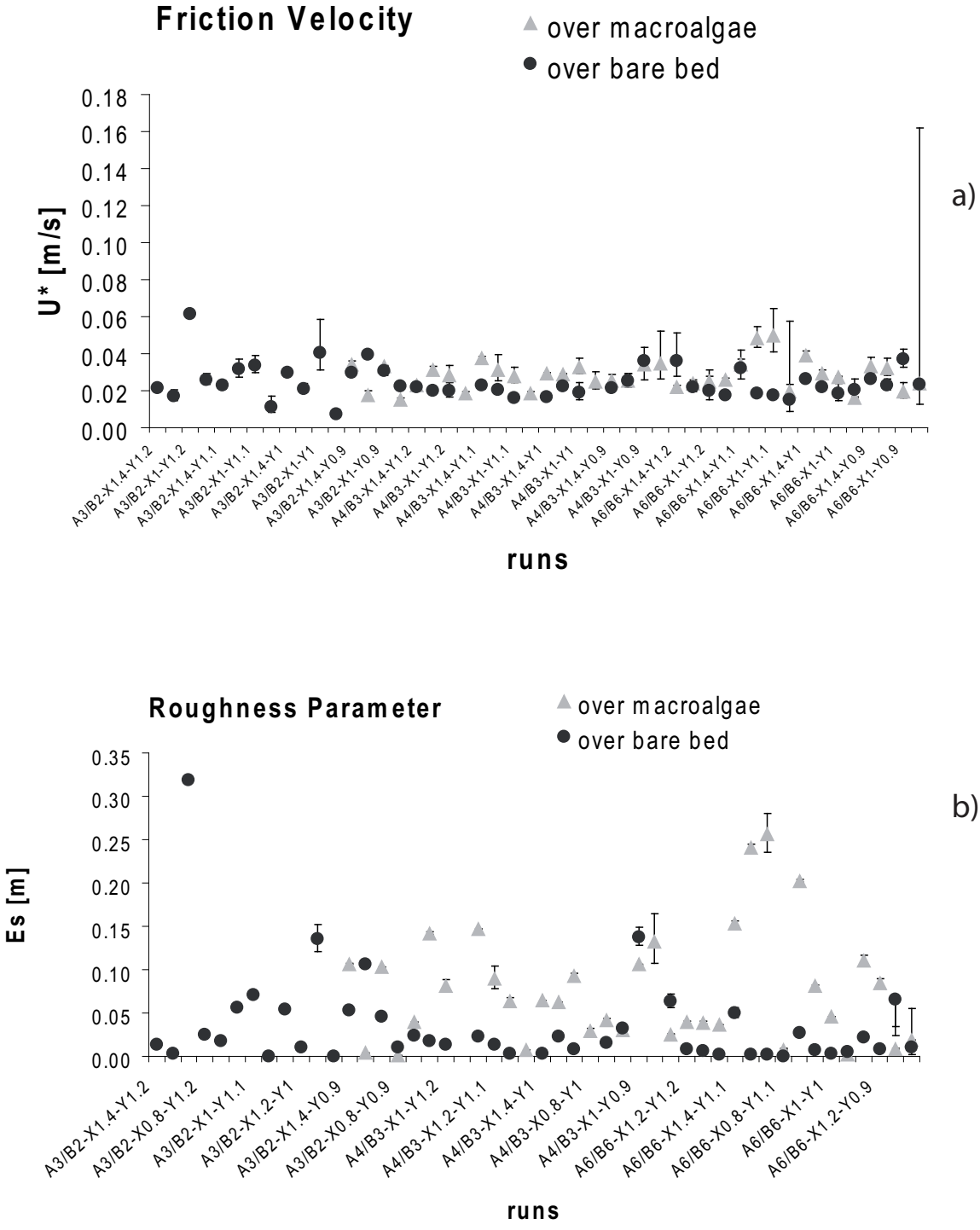

Figure 3.22: a) Friction velocity and its confidence range for runs with and without macroalgae; b) Roughness coefficient and its confidence range for runs with and without macroalgae.

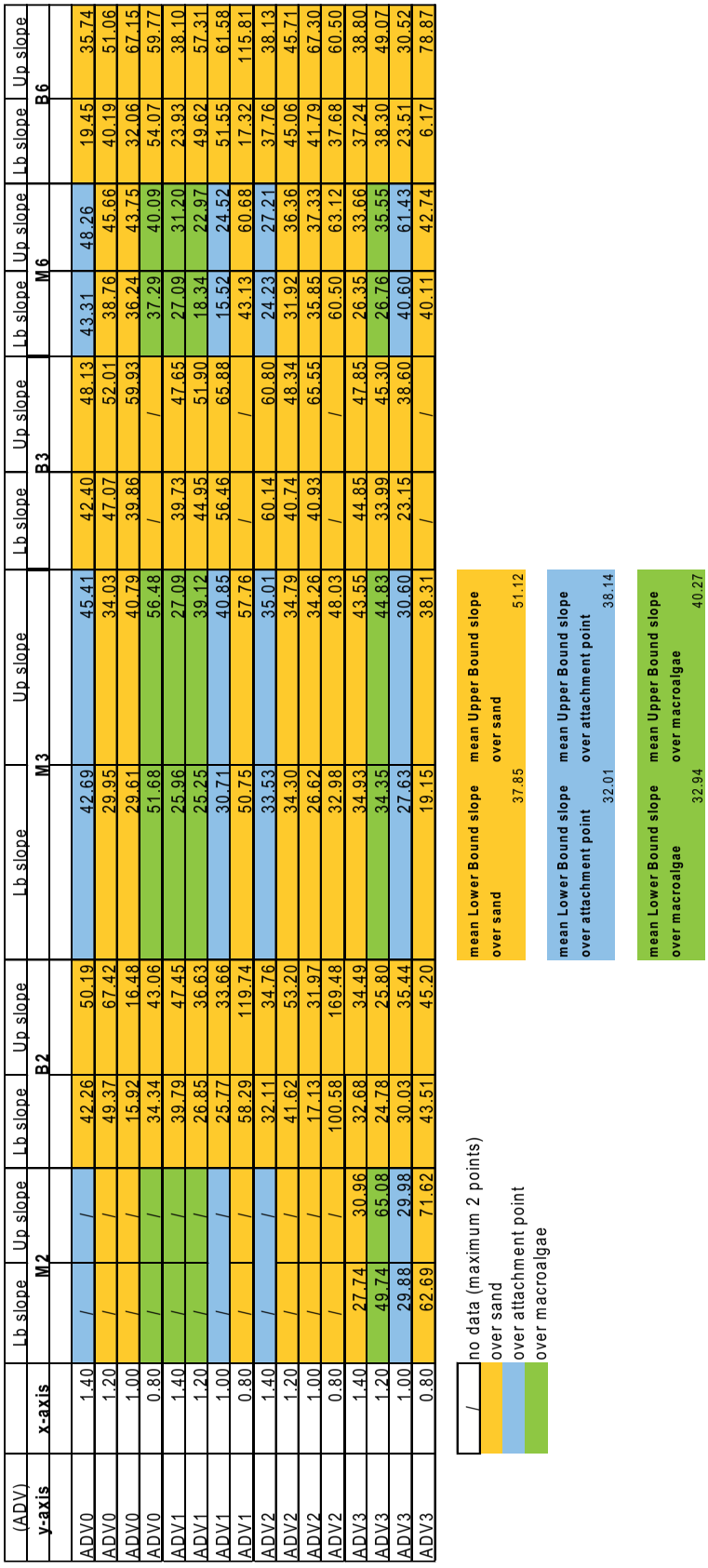

(ADV)		Lb slope	Up slope	Lb slope	Up slope	Lb slope	Up slope	Lb slope	Up slope	Lb slope	Up slope	Lb slope	Up slope
y-axis	x-axis	M2		B2		M3		B3		M6		B6	
ADV0	1.40	/	/	42.26	50.19	42.69	45.41	42.40	48.13	43.31	48.26	19.45	35.74
ADV0	1.20	/	/	49.37	67.42	29.95	34.03	47.07	52.01	38.76	45.66	40.19	51.06
ADV0	1.00	/	/	15.92	16.48	29.61	40.79	39.86	59.93	36.24	43.75	32.06	67.15
ADV0	0.80	/	/	34.34	43.06	51.68	56.48	/	/	37.29	40.09	54.07	59.77
ADV1	1.40	/	/	39.79	47.45	25.96	27.09	39.73	47.65	27.09	31.20	23.93	38.10
ADV1	1.20	/	/	26.85	36.63	25.25	39.12	44.95	51.90	18.34	22.97	49.62	57.31
ADV1	1.00	/	/	25.77	33.66	30.71	40.85	56.46	65.88	15.52	24.52	51.55	61.58
ADV1	0.80	/	/	58.29	119.74	50.75	57.76	/	/	43.13	60.68	17.32	115.81
ADV2	1.40	/	/	32.11	34.76	33.53	35.01	60.14	60.80	24.23	27.21	37.76	38.13
ADV2	1.20	/	/	41.62	53.20	34.30	34.79	40.74	48.34	31.92	36.36	45.06	45.71
ADV2	1.00	/	/	17.13	31.97	26.62	34.26	40.93	65.55	35.85	37.33	41.79	67.30
ADV2	0.80	/	/	100.58	169.48	32.98	48.03	/	/	60.50	63.12	37.68	60.50
ADV3	1.40	27.74	30.96	32.68	34.49	34.93	43.55	44.85	47.85	26.35	33.66	37.24	38.80
ADV3	1.20	49.74	65.08	24.78	25.80	34.35	44.83	33.99	45.30	26.76	35.55	38.30	49.07
ADV3	1.00	29.88	29.98	30.03	35.44	27.63	30.60	23.15	38.60	40.60	61.43	23.51	30.52
ADV3	0.80	62.69	71.62	43.51	45.20	19.15	38.31	/	/	40.11	42.74	6.17	78.87

/ no data (maximum 2 points)
over sand
over attachment point
over macroalgae

mean Lower Bound slope over sand 37.85
mean Upper Bound slope over sand 51.12

mean Lower Bound slope over attachment point 32.01
mean Upper Bound slope over attachment point 38.14

mean Lower Bound slope over macroalgae 32.94
mean Upper Bound slope over macroalgae 40.27

Figure 3.23: Lower and Upper bounds of the slope m computed through Equations 3.9, 3.11, 3.12.

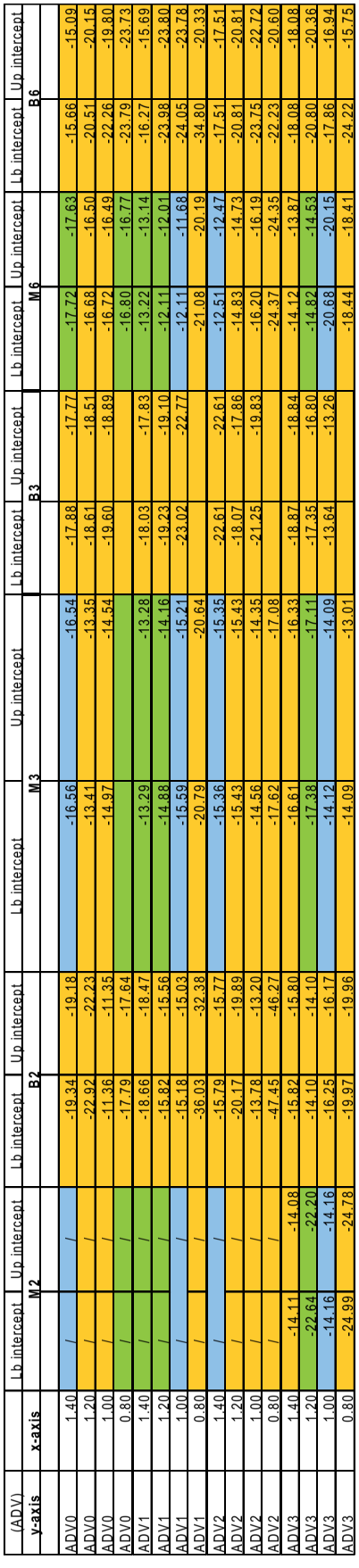

(ADV)		Lb intercept	Up intercept	Lb intercept	Up intercept	Lb intercept	Up intercept	Lb intercept	Up intercept	Lb intercept	Up intercept	Lb intercept	Up intercept
y-axis	x-axis	M2		B2		M3		B3		M6		B6	
ADV0	1.40	/	/	-19.34	-19.18	-16.56	-16.54	-17.88	-17.77	-17.72	-17.63	-15.66	-15.09
ADV0	1.20	/	/	-22.92	-22.23	-13.41	-13.35	-18.61	-18.51	-16.68	-16.50	-20.51	-20.15
ADV0	1.00	/	/	-11.36	-11.35	-14.97	-14.54	-19.60	-18.89	-16.72	-16.49	-22.26	-19.80
ADV0	0.80	/	/	-17.79	-17.64					-16.80	-16.77	-23.79	-23.73
ADV1	1.40	/	/	-18.66	-18.47	-13.29	-13.28	-18.03	-17.83	-13.22	-13.14	-16.27	-15.69
ADV1	1.20	/	/	-15.82	-15.56	-14.88	-14.16	-19.23	-19.10	-12.11	-12.01	-23.98	-23.80
ADV1	1.00	/	/	-15.18	-15.03	-15.59	-15.21	-23.02	-22.77	-12.11	-11.68	-24.05	-23.78
ADV1	0.80	/	/	-36.03	-32.38	-20.79	-20.64			-21.08	-20.19	-34.80	-20.33
ADV2	1.40	/	/	-15.79	-15.77	-15.36	-15.35	-22.61	-22.61	-12.51	-12.47	-17.51	-17.51
ADV2	1.20	/	/	-20.17	-19.89	-15.43	-15.43	-18.07	-17.86	-14.83	-14.73	-20.81	-20.81
ADV2	1.00	/	/	-13.78	-13.20	-14.56	-14.35	-21.25	-19.83	-16.20	-16.19	-23.75	-22.72
ADV2	0.80	/	/	-47.45	-46.27	-17.62	-17.08			-24.37	-24.35	-22.23	-20.60
ADV3	1.40	-14.11	-14.08	-15.82	-15.80	-16.61	-16.33	-18.87	-18.84	-14.12	-13.87	-18.08	-18.08
ADV3	1.20	-22.64	-22.20	-14.10	-14.10	-17.38	-17.11	-17.35	-16.80	-14.82	-14.53	-20.80	-20.36
ADV3	1.00	-14.16	-14.16	-16.25	-16.17	-14.12	-14.09	-13.64	-13.26	-20.68	-20.15	-17.86	-16.94
ADV3	0.80	-24.99	-24.78	-19.97	-19.96	-14.09	-13.01			-18.44	-18.41	-24.22	-15.75

Figure 3.24: Lower and Upper bounds the roughness coefficient computed through Equations 3.10, 3.13, 3.12.

Vertical Distribution of Shear Stresses

The vertical distributions of turbulent Reynolds stresses, $\tau_t = -\rho\overline{u_x' u_z'}$, and mean viscous stresses, $\tau_v = \mu\partial\overline{u}_x/\partial z$ have also been analyzed.

$$\tau = \tau_t + \tau_\mu = -\rho_w\overline{u_x' u_z'} + \mu\frac{\partial\overline{u_x}}{\partial z} \tag{3.15}$$

where ρ_w is the water density (assumed equal to $1027kg/m^3$ for salt water adopted for runs with macroalgae and equal to $999kg/m^3$ for fresh water for runs carried out without macroalgae); $u_x^{'}$, $u_z^{'}$ are the fluctuating velocity respectively along the longitudinal and the vertical direction; and μ is the dynamic viscosity ($1.310^{-3}kg/ms$).

Figures 3.25 and 3.26 report the vertical profiles of τ_t, τ_v and $\tau = \tau_v + \tau_t$ calculated for either a macroalgae covered bed (run M3) and a bare sandy bed (run B3).

It immediately appears that in any case, as expected, the contribution of the viscous shear stresses are much smaller than that provided by turbulent shear stresses, except near the bed. However, the presence of macroalgae strongly affects the vertical distribution of shear stresses, which increases from the bottom until approximately the height of the macroalgae layer, where it starts to decrease almost linearly until the water level (Figure 3.25). In the case of bare sandy bed, on the other hand, the vertical distribution of shear stresses strongly depends on the location with respect to bedforms. As observed by Dimas *et al.* (2008) and Blom and Booij (1995) in flume experiments with dune covered beds, the shear stresses distribution over a vertical located upstream of a bedform is always decreasing linearly from the bottom to the surface, like in the case of Figure 3.26. Conversely, if the vertical is located downstream of the bedform crest, the shear stress initially increases until it reaches a maximum value and subsequently decreases to attain a vanishing value at the water surface as ob-

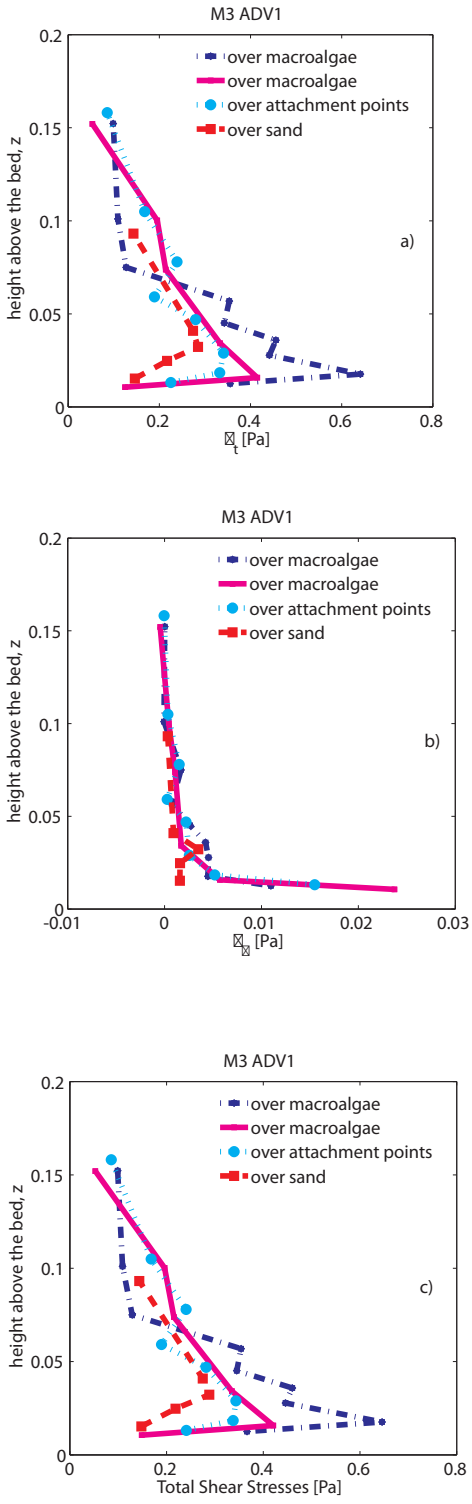

Figure 3.25: Vertical profiles of: a) turbulent Reynolds stresses, τ_t; b) viscous shear stresses, τ_v; c) total shear stresses, $\tau = \tau_v + \tau_t$, estimated on the basis of ADV1 measurements in run M3, carried out over a macroalgae covered bed.

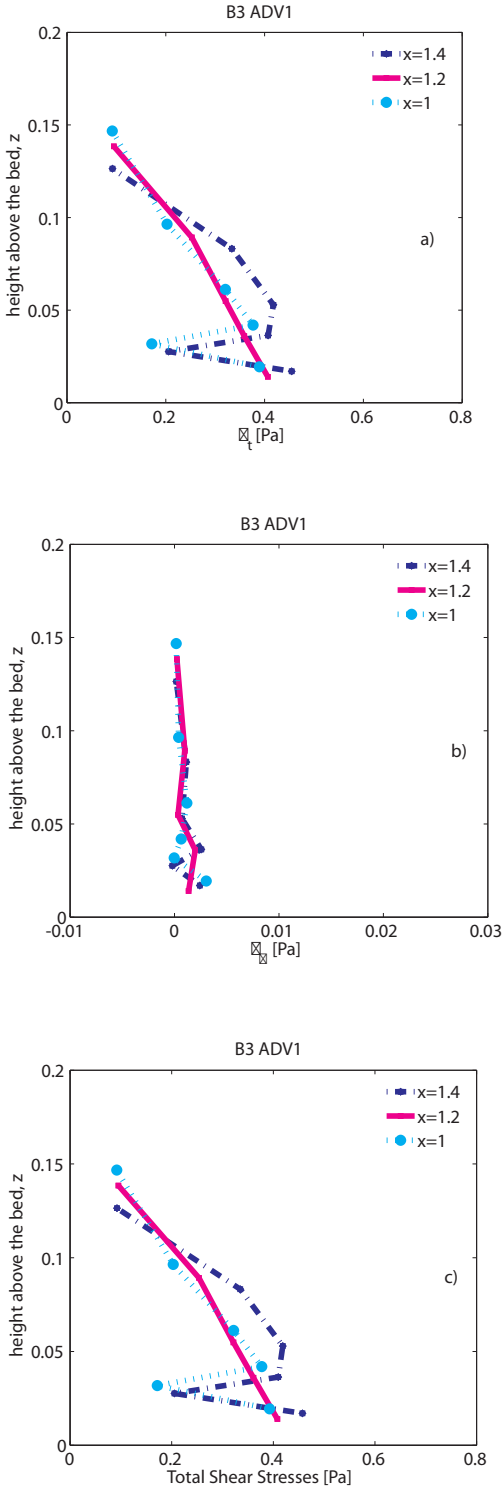

Figure 3.26: Vertical profiles of: a) turbulent Reynolds stresses, τ_t; b) viscous shear stresses, τ_v; c) total shear stresses, $\tau = \tau_v + \tau_t$, estimated on the basis of ADV1 measurements in run B3, carried out over a bare bed. In figure x=1.4, x=1.2 m correspond to macroalgae positions, while x=1 m refers to a macroalgae attachment point.

served along some verticals of Figure 3.26. This latter trend is quite similar to that characterizing nearly all the macroalgae covered bed profiles of Figure 3.25.

Double Averaging

In order to obtain a macroscopical description of the flow features within the study area, a double-averaging analysis has been carried out averaging over turbulence and over investigated area the longitudinal velocity. The logarithmic law and the Reynolds Stresses profiles have been also averaged in planes parallel to the bed. Equations 3.7 and 3.15 become:

$$5.75 \cdot log_{10}(z) = \frac{1}{u^*} < \overline{u_x} > +5.75 log_{10}(e_s) - 8.5 \tag{3.16}$$

$$\tau = -\rho_w < \overline{u_x' u_z'} > +\mu \frac{\partial < \overline{u_x} >}{\partial z} \tag{3.17}$$

where $< \overline{u_x} >$ is the time and spatial averaged longitudinal velocity (<> denoting spatial average, while the overbar indicates turbulence average).

Results of double-averaging process are reported in figure 3.27.

This analysis confirms that the presence of *Ulva intestinalis* leads to velocity profiles that are much less steep near the bed, where the flow velocity is decreased, while the bottom friction increases. In particular the presence of vegetation causes a decrease of both the velocity and the related fluctuations near the bed which, in turn, determines a lower bed shear stress and, hence, and enhanced sediment stability.

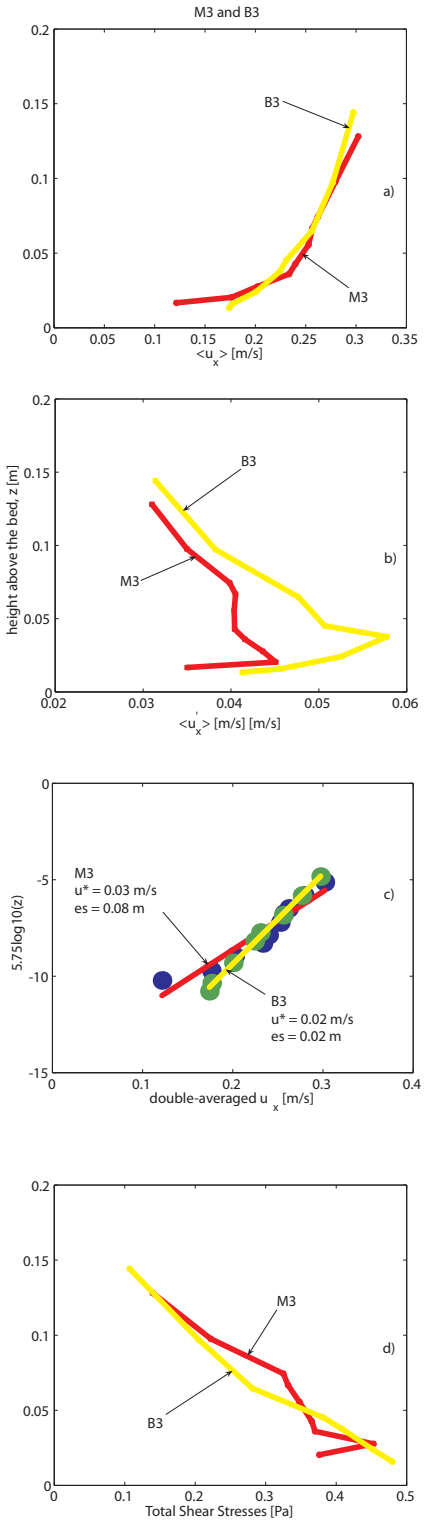

Figure 3.27: Average over planes parallel to the bed of:(a) the instantaneous mean longitudinal velocity, u_x; (b) the fluctuating velocity, $u_x^{'}$. Double-averaging of:(c) the logarithmic law and (d) the Reynolds Stresses. Spatial average over planes parallel to the bed is denoted by $< \cdots >$, while an overline indicates time average.

3.3.7 Spectral Analysis

In order to study the content of the signal given by the time series of the fluctuating component of the longitudinal velocity, $u_x^{'}$, we compute the mono-dimensional Energy Spectrum through Fast Fourier Transform (FFT) Analysis. Firstly, the autocorrelation of $u_x^{'}$ is computed, then the FFT of the autocorrelation function is performed. Finally the Energy Density, $E[L^3/T^2]$, reads:

$$E(f) = C\epsilon^{2/3} f^{-5/3} \tag{3.18}$$

where C is Kolmogorov universal constant, approximately equal to 0.5; ϵ is the turbulent dissipation rate, a quantity characterizes the turbulence features, and $f[1/T]$ is the Frequency. The Energy density E is plotted versus frequency in a log-log plot (small circles in Figures 3.28 and 3.29, respectively for M3 run and B3 run). The Energy trend is mainly characterized by the presence of small eddies corresponding to the highest frequencies. In order to better visualize the monotonically decreasing trend of the Energy Density a binning analysis on a logarithmic scale is performed. The frequency values in the inertial subrange (corresponding to the middle interval of the curve, approximately between $f = 10^{-1}$ and $f = 1$) have been partitioned in several intervals and the mean value of the energy density in each bin is computed (blue circles). After linear fitting the mean value of the energy *vs* frequency in the range where the binning analysis has been performed, the slope of the lines, respectively equal to -1.2 and -1.3, are computed. The slope that we obtained is close to the Kolmogorov'law, which states that the slope in the inertial subrange should be equal to -5./3.

It is interesting to observe that the slope for the run over bare bed is slightly higher than the slope for the run with macroalgae, denoting that macroalgae act interfering the turbulence structure of the energy field.

Similar spectral characteristic were observed by Christiansen *et al.* (1999)

and Leonard and Luther (1995), who found out that the reduction in energy at low frequencies is due to the vegetation, which inhibits production of larger turbulent eddies, the vegetation also contributed to the break down of larger eddies into smaller ones.

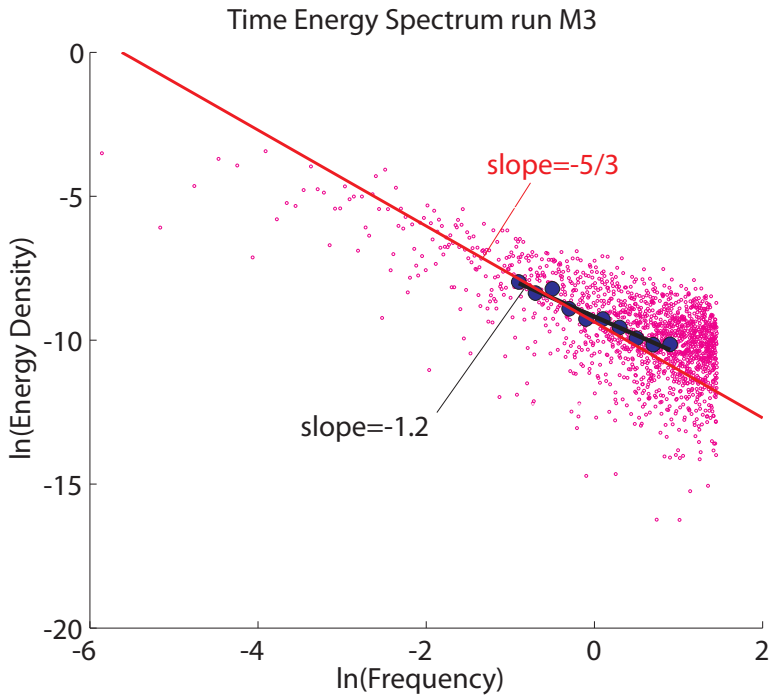

Figure 3.28: Time Spectrum for run M3 (conducted under uniform flow conditions for a macroalgae covered bed). The small circles represent the scatter plot of the Energy versus Frequency. In the middle interval of the curve, the inertial subrange, the mean values of the Energy have been computed (blue circles). The slope of the fitting line resulting from linear interpolation of the binnings is -1.2.

On the basis of Taylor's hypothesis the spatial spectrum, $S(k_w)$ is also computed (Nezu and Nakagawa (1993)):

$$S(k_w) = \frac{\overline{u_x}}{2\pi} E(f) \tag{3.19}$$

where k_w is the wave number in the streamwise direction:

$$k_w = \frac{2\pi f}{\overline{u_x}} \tag{3.20}$$

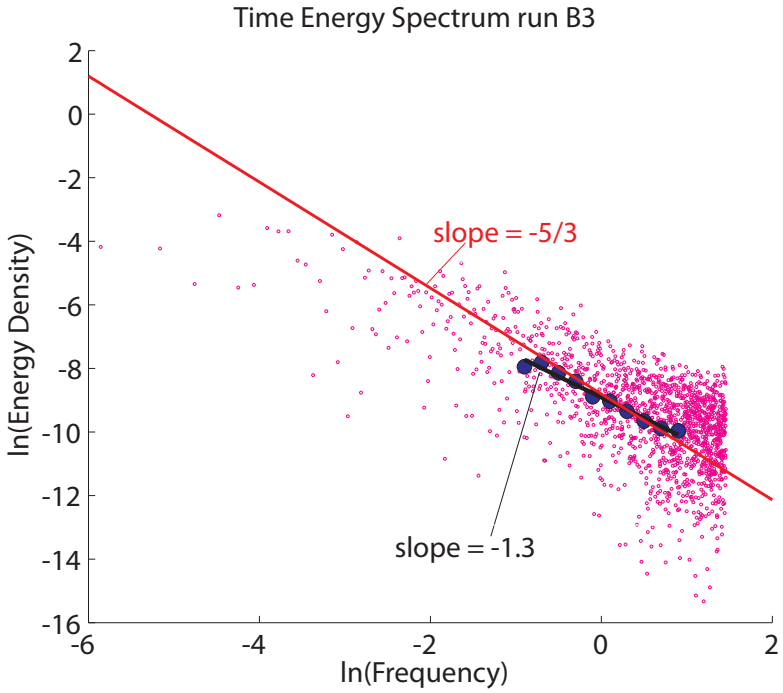

Figure 3.29: Time Spectrum for run B3 (conducted under uniform flow conditions for a bare sandy bed). The small circles represent the scatter plot of the Energy versus Frequency. In the middle interval of the curve, the inertial subrange, the mean values of the Energy have been computed (blue circles). The slope of the fitting line resulting from linear interpolation of the binnings is -1.3

As far the Time Energy Spectrum case, we report the monodimensional energy spectrum for the space scale in figures 3.30 3.31, where the binning analysis is here performed in the interval of wave number $k = 10^1$ and $k = 10^2$. The slope that we obtained are still close the $-5/3$ law of Kolomogorov. B3 is reaching the -1.66 value much closer. Again the slope for the run over bare bed is slightly higher than the slope for the run with macroalgae, confirming that macroalgae generate perturbation which are perceptible in the energy spectra.

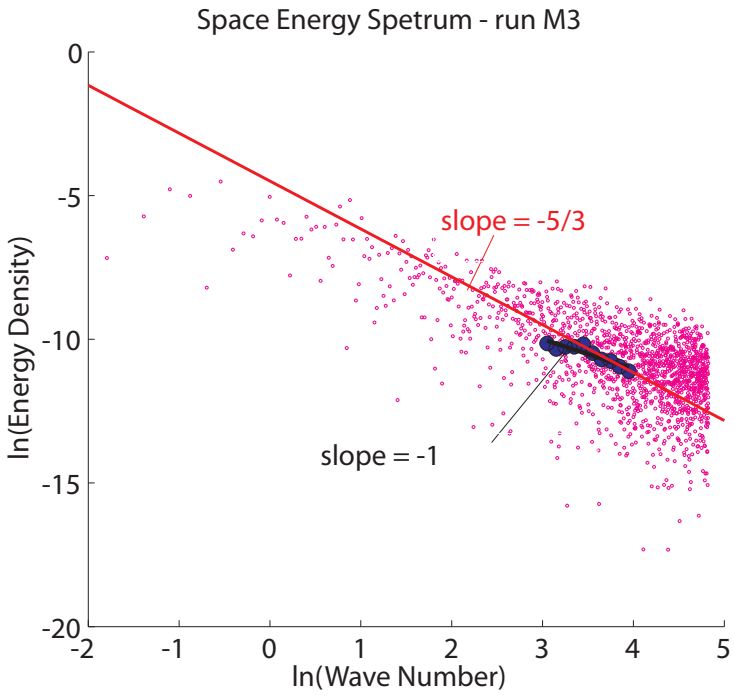

Figure 3.30: Space Spectrum for run M3 (conducted under uniform flow conditions for a macroalgae covered bed). The small circles represent the scatter of the Energy versus Wave Number. In the middle interval of the curve, the inertial subrange, the mean values of the Energy have been computed (black circles). The slope of the fitting line resulting from linear interpolation of the binnings is -1.

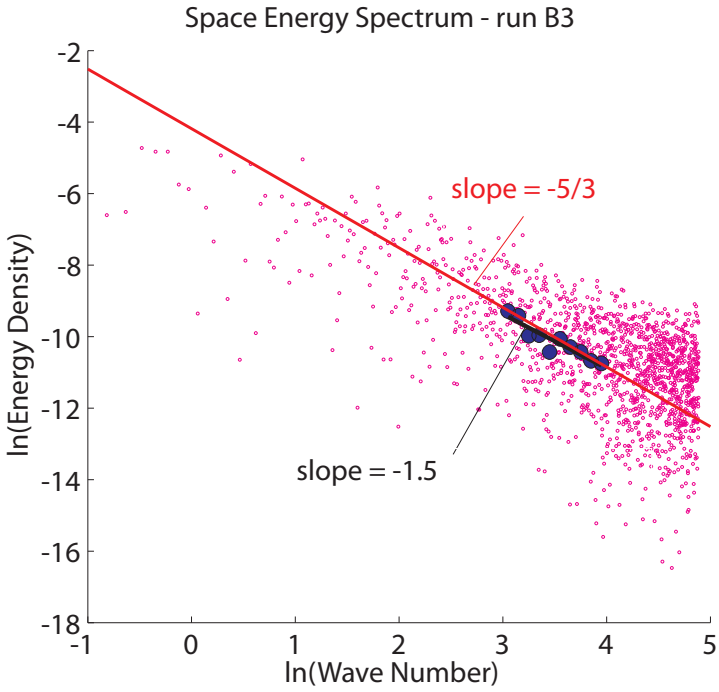

Figure 3.31: Time Spectrum for run B3 (conducted under uniform flow conditions for a bare sandy bed). The small circles represent the scatter of the Energy versus Wave Number. In the middle interval of the curve, the inertial subrange, the mean values of the Energy have been computed (black circles). The slope of the fitting line resulting from linear interpolation of the binnings is -1.5.

3.4 Discussion

We have provided a overall view of how *Ulva Intestinalis* affects the unidirectional flow and waves superposed to a uniform flow over a sandy bed. The data collected under a range of flow depths suggest that macro-algae exert a significant bio-stabilizing effect. As documented by direct observations and bed elevation measurements, and unlikely the great majority of vegetation so far used in laboratory flumes, this species of macro-algae tend to lay flat over the bed, waving horizontally with the current. The interaction of macro-algae with the flow results in a decreasing of bedform wavelength, with small bedforms forming around the macro-algae strands. The vertical distributions of the longitudinal velocity and of shear stress, suggest that macro-algae lead to a decrease of the mean flow velocity and an increase of the flow resistance close to the bed. The friction velocity is in fact generally bigger over macro-algae than over bare bed. The presence of macro-algae also contribute to inhibit the overall mobility of sediments, thus reducing the amount of sediment transported as bedload.

The present study focused on macro-algae mats of current driven flows. Nevertheless, both temporal and spatial flow dynamics are key to fully understanding the momentum transfer mechanisms and their influence on flow resistance (Nikora *et al.*, 2001),(Nikora *et al.*, 2004). A systematic study is then needed to asses the influence of macroalgal mats on sediment transport in wave-current flows under a wide range of flow depth surrogating the different flow depth induced by tidal oscillations.

Chapter 4

Conclusions and future research

The main conclusions for the two main chapters of this thesis are here report and future research directions are presented.

The first part of this thesis concerns the sediment property evaluations by means of a point wave-tidal model and a suspended sediment model on the basis of wind and turbidity observations acquired in the Venice Lagoon. The estimates of bed sediment properties based on observations of water depth, SSC and wind velocity in the Venice lagoon give a settling velocity in the range $2.7 \cdot 10^{-4} - 6.3 \cdot 10^{-4} m/s$ and a residual concentration which is supposed to never settle in the lagoonal ecosystem in the range $6.7 - 16.2 mg/l$. These estimates correspond to deduced values for the critical shear stresses for erosion in the range $0.1 - 0.5 Pa$ and for the erosion parameter in the range $2 \cdot 10^{-6} - 3.1 \cdot 10^{-4} kg/ms^2$. Results are in line with what is expected for sandy-silt sediment and are consistent with independent *in situ* estimates. The method developed here appears to have distinct advantages over more traditional in situ procedures (e.g. the Sea Carousel or the Cohesive Strength Meter) because it does not interfere with the surface biofilm and provides a direct and quantitative physical estimate of the critical-shear stress. The method proposed is thus effective in studying and monitoring bed sediment properties on larger spatial scales and on longer temporal scales than those afforded by *in situ* observations.

The second part of this thesis concerns the quantification of the impact of

macroalgae on sediment stability and flow dynamic, by means of an experimental activity carried out at the Total Environment Simulator facility provided by the University of Hull, UK, within the European Project Hydralab III. This work gives relevant contributions on the mechanical behavior of *Enteromorpha* in open-channel flume under unidirectional flow conditions and waves superposed to a uniform flow, suggesting that macroalgae exert a significant bio-stabilizing effect. We observed that macroalgae act decreasing the mean flow velocity, increasing the flow resistance close to the bed. As documented by direct observations and bed elevation measurements, and unlikely the great majority of vegetation so far used in laboratory flumes, this species of macro-algae tend to lay flat over the bed, waving horizontally with the current. The interaction of macro-algae with the flow results in a decreasing of bedform wavelength, with small bedforms forming around the macro-algae strands. The vertical distributions of the longitudinal velocity and of shear stress, suggest that macro-algae lead to a decrease of the mean flow velocity and an increase of the flow resistance close to the bed. The friction velocity is in fact generally bigger over macro-algae than over bare bed. The presence of macro-algae also contribute to inhibit the overall mobility of sediments, thus reducing the amount of sediment transported as bedload. The present study focused on macro-algae mats of current driven flows. Nevertheless, both temporal and spatial flow dynamics are key to fully understanding the momentum transfer mechanisms and their influence on flow resistance (Nikora *et al.*, 2001),(Nikora *et al.*, 2004). A systematic study is then needed to asses the influence of macroalgal mats on sediment transport in wave-current flows under a wide range of flow depth surrogating the different flow depth induced by tidal oscillations.

Acknowledgments

My acknowledgements to the Ministero delle Infrastrutture e dei Trasporti-Magistrato alle Acque di Venezia - tramite il suo concessionario Consorzio Venezia Nuova for providing wind, turbidity data and to the Center for Forecast of Tide Level and High Water in Venice for providing water level data.

I also thank the European Community's Sixth Framework Programme through the grant to the budget of the Integrated Infrastructure Initiative HYDRALAB III within the Transnational Access Activities for financing the experiment activity at the Total Environment Simulator of the University of Hull, UK.

I am very grateful to all who helped me in carrying out this work.

I thank Professor Andrea Rinaldo and Professor Marco Marani for giving me the great opportunity to take part in their research group. I particularly thank Professor Marco Marani for supporting me and advising me in executing the analysis on sediment bed properties in this research work. I am grateful to Professor Stefano Lanzoni for giving me the chance to participate to the HYDRALAB III European project and for leading me in carrying out the analyses on the interaction between macroalgae and sediment/flow dynamic.

My great thanks to Dr. Andrea D'Alpaos for following me during the first part of this work and also for his patience in helping me to prepare for the admission exam of this PhD school. Thanks to Dr. Luca Carniello for his helpfulness in working together during the realization of this research work. Thanks to Gianluigi Bugno for helping me in the preparation of the experimental flume plan.

My great thank to the HYDRALAB III working group, in particular Pro-

fessor José Figueiredo da Silva, Professor Robert Duck, Dr. Stuart McLelland, and Dr. Brendan Murphy for imparting their knowledge and for the nice time spent together working in the lab and outside the lab!

Last but not least, my infinite thanks to all my special colleagues for their very useful advices and for supporting me in this work.

Bibliography

Allen, J. R. L. (2000). Morphodynamics of holocene saltmarshes: a review sketch from atlantic and southern north sea coast of europe. *Quaternary Science Reviews, (19), pp. 1155–1231.*

Amos, C., Bergamasco, A., Umgiesser, G., Cappucci, S., Cloutier, D., DeNat, L., Flindt, M., Bonardi, M., and Cristante, S. (2004). The stability of tidal flats in venice lagoon-the results of in-situ measurements using two benthic, annular flumes. *Journal of Mar. Sys., (51), pp. 211–241. doi:10.1016/j.jmarsys.2004.05.013.*

Amos, C. L., Umgiesser, G., Ferrarin, C., Thompson, C. E. L., Whitehouse, R. J. S., Sutherland, T. F., and Bergamasco, A. (2010). The erosion rate of cohesive sediments in venice lagoon, Italy. *Continental Shelf Research, 30 (8), pp. 859-870, doi:10.1016/j.csr.2009.12.001.*

Barnett, T. (1968). On the generation, dissipation, prediction of ocean wind waves. *J. Geophys. Res., (73), pp. 513-529.*

Battjes, J. A. and Janssen, J. (1978). Energy loss and setup due to breaking of random waves. *Proceedings of 16th International Conference on Coastal Engineering, pp. 569-587.*

Blom, P. and Booij, R. (1995). Turbulent free-surface flow over a sill. *Journal of Hydraulic Research, 33 (5), pp. 663-682.*

Bolam, S. G., Fernandes, T. F., Read, P., and Raffaelli, D. (2000). Effects

of macroalgal mats on intertidal sandflats: an experimental study. *J. Expt. Marine Biol. and Ecol., 249, pp. 123-137.*

Breugem, W. A. and Holthuijsen, L. H. (2007). Generalized shallow water wave growth from lake george. *Journal of Waterway, Port, Coastal, and Ocean Engineerign, ASCEE, 173, pp. 25-43.*

Carniello, L., Defina, A., Fagherazzi, S., and D'Alpaos, L. (2005). A combined wind wave-tidal model for the Venice Lagoon. *J. Geophys. Res., 110, F04007, doi:10.1029/2004JF000232.*

Carniello, L., D'Alpaos, A., and Defina, A. (2009). Simulation of wind waves in shallow microtidal basins: Application to the venice lagoon, italy. *River, Coastal and Estuarine Morphodynamics: RCEM 2009, Vionnet et al. (eds), 2010 Taylor and Francis Group, London, ISBN 978-0-415-55426-8, pp. 907–912.*

Cavaleri, L. and Malanotte-Rizzoli, P. (1981). Wind wave prediction in shallow water: Theory and applications. *Journal of Geophysical Research,86, C11, pp. 10,961-10, 973, doi:10.1029/JC086iC11p10961.*

Chapman, V. J. (1977). Introduction. *Wet Coastal Ecosystems, pp. 1-30.*

Christiansen, T., Wiberg, P. L., and Milligan, T. (1999). Flow and sediment transport on a tidal salt marsh surface. *Estuarine, Coastal and Shelf Science, 50, pp. 315-331.*

Collins, J. I. (1972). Prediction of shallow water spectra. *Journal of Geophysical Research, 77, pp. 2693-2707.*

CVN (30/06/2004). Attività per la taratura e la validazione del modello idrodinamico e morfologico della laguna di venezia - stazioni fisse. *Consorzio Venezia Nuova, Rapporto Tecnico Finale, Perizia di Variante.*

Defina, A., Carniello, L., Fagherazzi, S., and D'Alpaos, L. (2007). Self organization of shallow basins in tidal flats and salt marshes. *J. Geophys. Res., 112, F03001, doi:10.1029/2006JF000550.*

Dimas, A., Fourniotis, N. T., Vouros, A., and Demetracopoulos, A. (2008). Effect of bed dunes on spatial development of open-channel flow. *Journal of Hydraulic Research, 46 (6), pp. 802-813.*

Dyer, K. R., Christe, M. C., and Wright, E. W. (2000). The classification of mudflats. *Cont. Shelf Res., 20, pp. 1061-1078.*

Einstein, H. A. and Krone, R. B. (1962). Experiments to determine modes of cohesive sediment transport in salt water. *Journal of Geophysical Research, (67), pp. 1451-1461.*

Eriksson, B. K. and Johansson, G. (2005). Effects of sedimentation on macroalgae: Species-specific responses are related to reproductive traits. *Oecologia, 143, pp. 438-448.*

Escartin, J. and Aubrey, D. G. (1995). Flow structure and dispersion within algal mats. *Estuarine, Coastal and Shelf Science, 40, pp. 451-472.*

Fagherazzi, S., Wiberg, P., and Howard, A. (2003). Tidal flow field in a small basin. *Journal of Geophysical Research, 108 (C3), 3071 doi:10.1029/2002JC001340.*

Fagherazzi, S., Carniello, L., D'Alpaos, L., and Defina, A. (2006). Critical bifurcation of shallow microtidal landforms in tidal flats and salt marshes. *PNAS, 103 (22), doi:10.1073/pnas.0508379103, pp. 8337-8341.*

Frostick, L. E. and McCave, I. N. (1979). Seasonal shifts of sediment within an estuary mediated by algal growth. *Estuarine, Coastal and Shelf Science, 9, pp. 569-576.*

Gedan, K. B., Silliman, B. R., and Bertness, M. D. (2009). Centuries of human driven change in salt marsh ecosystem. *Annual Review Marine Sciences, pp. 117-141.*

Gelci, R., Cazalé, H., and Vassal, J. (1957). Prévision de la houle. la methode de densités spectroangulaieres. *Bul. Inform. Comité Central Oceanogr.d'Edude Cotes, 9, pp. 416.*

Hasselmann, K. (1974). On the spectral dissipation of ocean waves due to white-capping. *Boundary Layer Meteorol., 6, pp. 107-127.*

Hinze, J. O. (1959). *Turbulence, an introduction to its mechanism and theory.* pp. 586, McGraw-Hill Book Company, INC.

Houwing, E. J. (1999). Determination of the critical erosion threshold of cohesive sediments on intertidal mudflats along the dutch wadden sea coast.y. *Estuarine, Coastal and Shelf Science, 49, pp. 545-555.*

Kineke, G. C. and Sternberg, R. W. (1989). The effect of particle settling velocity on computed suspended sediment concentration profiles. *Marine Geology, 90, pp. 159-174.*

Kirwan, M. L. and Murray, A. B. (2007). A coupled geomorphic and ecological model of tidal marsh evolution. *Proc. Natl. Acad. Sci. U. S. A., 104, pp. 6118-6122.*

Krone, R. (1987). A method for simulating historic marsh elevations. *Coastal Sediments '87 - American Society of Civil Engineers, New York, pp. 316–323.*

Lagarias, J., Reeds, J. A., Wright, M. H., and Wright, P. E. (1998). Convergence properties of the nelder-mead simplex method in low dimensions. *SIAM Journal of Optimization, 9 1, pp. 112-147.*

Leonard, L. and Luther, M. (1995). Flow hydrodynamics in tidal marsh canopies. *Limnology and Oceanography, 40, pp.1474-1484.*

Longuet-Higgins, M. S. and Stewart, R. W. (1962). Radiation stress and mass transport in gravity waves, with application to surf beats. *Journal of Fluid Mechanics, 13, 4, pp. 481-504, doi:10.1017/S0022112062000877.*

Lopez, F. and Garcia, M. (1998). Open-channel flow through simulated vegetation: Suspended sediment transport modeling. *Water Resources Research, 34, 9, pp.2341-2352.*

Marani, M., Belluco, E., Ferrari, S., Silvestri, S., D'Alpaos, A., Lanzoni, S., Feola, A., and Rinaldo, A. (2006). Analysis, synthesis and modelling of high resolution observations of salt marsh ecogeomorphological patterns in the venice lagoon. *Estuarine Coastal and Shelf Sciences, 69, pp.414-426, doi:10.1016/j.ecss.2006.05.021.*

Marani, M., D'Alpaos, A., Lanzoni, S., Carniello, L., and Rinaldo, A. (2007). Biologically-controlled multipla equilibria of tidal landforms and the fate of the venice lagoon. *Geophys. Res. Lett., 34, L11402, doi:10.1029/2007GL030178.*

Mehta, A. (1984). Characterization of cohesive sediment properties and transport processes in estuaries. *Lecture Notes in Coastal and Estuarine Studies-Estuarine Cohesive Sediment Dynamics, 14, pp. 290–325.*

Morris, J. T., Sundareshwar, P. V., Nietch, C. T., Kjerfve, B., and Cahoon, D. R. (2002). Responses of coastal wetlands to rising sea level. *Ecology, 83, pp. 2869-2877.*

Nepf, H. M. and Ghisalberti, M. (2008). Flow and transport in channels with submerged vegetation. *Acta Geophysica, 56, 3, pp. 753-777.*

Nepf, H. M. and Vivoni, E. R. (2000). Flow structure in depth-limited, vegetated flow. *Journal of Geophysical Research, 105, C12 pp. 28547-28557.*

Nezu, I. and Nakagawa, H. (1993). Turbulence in open-channel flows. *IAHR-MOnographs, Balkema, Netherlands.*

Nikora, V., Goring, D., McEwan, I., and Griffiths, G. (2001). Spatially averaged open-channel flow over rough bed. *Journal of Hydraulic Engineering, ASCE, 127, 2, pp. 123-133.*

Nikora, V., Koll, K., McEwan, I., McLean, S., and Dittrich, A. (2004). Velocity distribution in the roughness layer of rough-bed flows. *Journal of Hydraulic Engineering, ASCE, 130, 10, pp. 1036-1042.*

Parchure, T. and Mehta, A. (1985). Erosion of soft cohesive sediment deposits. *J. Hydraul. Eng, 111, pp. 1308–1326.*

Paterson, D. M. (1964). Short-term changes in the erodibility of intertidal cohesive sediments related to the migratory behaviour of epipelic diatoms. *Journal of Geophysical Research, 69,24, pp. 5181-5190, doi:10.1029/JZ069i024p05181.*

Phillips, O. M. (1957). On the generation of waves by turbulent wind. *Journal of Fluid Mechanics, 2, pp.417-445.*

Pierson, J. and Moskowitz, L. (1989). A proposed spectral form for fully developed wind seas based on the similarity theory of s. a. kitaigorodskii. *Limnology and Oceanography, 34, pp. 223-234.*

Romano, C., Widdows, J., Brinsley, M. D., and Staff, F. (2003). Impact of enteromorpha intestinalis mats on near-bed currents and sediment dynamics: flume studies. *Marine Ecology Progress Series, 256, pp. 63-74.*

Silva, J., Duck, R., and Catarino, J. (2004). Seagrasses and sediment response to changing physical forcing in a coastal lagoon. *Hydrology and Earth System Sciences, 8, pp. 151-159.*

Smith, S. and Banke, E. (1975). Variation of the sea surface drag coefficient with wind speed. *Q.J.R. Meteorol. Soc., 101, pp. 665-673.*

Soulsby, R. (1997). Dynamics of marine sands: A manual for pratical applications. *Thomas Telford, London, 248.*

Traykovsky, P., Wiberg, L., and Geyer, W. R. (2007). Observation and modeling of wave-supported sediment gravity flows on the po prodelta and comparison to prior observations from the eel shelf. *Continental Shelf Research, 27, pp. 375–399.*

UNEP (2006). Marine and coastal ecosystems and human well being: a synthesis report based o the findings of the millennium ecosystem assessment. *Nairobi, Kenya: UNEP, pp. 76.*

Young, I. and Verhagen, L. (1996a). The growth of fetch limited waves in water of finite depth. part 1. total energy and peak frequency. *Coastal Engineering, 29, pp. 47-78.*

Young, I. and Verhagen, L. (1996b). The growth of fetch limited waves in water of finite depth. part 2. spectral evolution. *Coastal Engineering, 29, pp. 79-99.*